All-sky search for continuous gravitational waves from isolated neutron stars using Advanced LIGO and Advanced Virgo O3 data

R. Abbott *et al.*[*]
(LIGO Scientific Collaboration, Virgo Collaboration, and KAGRA Collaboration)

(Received 3 January 2022; accepted 17 October 2022; published 28 November 2022)

We present results of an all-sky search for continuous gravitational waves which can be produced by spinning neutron stars with an asymmetry around their rotation axis, using data from the third observing run of the Advanced LIGO and Advanced Virgo detectors. Four different analysis methods are used to search in a gravitational-wave frequency band from 10 to 2048 Hz and a first frequency derivative from -10^{-8} to 10^{-9} Hz/s. No statistically significant periodic gravitational-wave signal is observed by any of the four searches. As a result, upper limits on the gravitational-wave strain amplitude h_0 are calculated. The best upper limits are obtained in the frequency range of 100 to 200 Hz and they are $\sim 1.1 \times 10^{-25}$ at 95% confidence level. The minimum upper limit of 1.10×10^{-25} is achieved at a frequency 111.5 Hz. We also place constraints on the rates and abundances of nearby planetary- and asteroid-mass primordial black holes that could give rise to continuous gravitational-wave signals.

DOI: 10.1103/PhysRevD.106.102008

I. INTRODUCTION

The Advanced LIGO [1] and Advanced Virgo [2] detectors have made numerous detections of gravitational waves (GWs), to date consisting of short-duration (transient) GWs emitted during the inspirals and mergers of compact binary systems of black holes (BHs), neutron stars (NSs), [3,4], as well as mixed NS-BH binaries [5]. Among still undiscovered types of GW radiation are long-lasting, almost-monochromatic continuous waves (CWs), whose amplitudes and frequencies change much more slowly compared to those of transient sources (on the timescale of years rather than seconds). Astrophysically, promising sources of CWs are rotating, nonaxisymmetric NSs, emitting GWs at a frequency close to, or related to, their spin frequency. Deviations from the symmetry (a NS "deformation") may be caused by fluid instabilities, such as in the case of r-modes, or by elastic, thermal, or magnetic stresses in the crust and/or core of NS, and may be acquired at various stages of stars' isolated evolution, or during an interaction with a companion in a binary system (for recent reviews on sources of CW, see, e.g., [6–8]). Discovery of CWs emitted by NS would allow to probe their still mysterious interiors, study properties of dense matter in conditions distinct from those occurring in inspirals and mergers of binary NS systems, as well as carry out additional tests of the theory of gravity [9]. Due to intrinsically smaller GW amplitude of CWs in comparison to the already-detected transient sources, searches for CWs from rotating nonaxisymmetric NSs are essentially limited to the Galaxy.

The search presented here is not limited to gravitational-wave signals from deformed rotating neutron stars. Another source of quasimonochromatic, persistent GWs are very light, planetary- and asteroid-mass, inspiraling primordial black holes (PBHs), which could comprise a fraction or the totality of dark matter [10]. Such signals would arise from inspiraling PBHs whose chirp masses are less than $\mathcal{O}(10^{-5})M_\odot$ and whose GW frequencies are less than $\sim$250 Hz, and would be indistinguishable from those arising from nonaxisymmetric rotating NSs spinning up.

Recent detections of black holes made by the LIGO-Virgo-KAGRA Collaboration have revived interest in PBHs: low spin measurements and the rate inferences are consistent with those expected for BHs that formed in the early Universe [11]. Existence of light PBHs is well motivated theoretically and experimentally: recent detections of star and quasar microlensing events [12–14] suggest compact objects or PBHs with masses between 10^{-6} and 10^{-5} $M_\odot$ could constitute a fraction of dark matter of order $f_{\mathrm{PBH}} \sim 0.01$, which is consistent within the unified scenario for PBH formation presented in [15], but greater than expected for free-floating (i.e., not bound to an orbit) planets [16] (e.g., the hypothetical Planet 9 could be a PBH with a mass of 10^{-6} $M_\odot$ that was captured by the solar system [17]). PBHs may also collide with NSs and be responsible for the origin of NS-mass BHs, potentially detectable in the LIGO-Virgo-KAGRA searches [18]. However, constraints arising from such observations [10], even those that come from the LIGO-Virgo merging

[*]Full author list given at the end of the article.

TABLE I. Frequency and frequency derivative search ranges of the four pipelines.

Pipeline	Frequency (Hz)	Frequency derivative (Hz/s)
FrequencyHough	10–2048	$-10^{-8} - 10^{-9}$
SkyHough	65–350	$-10^{-9} - 5 \times 10^{-12}$
SOAP	40–1000	$-10^{-9} - 10^{-9}$
	1000–2000	$-10^{-8} - 10^{-8}$
TD Fstat	20–200	$-3.2 \times 10^{-9} f/100 - 0$
	200–750	$-2 \times 10^{-10} - 2 \times 10^{-11}$

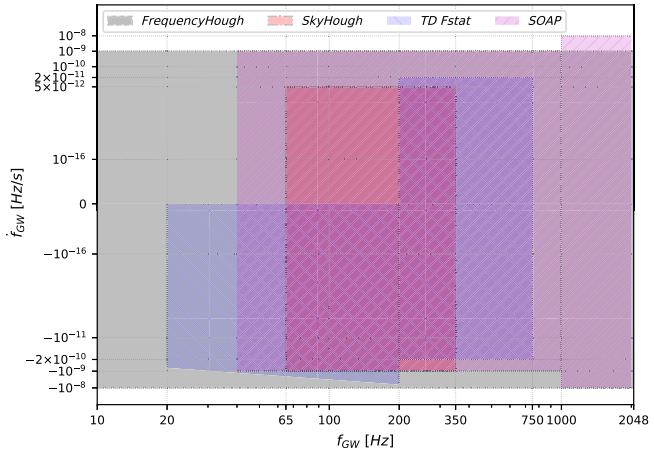

FIG. 1. Frequency and frequency derivative search ranges of the four pipelines: the *FrequencyHough* pipeline ranges marked in grey, *SkyHough* in red, *Time-Domain $\mathcal{F}$-statistic* in blue, and *SOAP* in magenta. See Table I for details.

rate inferences [19,20] and stochastic background searches [21,22], rely on modeling assumptions, and can be evaded if, for example, PBHs formed in clusters [23–28]. It is therefore important to develop complementary probes of these mass regimes to test different PBH formation models [29,30], which is possible by searching for continuous GWs.

Searches for continuous waves are usually split in three different domains: *targeted searches* look for signals from known pulsars; *directed searches* look for signals from known sky locations; *all-sky searches* look for signals from unknown sources. All-sky searches for *a priori* unknown CW sources have been carried out in the Advanced LIGO and Advanced Virgo data previously [31–43]. A recent review on pipelines for wide parameter-space searches can be found in [44].

Here we report on results from an all-sky, broad frequency range search using the most-sensitive data to date, the LIGO-Virgo O3 observing run, employing four different search pipelines: the *FrequencyHough* [45], *SkyHough* [46], *Time-Domain $\mathcal{F}$-statistic* [47,48], and *SOAP* [49]. Each pipeline uses different data analysis methods and covers different regions of the frequency and frequency time derivative parameter space, although there exist overlaps between them (see Table I and Fig. 1 for details). The search is performed for frequencies between 10 and 2048 Hz and for a range of frequency time derivative between -10^{-8} and 10^{-9} Hz/s, covering the whole sky. We note here that the search is generally agnostic to the type of the GW source, so the results are not actually limited to signals from nonaxisymmetric rotating NSs in our Galaxy. A comprehensive multistage analysis of the signal outliers obtained by the four pipelines has not revealed any viable candidate for a continuous GW signal. However we improve the broad-range frequency upper limits with respect to previous O1 and O2 observing runs and also with respect to the recent analysis of the first half of the O3 run [39]. This is also the first all-sky search for CW sources that uses the Advanced Virgo detector's data.

The article is organized as follows: in Sec. II we describe the O3 observing run and provide details about the data used. In Sec. III we present an overview of the pipelines used in the search. In Sec. IV details of the data-analysis pipelines are described. In Sec. V, we describe the results obtained by each pipeline, namely the signal candidates and the sensitivity of the search; whereas Sec. VI contains a discussion of the astrophysical implications of our results.

II. DATASETS USED

The dataset used in this analysis was the third observing run (O3) of the Advanced LIGO and Advanced Virgo GW detectors [1,2]. LIGO is made up of two laser interfero meters, both with 4 km long arms. One is at the LIGO Livingston Observatory (L1) in Louisiana, USA and the other is at the LIGO Hanford Observatory (H1) in Washington, USA. Virgo (V1) consists of one interferometer with 3 km arms located at European Gravitational Observatory in Cascina, Italy. The O3 run took place between April 1, 2019, and March 27, 2020. The run was divided into two parts, O3a and O3b, separated by one month commissioning break that took place in October 2019. The duty factors for this run were ∼76%, ∼71%, ∼76% for L1, H1, V1, respectively. The maximum uncertainties (68% confidence interval) on the calibration of the LIGO data were of 7%/11% in magnitude and 4 deg/9 deg in phase for O3a/O3b data ([50,51]). For Virgo, it amounted to 5% in amplitude and 2 deg in phase, with the exception of the band 46–51 Hz, for which the maximum uncertainty was estimated as 40% in amplitude and 34 deg in phase during O3b. For the smaller range 49.5–50.5 Hz, the calibration was unreliable during the whole run [52].

III. OVERVIEW OF SEARCH PIPELINES

In this section we provide a broad overview of the four pipelines used in the search. The three pipelines:

FrequencyHough, *SkyHough*, and *Time-Domain $\mathcal{F}$-statistic* have been used before in several all-sky searches of the LIGO data. The *SOAP* pipeline is a new pipeline applied for the first time to an all-sky search. It uses novel algorithms. *SOAP* aims at a fast, preliminary search of the data before more sensitive but much more time consuming methods are applied (see [44] for a review on pipelines for wide parameter-space searches). The individual pipelines are described in more detail in the following section.

A. Signal model

The GW signal in the detector frame from an isolated, asymmetric NS spinning around one of its principal axis of inertia is given by [47]

$$h(t) = h_0\left[F_+(t,\alpha,\delta,\psi)\frac{1+\cos^2\iota}{2}\cos\phi(t) + F_\times(t,\alpha,\delta,\psi)\cos\iota\sin\phi(t)\right], \quad (1)$$

where F_+ and $F_\times$ are the antenna patterns of the detectors dependent on right ascension α, declination δ of the source and polarization angle ψ, h_0 is the amplitude of the signal, ι is the angle between the total angular momentum vector of the star and the direction from the star to the Earth, and $\phi(t)$ is the phase of the signal. The amplitude of the signal is given by

$$h_0 = \frac{4\pi^2 G}{c^4}\frac{\epsilon I_{zz} f^2}{d} \approx 1.06\times10^{-26}\left(\frac{\epsilon}{10^{-6}}\right) \times\left(\frac{I_{zz}}{10^{38}\ \mathrm{kg\,m^2}}\right)\left(\frac{f}{100\ \mathrm{Hz}}\right)^2\left(\frac{1\ \mathrm{kpc}}{d}\right), \quad (2)$$

where d is the distance from the detector to the source, f is the GW frequency (assumed to be twice the rotation frequency of the NS), ϵ is the ellipticity or asymmetry of the star, given by $(I_{xx}-I_{yy})/I_{zz}$, and I_{zz} is the moment of inertia of the star with respect to the principal axis aligned with the rotation axis.

We assume that the phase evolution of the GW signal can be approximated with a second order Taylor expansion around a fiducial reference time τ_r:

$$\phi(\tau) = \phi_o + 2\pi\left[f(\tau-\tau_r) + \frac{\dot{f}}{2!}(\tau-\tau_r)^2\right], \quad (3)$$

where ϕ_o is an initial phase and f and $\dot{f}$ are the frequency and first frequency derivative at the reference time. The relation between the time at the source τ and the time at the detector t is given by

$$\tau(t) = t + \frac{\vec{r}(t)\cdot\vec{n}}{c} + \Delta_{E\odot} - \Delta_{S\odot}, \quad (4)$$

where $\vec{r}(t)$ is the position vector of the detector in the Solar System Barycenter frame, and $\vec{n}$ is the unit vector pointing to the NS; $\Delta_{E\odot}$ and $\Delta_{S\odot}$ are, respectively, the relativistic Einstein and Shapiro time delays. In standard equatorial coordinates with right ascension α and declination δ, the components of the unit vector $\vec{n}$ are given by $(\cos\alpha\cos\delta, \sin\alpha\cos\delta, \sin\delta)$.

B. Parameter space analyzed

All the four pipelines perform an all-sky search; however the frequency and frequency derivative ranges analyzed are different for each pipeline. The detailed ranges analyzed by the four pipelines are summarized in Table I and presented in Fig. 1. The *FrequencyHough* pipeline analyzes a broad frequency range between 10 and 2048 Hz and a broad frequency time derivative range between -10^{-8} and 10^{-9} Hz/s. A very similar range of f and $\dot{f}$ is analyzed by the *SOAP* pipeline. The *SkyHough* pipeline analyzes a narrower frequency range where the detectors are most sensitive whereas the *Time-Domain $\mathcal{F}$-statistic* pipeline analyzes f and $\dot{f}$ ranges of the bulk of the observed pulsar population (see Fig. 2 in Sec. IV C).

C. Detection statistics

As all-sky searches cover a large parameter space they are computationally very expensive and it is computationally prohibitive to analyze coherently the data from the full observing run using optimal matched filtering. As a result each of the pipelines developed for the analysis uses a semicoherent method. Moreover to reduce the computer memory and to parallelize the searches the data are divided into narrow bands. Each analysis begins with sets of *short Fourier transforms* (SFTs) that span the observation period, with coherence times ranging from 1024s to 8192s. The *FrequencyHough*, *SkyHough*, and *SOAP* pipelines compute measures of strain power directly from the SFTs and create detection statistics by stacking those powers with corrections for frequency evolution applied. The *FrequencyHough* and *SkyHough* pipelines use *Hough* transform to do the stacking whereas the *SOAP* pipeline uses the *Viterbi* algorithm. The *Time-Domain $\mathcal{F}$-statistic* pipeline extracts band-limited 6-day long time-domain data segments from the SFT sets and applies frequency evolution corrections coherently to obtain the *$\mathcal{F}$-statistic* [47]. Coincidences are then required among multiple data segments with no stacking.

D. Outlier follow-up

All four pipelines perform a follow-up analysis of the statistically significant candidates (outliers) obtained during the search. All pipelines perform vetoing of the outliers

corresponding to narrow, instrumental artifacts (lines) in the advanced LIGO detectors ([54]). Several other consistency vetoes are also applied to eliminate outliers. The *FrequencyHough*, *SkyHough*, and *Time-Domain $\mathcal{F}$-statistic* pipelines perform a follow-up of the candidates by processing the data with increasing long coherence times whereas *SOAP* pipeline use *convolutional neural networks* to do the post processing.

E. Upper limits

No periodic gravitational wave signals were observed by any of the four pipelines and all the pipelines obtain upper limits on their strength. The three pipelines *SkyHough*, *Time-Domain $\mathcal{F}$-statistic*, and *SOAP* obtain the upper limits by injections of the signals according to the model given in Sec. III A above for an array of signal amplitudes h_0 and randomly choosing the remaining parameters. The *FrequencyHough* pipeline obtains upper limits using an analytic formula [see Eq. (6)] that depends on the spectral density of the noise of the detector. The formula was validated by a number of tests consisting of injecting signals to the data.

IV. DETAILS OF SEARCH METHODS

A. *FrequencyHough*

The *FrequencyHough* pipeline is a semicoherent procedure in which interesting points (i.e., outliers) are selected in the signal parameter space, and then are followed-up in order to confirm or reject them. This method has been used in several past all-sky searches of Virgo and LIGO data [31,34,35,55]. A detailed description of the methodology can be found in [45]. In the following, we briefly describe the main analysis steps and specific choices used in the search.

Calibrated detector data are used to build "short duration" and cleaned [56] fast Fourier transforms (FFTs), with duration T_{FFT} which depends on the frequency band being considered, see Table II.

Next, local maxima are selected based on the square root of the equalized power of the data[1] passing a dimensionless threshold of $\Theta = 1.58$. The collection of these time-frequency peaks forms the so-called *peakmap*.

The peakmap is cleaned of the strongest disturbances using a *line persistency* veto [45].

The time-frequency peaks of the peakmap are properly shifted, for each sky position,[2] to compensate the Doppler effect due to the detector motion [45]. The shifted peaks are then fed to the *FrequencyHough* algorithm [45], which transforms each peak to the frequency/spin-down plane of the source. The frequency and spin-down bins (which we will refer to as *coarse* bins in the following) depend on the frequency band, as shown in Table II, and are defined, respectively, as $\delta f = 1/T_{\mathrm{FFT}}$ and $\delta\dot{f} = \delta f/T_{\mathrm{obs}}$, where T_{obs} is the total run duration. In practice, the nominal frequency resolution has been increased by a factor of 10 [45], as the *FrequencyHough* is not computationally bounded by the width of the frequency bin. The algorithm, moreover, adaptively weights any noise nonstationarity and the time-varying detector response [57].

TABLE II. Properties of the FFTs used in the *FrequencyHough* pipeline. The time duration T_{FFT} refers to the length in seconds of the data chunks on which the FFT is computed. The frequency bin width is the inverse of the time duration, while the spin-down bin width is computed as $\delta\dot{f} = \delta f/T_{\mathrm{obs}}$, where T_{obs} is the total run duration.

Band (Hz)	T_{FFT} (s)	δf (Hz)	$\delta\dot{f}$ (Hz/s)
10–128	8192	1.22×10^{-4}	3.92×10^{-12}
128–512	4096	2.44×10^{-4}	7.83×10^{-12}
512–1024	2048	4.88×10^{-4}	1.57×10^{-11}
1024–2048	1024	9.76×10^{-4}	3.13×10^{-11}

The whole analysis is split into tens of thousands of independent jobs, each of which covers a small portion of the parameter space. Moreover, for frequencies above 512 Hz a GPU-optimized implementation of the *FrequencyHough* transform has been used [58].

The output of a *FrequencyHough* transform is a 2D histogram in the frequency/spin-down plane of the source.

Outliers, that is, significant points in this plane, are selected by dividing each 1 Hz band of the corresponding histogram into 20 intervals and taking, for each interval, and for each sky location, the one or (in most cases) two candidates with the highest histogram number count [45]. All the steps described so far are applied separately to the data of each detector involved in the analysis.

As in past analyses [31,34], candidates from each detector are clustered and then coincident candidates among the clusters of a pair of detectors are found using a distance metric[3] d_{FH} built in the four-dimensional parameter space of sky position (λ, β) (in ecliptic coordinates), frequency f, and spin-down $\dot{f}$. Pairs of candidates with distance $d_{\mathrm{FH}} \leq 3$ are considered coincident. In the

[1]Computed as the ratio of the squared modulus of each FFT of the data and an autoregressive estimation of the average power spectrum, see [56] for more details.

[2]Over a suitable grid, which bin size depends on the frequency and sky location.

[3]The metric is defined as

$$d_{\mathrm{FH}} = \sqrt{\left(\frac{\Delta f}{\delta f}\right)^2 + \left(\frac{\Delta \dot{f}}{\delta \dot{f}}\right)^2 + \left(\frac{\Delta \lambda}{\delta \lambda}\right)^2 + \left(\frac{\Delta \beta}{\delta \beta}\right)^2},$$

Δf, $\Delta\dot{f}$, $\Delta\lambda$, and $\Delta\beta$ are the differences, for each parameter, among pairs of candidates of the two detectors, and δf, $\delta\dot{f}$, $\delta\lambda$, and $\delta\beta$ are the corresponding bin widths.

current O3 analysis, coincidences have been done only among the two LIGO detectors for frequencies above 128 Hz, while also coincidences H1-Virgo and L1-Virgo have been considered for frequencies below 128 Hz, where the difference in sensitivity (especially in the very low frequency band) is less pronounced.

Coincident candidates are ranked according to the value of a statistic built using the distance and the *FrequencyHough* histogram weighted number count of the coincident candidates [45]. After the ranking, the eight outliers in each 0.1 Hz band with the highest values of the statistic are selected and subject to the follow-up.

1. Follow-up

The *FrequencyHough* follow-up runs on each outlier of each coincident pair. It is based on the construction of a new peakmap, over ± 3 *coarse* bins around the frequency of the outlier, with a longer T_{FFT}. This new peakmap is built after the removal of the signal frequency variation due to the Doppler effect for a source located at the outlier sky position.

A new refined grid on the sky is built around this point, covering ± 3 *coarse* bins, in order to take into account the uncertainty on the outlier parameters. For each point of this grid we remove the residual Doppler shift from the peakmap by properly shifting the frequency peaks. Each new corrected peakmap is the input for the *FrequencyHough* transform to explore the frequency and the spin-down range of interest (± 3 *coarse* bins for the frequency and the spin-down). The most significant peak among all the *FrequencyHough* histograms, characterized by a set of *refined* parameters, is selected and subject to further postprocessing steps.

First, the *significance* veto (V1) is applied. It consists in building a new peakmap over 0.2 Hz around the outlier refined frequency, after correcting the data with its refined parameters. The corrected peakmap is then projected on the frequency axis. Its frequency range is divided in subbands, each covering ± 2 coarse frequency bins. The maximum of the projection in the subband containing the outlier is compared with the maxima selected in the remaining *off-source* intervals. The outlier is kept if it ranks as first or second for both detectors. Second, a *noise line* veto (V2) is used, which discards outliers whose frequency, after the removal of the Doppler and spin-down corrections, overlaps a band polluted by known instrumental disturbances. The *consistency* test (V3) discards pairs of coincident outliers if their critical ratios (CRs), properly weighted by the detector noise level, differ by more than a factor of 5. The CR is defined as

$$CR = \frac{x - \mu}{\sigma}, \tag{5}$$

where x is the value of the peakmap projection in a given frequency bin, μ is the average value, and σ the standard deviation of the peakmap projection. The *distance* veto (V4) consists in removing pairs of coincident outliers with distance $d_{\mathrm{FH}} > 6$ after the follow-up. Finally, outliers with distance $d_{\mathrm{FH}} < 3$ from *hardware injections* are also vetoed (V5). Outliers which survive all these vetoes are scrutinized more deeply, by applying a further follow-up step, based on the same procedures just described, but further increasing the segment duration T_{FFT}.

2. Parameter space

The *FrequencyHough* search covers the frequency range [10, 2048] Hz, a spin-down range between -10^{-8} Hz/s and 10^{-9} Hz/s and the whole sky. The frequency and spin-down resolutions are given in Table II. The sky resolution, on the other hand, is a function of the frequency and of the sky position and is defined in such a way that for two nearby sky cells the maximum frequency variation, due to the Doppler effect, is within one frequency bin, see [45] for more details.

3. Upper limits

"Population average" upper limits are computed for every 1 Hz subband in the range of 20–2048 Hz,[4] considering only the LIGO detectors, as Virgo sensitivity is worse for most of the analyzed frequency band. First, for each detector we use the analytical relation [45]

$$h_{UL,95\%} \approx \frac{4.97}{N^{1/4}} \sqrt{\frac{S_n(f)}{T_{\mathrm{FFT}}}} \sqrt{CR_{\max} + 1.6449}, \tag{6}$$

where N is the actual number of data segments used in the analysis, $S_n(f)$ is the detector average noise power spectrum, computed through a weighted mean over time segments of duration T_{FFT} (in order to take into account noise nonstationarity), and $CR_{\max}$ is the maximum outlier CR[5] in the given 1 Hz band. Comparing this equation with Eq. (67) in [45], the coefficient 4.97 has been obtained taking the parameter $\theta_{\mathrm{thr}} = 2.5$ (the values of p_0, p_1 directly depend on it), while the term 1.6449 comes from taking the confidence level parameter $\Gamma = 0.95$. For each 1 Hz band, the final upper limit is the worse among those computed separately for Hanford and Livingston. Such upper limits implicitly assume an average over the source population parameters. In order to compute upper limits which hold for specific source parameters, a scaling factor must be applied as discussed in the Appendix.

As verified through a detailed comparison based on LIGO and Virgo O2 and O3 data, this procedure produces

[4]Although the search starts at 10 Hz, we decided to compute upper limit starting from 20 Hz, due to the unreliable calibration at lower frequency.

[5]Defined by Eq. (5) and where in this case the various quantities are computed over the *FrequencyHough* map.

conservative upper limits with respect to those obtained through the injection of simulated signals, which is computationally much heavier [59].

Moreover, it has been shown that the upper limits obtained through injections are always above those based on Eq. (6) when the minimum CR in each 1 Hz subband is used. The two curves based, respectively, on the highest and the smallest CR delimit a region containing both a more stringent upper limit estimate and the search sensitivity estimate, that is the minimum strain of a detectable signal. Any astrophysical implication of our results, discussed in Sec. V will be always based on the most conservative estimate.

B. *SkyHough*

SkyHough [46,60] is a semicoherent pipeline based on the Hough transform to look for CW signals from isolated neutron stars. Several versions of this pipeline have been used throughout the initial [61,62] and advanced [31,32] detector era, as well as to look for different kinds of signals such as CW from neutron stars in binary systems [40,41,63] or long-duration GW transients [64]. The current implementation of *SkyHough* closely follows that of [32] and includes an improved suite of postprocessing and follow-up stages [65–67].

1. Parameter space

The *SkyHough* pipeline searches over the standard four parameters describing a CW signal from isolated NS: frequency f, spin-down $\dot{f}$, and sky position parametrized using equatorial coordinates α, δ.

Parameter-space resolutions are given in [46]

$$\delta f = \frac{1}{T_{\mathrm{SFT}}}, \qquad \delta\dot{f} = \frac{\delta f}{T_{\mathrm{obs}}}, \qquad \delta\theta = \frac{c/v}{T_{\mathrm{SFT}}\mathrm{P_f} f}, \quad (7)$$

where θ represents either of the sky angles, $v/c \simeq 10^{-4}$ represents the average detector velocity as a fraction of the speed of light, and the pixel factor $\mathrm{P_f} = 2$ is a tunable overresolution parameter. Table III summarizes the numerical values employed in this search.

The *SkyHough* all-sky search covers the most sensitive frequency band of the advanced LIGO detectors, between 65 and 350 Hz. This band is further subdivided into $\Delta f = 0.025$ Hz subbands, resulting in a total of 11400 frequency bands. Spin-down values are covered from -1×10^{-9} to 5×10^{-12} Hz/s, which include typical spin-up values associated to CW emission from the evaporation of boson clouds around black holes [68].

TABLE III. Parameter-space resolutions employed by the *SkyHough* pipeline.

Parameter	Resolution
δf	1.4×10^{-4} Hz
$\delta\dot{f}$	5×10^{-12} Hz/s
$\delta\theta$	0.69 Hz/f

2. Description of the search

The first stage of the *SkyHough* pipeline performs a multidetector search using H1 and L1 SFTs with $T_{\mathrm{SFT}} = 7200s$. Each 0.025 Hz subband is analyzed separately using the same two step strategy as in [32,41]: parameter space is efficiently analyzed using *SkyHough*'s look-up table approach; the top 0.1% most significant candidates are further analyzed using a more sensitive statistic. The result for each frequency subband is a toplist containing the 10^5 most significant candidates across the sky and spin-down parameter space.

Each toplist is then clustered using a novel approach presented in [65] and first applied in [41]. A parameter-space distance is defined using the average mismatch in frequency evolution between two different parameter-space templates

$$d(\vec{\lambda}, \vec{\lambda}_*) = \frac{T_{\mathrm{SFT}}}{N_{\mathrm{SFT}}} \sum_{\alpha=0}^{N_{\mathrm{SFT}}} |f(t_\alpha; \vec{\lambda}) - f(t_\alpha; \vec{\lambda}_*)|, \quad (8)$$

where $f(t; \vec{\lambda})$ is defined as

$$f(t; \vec{\lambda}) = [f + (t - t_{\mathrm{ref}}) \cdot \dot{f}] \cdot \left[1 + \frac{\vec{v}(t) \cdot \vec{n}}{c}\right] \quad (9)$$

and $\vec{\lambda} = \{f, \dot{f}, \alpha, \delta\}$ refers to the phase-evolution parameters of the template.

Clusters are constructed by pairing together templates in consecutive frequency bins such that $d(\vec{\lambda}, \vec{\lambda}_*) \leq 1$. Each cluster is characterized by its most significant element (the *loudest* element). From each 0.025 Hz subband, we retrieve the 40 most significant clusters for further analysis. This results in a total of 456000 candidates to follow-up.

The loudest cluster elements are first sieved through the *line veto*, a standard tool to discard clear instrumental artifacts using the list of known, narrow, instrumental artifacts (lines) in the advanced LIGO detectors [54]: If the instantaneous frequency of a candidate overlaps with a frequency band containing an instrumental line of known origin, the candidate is ascribed an instrumental origin and consequently ruled out.

Surviving candidates are then followed-up using PYFSTAT, a PYTHON package implementing a Markov-chain Monte Carlo (MCMC) search for CW signals [66,69]. The follow-up uses the $\mathcal{F}$-*statistic* as a (log) Bayes factor to sample the posterior probability distribution of the phase-evolution parameters around a certain parameter-space region

$$\mathrm{P}(\vec{\lambda}|x) \propto e^{\mathcal{F}(\vec{\lambda};x)} \cdot \mathrm{P}(\vec{\lambda}), \quad (10)$$

TABLE IV. Coherence-time configuration of the multistage follow-up employed by the *SkyHough* pipeline. The data stream is divided into a fix number of segments of the same length; the reported coherence time is an approximate value obtained by dividing the observation time by the number of segments at each stage.

Stage	0	1	2	3	4	5
N_{seg}	660	330	92	24	4	1
T_{coh}	0.5 day	1 day	4 days	15 days	90 days	360 days

where $\mathrm{P}(\vec{\lambda})$ represents the prior probability distribution of the phase-evolution parameters. The *$\mathcal{F}$-statistic*, as opposed to the *SkyHough* number count, allows us to use longer coherence times, increasing the sensitivity of the follow-up with respect to the main search stage.

As initially described in [69], the effectiveness of an MCMC follow-up is tied to the number of templates covered by the initial prior volume, suggesting a hierarchical approach: coherence time should be increased following a ladder so that the follow-up is able to converge to the true signal parameters at each stage. We follow the proposal in [67] and compute a coherence-time ladder using $\mathcal{N}^* = 10^3$ [see Eq. (31) of [69]] starting from $T_{\mathrm{coh}} =$ 1 day including an initial stage of $T_{\mathrm{coh}} = 0.5$ days. The resulting configuration is collected in Table IV.

The first follow-up stage is similar to that employed in [40,41]: an MCMC search around the loudest candidate of the selected clusters is performed using a coherence time of $T_{\mathrm{coh}} = 0.5$ days. Uniform priors containing four parameter-space bins in each dimension are centered around the loudest candidate. A threshold is calibrated using an injection campaign: any candidate whose loudest $2\mathcal{F}$ value over the MCMC run is lower than $2\mathcal{F} = 3450$ is deemed inconsistent with CW signal.

The second follow-up stage is a variation of the method described in [67], previously applied to [39,70]. For each outlier surviving the initial follow-up stage (stage 0 in Table IV), we construct a Gaussian prior using the median and interquartile range of the posterior samples and run the next-stage MCMC follow-up. The resulting maximum $2\mathcal{F}$ is then compared to the expected $2\mathcal{F}$ inferred from the previous MCMC follow-up stage. Highly discrepant candidates are deemed inconsistent with a CW signal and hence discarded.

Given an MCMC stage using $\hat{N}$ segments from which a value of $2\hat{\mathcal{F}}$ is recovered, the distribution of $2\mathcal{F}$ values using N segments is well approximated by

$$\mathrm{P}(2\mathcal{F}|N, 2\hat{\mathcal{F}}, \hat{N}) = \frac{1}{\sqrt{2\pi\sigma^2}} e^{-\frac{1}{2}\left(\frac{2\mathcal{F}-\mu}{\sigma}\right)^2}, \tag{11}$$

where

TABLE V. $2\mathcal{F}$ consistency brackets employed in the multistage follow-up of the *SkyHough* pipeline. Brackets were computed using a campaign of 500 software-injected signals representing an isotropic population of uniformly sky-distributed NS at 150 representative frequency bands with an amplitude corresponding to the $h_0^{95\%}$ sensitivity estimation. The implied false dismissal probability is $\lesssim 1/(150 \times 500) \simeq 1.3 \times 10^{-5}$. Stages correspond to those described in Table IV.

Comparing stages	$(2\mathcal{F} - \mu)/\sigma$ bracket
Stage 0 vs Stage 1	$(-1.79, 1.69)$
Stage 1 vs Stage 2	$(-1.47, 1.35)$
Stage 2 vs Stage 3	$(-0.94, 0.80)$
Stage 3 vs Stage 4	$(-0.63, 0.42)$
Stage 4 vs Stage 5	$(-0.34, 0.11)$

$$\mu = \rho_0^2 + 4N, \tag{12}$$

$$\sigma^2 = 8 \cdot (N + \hat{N} + \rho_0^2), \tag{13}$$

and $\rho_0^2 = 2\hat{\mathcal{F}} - 4\hat{N}$ is a proxy for the (squared) SNR [71]. Equation (11) is exact in the limit of $N, \hat{N} \gg 1$ or $\rho_0^2 \gg 1$. In this search, however, we calibrate a bracket on $(2\mathcal{F} - \mu)/\sigma$ for each follow-up stage using an injection campaign, shown in Table V. Candidates outside of the bracket are deemed inconsistent with a CW signal.

Any surviving candidates are subject to manual inspection in search for obvious instrumental causes such as hardware-injected artificial signals or narrow instrumental artifacts.

C. *Time-Domain $\mathcal{F}$-statistic*

The *Time-Domain $\mathcal{F}$-statistic* search method has been applied to an all-sky search of VSR1 data [48] and all-sky searches of the LIGO O1 and O2 data [31,32,34]. The main tool of the pipeline is the *$\mathcal{F}$-statistic* [47] with which one can coherently search the data over a reduced parameter space consisting of signal frequency, its derivatives, and the sky position of the source. However, a coherent all-sky search over the long dataset like the whole data of O3 run is computationally prohibitive. Thus the data are divided into shorter time domain segments. Moreover, to reduce the computer memory required to do the search, the data are divided into narrow band segments that are analyzed separately. As a result the *Time-Domain $\mathcal{F}$-statistic* pipeline consists of two parts. The first part is the coherent search of narrow band, time-domain segments. The second part is the search for coincidences among the parameters of the candidates obtained from the coherent search of all the time domain segments.

The algorithms to calculate the *$\mathcal{F}$-statistic* in the coherent search are described in Sec. 6.2 of [48]. The time series is divided into segments, called frames, of six sidereal days long each. Moreover the data are divided into subbands of

0.25 Hz overlapped by 0.025 Hz. The O3 data has a number of nonscience data segments. The values of these bad data are set to zero. For our analysis, we choose only segments that have a fraction of bad data less than 60% both in H1 and L1 data and there is an overlap of more than 50% between the data in the two detectors. This requirement results in 41 six-day-long data segments for each subband. For the search we use a four-dimensional grid of templates (parametrized by frequency, spin down rate, and two more parameters related to the position of the source in the sky) constructed in Sec. 4 of [72] with grid's minimal match parameter MM chosen to be $\sqrt{3}/2$. This choice of the grid spacing led to the following resolution for the four parameters of the space that we search

$$\Delta f \simeq 1.9 \times 10^{-6}\ \text{Hz}, \tag{14a}$$

$$\Delta \dot{f} \simeq 1.1 \times 10^{-11}\ \text{Hz/s}, \tag{14b}$$

$$\Delta \alpha \simeq 7.4 \times 10^{-2} \left(\frac{100\ \text{Hz}}{f}\right)\ \text{rad}, \tag{14c}$$

$$\Delta \delta \simeq 1.5 \times 10^{-2} \left(\frac{100\ \text{Hz}}{f}\right)\ \text{rad}. \tag{14d}$$

We set a fixed threshold of 15.5 for the $\mathcal{F}$-*statistic* and record the parameters of all threshold crossings, together with the corresponding values of the $\mathcal{F}$-*statistic*. In the second stage of the analysis we use exactly the same coincidence search algorithm as in the analysis of VSR1 data and described in detail in Sec. 8 of [48] with only one change. We use a different coincidence cell from that described in [48]. In [48] the coincidence cell was constructed from Taylor expansion of the autocorrelation function of the $\mathcal{F}$-*statistic*. In the search performed here the chosen coincidence cell is a suitably scaled grid cell used in the coherent part of the pipeline. We scale the four dimensions of the grid cell by different factors given by [16 8 2 2] corresponding to frequency, spin down rate (frequency derivative), and two more parameters related to the position of the source in the sky, respectively. This choice of scaling gives optimal sensitivity of the search. We search for coincidences in each of the bands analyzed. Before identifying coincidences we veto candidate signals overlapping with the instrumental lines identified by independent analysis of the detector data. To estimate the significance of a given coincidence, we use the formula for the false alarm probability derived in the Appendix of [48]. Sufficiently significant coincidences are called outliers and are subject to a further investigation.

1. Parameter space

Our *Time-Domain* $\mathcal{F}$-*statistic* analysis is a search over a four-dimensional space consisting of four parameters: frequency, spin-down rate, and sky position. As we search over the whole sky the search is very computationally intensive. Given that our computing resources are limited, to achieve a satisfactory sensitivity we have restricted the range of frequency and spin-down rates analyzed to cover the frequency and spin-down ranges of the bulk of the observed pulsars. Thus we have searched the gravitational frequency band from 20 to 750 Hz. The lower frequency of 20 Hz is chosen due to the low sensitivity of the interferometers below 20 Hz. In the frequency 20 to 130 Hz range, assuming that the GW frequency is twice the spin frequency, we cover young and energetic pulsars, such as Crab and Vela. In the frequency range from 80 to 160 Hz we can expect GW signal due to r-mode instabilities [73,74]. In the frequency range from 160 to 750 Hz we can expect signals from most of the recycled millisecond pulsars, see Fig. 3 of [75].

For the GW frequency derivative $\dot{f}$ we have chosen a frequency dependent range. Namely, for frequencies less than 200 Hz we have chosen $\dot{f}$ to be in the range $[-f/\tau_{\min}, 0]$, where $\tau_{\min}$ is a limit on pulsar's characteristic age, and we have taken $\tau_{\min} = 1000$ yr. For frequencies greater than 200 Hz we have chosen a fixed range for the spin-down rate. As a result, the following ranges of $\dot{f}$ were searched in our analysis:

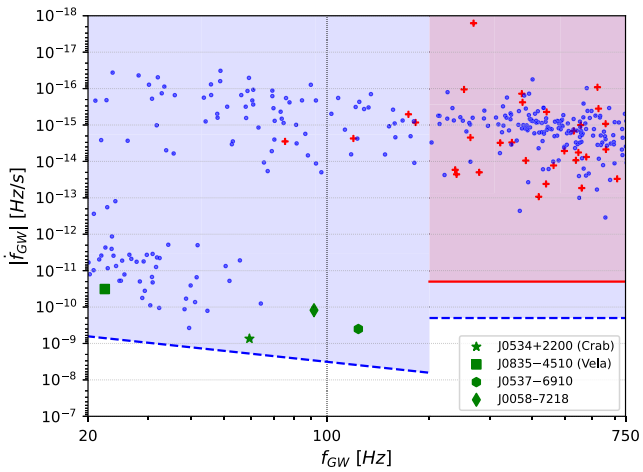

FIG. 2. Frequency time derivative for tentative emission of GWs ($\dot{f} \equiv 2\dot{f}_{\text{rot}}$) as a function of the frequency of emitted GWs ($f \equiv 2f_{\text{rot}}$), where f_{rot} and $\dot{f}_{\text{rot}}$ are rotational frequency and frequency time derivative for known pulsars, obtained from the Australia Telescope National Facility (ATNF) database [53]. The vertical axis shows the absolute value for both negative values of the frequency time derivative ("spin-down," blue dots) and positive values ("spinup," red plus symbols). Blue dashed lines represent spin-down limits used in the *Time-Domain* $\mathcal{F}$-*statistic* search: for $f < 200$ Hz, $0 > \dot{f} > -f/\tau_{\min}$, where $\tau_{\min} = 1000$ yr denotes a limit on pulsar's characteristic age; for $f > 200$ Hz, $\dot{f} > -2 \times 10^{-10}$ Hz/s. For $f > 200$ Hz in the case of spinning-up objects, in the $\mathcal{F}$-*statistic* search we admit a positive range of values to $\dot{f} < 2 \times 10^{-11}$ Hz/s. The boundary of this range is marked by a red continuous line.

$$0 > \dot{f} > -3.2 \times 10^{-9} \frac{f}{100\,\mathrm{Hz}}\ \mathrm{Hz/s},\ \text{for } f < 200\,\mathrm{Hz}, \quad (15a)$$

$$2 \times 10^{-11}\ \mathrm{Hz/s} > \dot{f} > -2 \times 10^{-10}\ \mathrm{Hz/s},\ \text{for } f > 200\,\mathrm{Hz}. \quad (15b)$$

In Fig. 2 we plot GW frequency derivatives against GW frequencies (assuming the GW frequency is twice the spin frequency of the pulsar) for the observed pulsars from the ATNF catalog [53]. We show the range of the GW frequency derivative selected in our search, and one can see that the expected frequency derivatives of the observed pulsars are well within this range. Note, finally, that we have made the conservative choice of including positive values of the frequency derivative ("spin-up"), in order to search as wide a range as possible. In most cases, however, the pulsars that appear to spin up are in globular clusters, for which the local forces make the measurement unreliable [76].

2. Sensitivity of the search

In order to assess the sensitivity of the $\mathcal{F}$-*statistic* search, we set upper limits on the intrinsic GW amplitude h_0 in each 0.25 Hz bands. To do so, we generate signals for an array of eight amplitudes h_0 and for randomly selected sky positions (samples drawn uniformly from the sphere). For each amplitude, we generate 100 signals with f, $\dot{f}$, the polarization angle ψ, and cosine of the inclination angle ι are chosen from uniform random distributions in their respective ranges. The signals are added to the real data segments, and searches are performed with the same grids and search setup as for the real data search, in the neighborhood of injected signal parameters. We search ± 6 grid points for $\dot{f}$ and ± 1 grid points for the sky positions away from the true values of the signal's parameters. We consider a signal detected if coincidence multiplicity for the injected signal is higher than the highest signal multiplicity in a given subband and in a given hemisphere in the real data search. The detection efficiency is the fraction of recovered signals. We estimate the $h_0^{95\%}$, i.e., 95% confidence upper limit on the GW amplitude h_0, by fitting[6] a sigmoid function to a range of detection efficiencies E as a function of injected amplitudes h_0, $E(h_0) = (1 + e^{k(x_0 - h_0)})^{-1}$, with k and x_0 being the parameters of the fit. Figure 3 presents an example fit to the simulated data with 1σ errors on the $h_0^{95\%}$ estimate marked in red.

[6]For the $h_0^{95\%}$ fitting procedure, we use the PYTHON 3 [77] SCIPY-OPTIMIZE [78] CURVE_FIT package, implementing the Levenberg-Marquardt least squares algorithm, to obtain the best fitted parameters, x_0 and k, to the sigmoid function. Errors of parameters δx_0 and δk are obtained from the covariance matrix and used to calculate the standard deviation σ_e of the detection efficiency as a function of h_0, i.e., the confidence bands around the central values of the fit. In practice, we use the UNCERTAINTIES package [79] to obtain the $\pm 1\sigma$ standard deviation on the h_0 value.

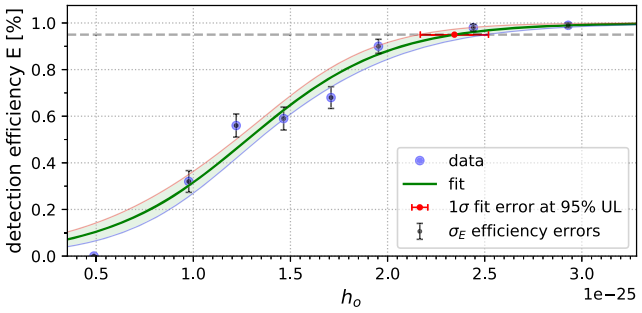

FIG. 3. Example sigmoid function fit (green solid line) to the injected data efficiencies (blue dots), representing the detection efficiency E as a function of injected GW amplitude h_0 used in *Time-Domain* $\mathcal{F}$-*statistic* search. Pale red and blue curves mark the 1σ confidence band obtained from the uncertainty of the fit. Red error bar marks the $\pm 1\sigma$ standard deviation on the $h_0^{95\%}$ value, corresponding to the efficiency of 0.95 (indicated by the horizontal dashed gray line). Vertical errors for each efficiency represent 1σ standard binomial errors related to detection rate, $\sigma_E = \sqrt{E(1-E)/N_i}$, where E is the efficiency and $N_i = 100$ is the number of injections for each GW amplitude. The data shown relates to the subband with the frequency of the lower edge of the band equal to 725.95 Hz.

D. *SOAP*

SOAP [49] is a fast, model-agnostic search for long duration signals based on the Viterbi algorithm [80]. It is intended as both a rapid initial search for isolated NSs, quickly providing candidates for other search methods to investigate further, as well as a method to identify long duration signals which may not follow the standard CW frequency evolution. In its most simple form *SOAP* analyzes a spectrogram to find the continuous time-frequency track which gives the highest sum of fast Fourier transform power. If there is a signal present within the data then this track is the most likely to correspond to that signal. The search pipeline consists of three main stages, the initial *SOAP* search [49], the postprocessing step using convolutional neural networks [81], and a parameter estimation stage.

1. Data preparation

The data used for this search starts as calibrated detector data which is used to create a set of FFTs with a coherence time of 1800 s. The power spectrum of these FFTs are then summed over one day, i.e., every 48 FFTs. Assuming that the signal remains within a single bin over the day, this averages out the antenna pattern modulation and increases the SNR in a given frequency bin. As the frequency of a CW signal increases, the magnitude of the daily Doppler modulation also increases, therefore the assumption that a signal remains in a single frequency bin within one day no longer holds. Therefore, the analysis is split into four separate bands (40–500, 500–1000, 1000–1500, and 1500–2000 Hz) where for each band the Doppler modulations are

accounted for by taking the sum of the power in adjacent frequency bins. For the bands starting at 40, 500, 1000, and 1500 Hz, the sum is taken over every one (no change), two, three, and four adjacent bins, respectively, such that the resulting time-frequency plane has one, two, three, or four times the width of bin. The data is then split further into "subbands" of widths 0.1, 0.2, 0.3, and 0.4 Hz wide respective to the four band sizes above. These increase in width such that the maximum yearly Doppler shift $\Delta f_{\mathrm{orb}}^{(\mathrm{max})}$ is half the subband width, where the maximum is given by

$$\Delta f_{\mathrm{orb}}^{(\mathrm{max})} = f\frac{v_{\mathrm{orb}}^{(\mathrm{max})}}{c} \approx 10^{-4} f, \tag{16}$$

where $v_{\mathrm{orb}}^{(\mathrm{max})}$ is the maximum orbital velocity of the Earth relative to the source, c is the speed of light, and f is the initial pulsar frequency. Each of the subbands are overlapping by half of the subband width such that any signal should be fully contained within a subband.

2. Search pipeline

SOAP searches through each of the summed and narrow banded spectrograms described in Sec. IV D 1 by rapidly identifying the track through the time frequency plane which gives the maximum sum of some statistic. In this search the statistic used is known as the "line aware" statistic [49], which uses multiple detectors data to compute the Bayesian statistic $p(\mathrm{signal})/[p(\mathrm{noise}) + p(\mathrm{line})]$, penalizing instrumental linelike combinations of spectrogram powers. Since each of the four bands described in Sec. IV D 1 take the sum of a different number of FFT bins, the χ^2 distributions that make up the Bayesian statistic are adjusted such that they have $2 \times N \times M$ degrees of freedom, where M is the number of summed frequency bins and N is the number of summed time segments.

SOAP then returns three main outputs for each subband: the Viterbi track, the Viterbi statistic, and a Viterbi map. The Viterbi track is the time-frequency track which gives the maximum sum of statistics along the track and is used for the parameter estimation stage in Sec. IV D 5. The Viterbi statistic is the sum of the individual statistics along the track, and is one of the measures used to determine the candidates for follow-up in Sec. IV D 4. The Viterbi map is a time-frequency map of the statistics in every time-frequency bin which has been normalized along every time step. This is representative of the probability distribution of the signal frequency conditional on the time step and is used as input to the convolutional networks described in Sec. IV D 3.

3. Convolutional neural network postprocessing

One post processing step in *SOAP* consists of convolutional neural networks (CNNs) which take in combinations of three data types: the Viterbi map, the two detectors spectrograms, and the Viterbi statistic. The aim of this technique is to improve the sensitivity to isolated neutron stars by reducing the impact of instrumental artifacts on the detection statistic. This part of the analysis does add some model dependency, so it is limited to search for signals that follow the standard CW frequency evolution. The structure of the networks are described in [81], where the output is a detection statistic which lies between 0 and 1. These are trained on $\sim 1 \times 10^5$ examples of continuous wave signals injected into real data, where the data is split in the same way as described in Sec. IV D 1. Each of the subbands is duplicated and a simulated continuous GW is injected into one of the two subbands such that the network has an example of noise and noise + signal cases. The sky positions, the frequency, frequency derivative, polarization, cosine of the inclination angle and SNR of the injected signals are all uniformly drawn in the ranges described in [81]. These signals are then injected into real O3 data before the data processing steps described in Sec. IV D 1. As the neural network should not be trained and tested on the same data, each of the training subbands are split into two categories ("odd" and "even"), where the subbands are placed in these categories alternately such that an "odd" subband is adjacent to two "even" subbands. This allows a network to be trained on "odd" subbands and tested on "even" subbands and vice versa. The outputs from each of these networks can be combined and used as another detection statistic to be further analyzed as described in Sec. IV D 4.

4. Candidate selection

At this stage there is a set of Viterbi statistics and CNN statistics for each subband that is analyzed, from which a set of candidate signals need to be selected for follow-up. Before doing this, any subbands which contain known instrumental artifacts are removed from the analysis. The subbands corresponding to the top 1% of the Viterbi statistics from each of the four analysis bands are then combined with the subbands corresponding to the top 1% of CNN statistics, leaving us with a maximum of 2% of the subbands as candidates. It is at this point where we begin to reject candidates by manually removing subbands which contain clear instrumental artifacts and still crossed the detection threshold for either the Viterbi or CNN statistic. There are a number of features we use to reject candidates including: strong detector artifacts which only appear in a single detectors spectrogram, broad ($> 1/5$ subband width) long duration signals, individual time-frequency bins which contribute large amounts to the final statistic and very high power signals in both detectors. Examples of these features can be seen in Sec. 6.3 of [82]. Any remaining candidates are then passed on for parameter estimation.

5. Parameter estimation

The parameter estimation stage uses the Viterbi track to estimate the Doppler parameters of the potential source.

Due to the complicated and correlated noise which appears in the Viterbi tracks, defining a likelihood is challenging. To avoid this difficulty, likelihood-free methods are used, in particular a machine learning method known as a conditional variational autoencoder. This technique was originally developed for parameter estimation of compact binary coalescence signals [83], and can return Bayesian posteriors rapidly (< 1 s). In our implementation, the conditional variational autoencoder is trained on isolated NS signals injected into many subbands, and returns an estimate of the Bayesian posterior in the frequency, frequency derivative, and sky position [84]. This acts both as a further check that the track is consistent with that of an isolated NS, and provides a smaller parameter space for a followup search.

V. RESULTS

In this section we summarize the results of the search obtained by the four pipelines. Each pipelines presents candidates obtained during the analysis and the results of the follow-up of the promising candidates. The upper limits on the GW strain are determined for each of the search procedures. There is also a study of the hardware injections of continuous wave signals added to the data. During the O3 run 18 hardware injections were added to the LIGO data. The injections are denoted by ip$N$ where N is the consecutive number of the injections. The amplitudes of the injections added in the O3 run were significantly lower than those added in previous observing runs. Consequently the injections were more difficult to detect.

A. *FrequencyHough*

Outliers produced by the *FrequencyHough* search are followed-up with the procedure described in Sec. IV A 1. The increase in FFT duration sets the sensitivity gain of the follow-up step and it is mainly limited by the resulting computational load, which increases with the fourth power of T_{FFT} for a fixed follow-up volume. Moreover, T_{FFT} cannot be longer than about one sidereal day, because the current procedure is not able to properly deal with the sidereal splitting of the signal power, which would cause a sensitivity loss.

All the coincident outliers produced by the *FrequencyHough* transform stage in the first frequency band, 10–128 Hz, have been followed-up. On the remaining frequency bands, from 128 up to 2048 Hz, only outliers with $CR \geq 5$ (computed over the *FrequencyHough* map) in both detectors have been followed-up. This selection was also applied for pairs of coincident outliers produced in the L1-Virgo and H1-Virgo detectors in the frequency band 10–128 Hz.

Table VI summarize the results of the first follow-up stage over coincident H1-L1 outliers, for each of the four analyzed frequency bands, given in the first column. The second columns is the value of T_{FFT} used at this stage, N_{i} the initial number of outliers to which the follow-up is applied. Subsequent columns indicate the number of candidates removed by the various vetoes, indicated as $V_{\mathrm{i}}, i = 1, \ldots 5$ and discussed in the Sec. IV A 1. The last column shows the number of outliers surviving the first follow-up stage. As it can be seen from the last column, 29 outliers survive this follow-up stage. Table VII shows the same quantities for the follow-up of coincident H1-Virgo and L1-Virgo outliers, which have been selected in the lowest frequency band, from 10 to 128 Hz. In this case, all the outliers have been discarded. Outliers which survived the first follow-up stage have been analyzed with a second step based on the same procedure as before but with a further increase in the FFT duration, which has been roughly doubled. The main quantities for the second follow-up stage are shown in Table VIII. The eight outliers in the band 512–1024 Hz are due to *hardware injection* ip1. An example is shown in Fig. 4, where the peakmap after Doppler correction is plotted for a small frequency range around the outlier frequency. Although the outlier parameters are relatively far from those of ip1, it is expected, especially in the case of a strong signal like this that—due to parameter correlations—outliers can

TABLE VI. Main quantities regarding the first follow-up stage for H1-L1 coincident outliers. T_{FFT} is the FFT duration used in the follow-up, N_{i} is the initial number of outliers to which the follow-up is applied, while $V_{\mathrm{i}}, i = 1, \ldots 5$ indicate the number of outliers removed by the subsequent vetoes. N_{s} is the number of outliers surviving the first follow-up stage.

Band (Hz)	T_{FFT} (s)	N_{i}	V1	V2	V3	V4	V5	N_{s}
10–128	24576	4007	3988	4	0	2	10	3
128–512	24576	12439	12422	0	1	13	3	0
512–1024	8192	10033	10017	1	0	5	2	8
1024–2048	8192	7440	7413	2	0	2	5	18

TABLE VII. Main quantities regarding the first follow-up stage for H1-Virgo (LH-AV) and L1-Virgo (LL-AV) coincident outliers. The shown quantities are the same as for Table VI. The corresponding frequency band is 10–128 Hz.

Detector	Band (Hz)	T_{FFT} (s)	N_{i}	V1	V2	V3	V4	V5	N_{s}
LL-AV	10–128	24576	1132	1127	4	0	0	1	0
LH-AV	10–128	24576	1143	1132	10	0	1	0	0

TABLE VIII. Main quantities regarding the second follow-up stage for H1-L1 surviving outliers.

Band (Hz)	$Tfft(s)$	N_i	V1	V2	V3	V4	V5	N_s
10–128	49152	3	3	0	0	0	0	0
512–1024	16384	8	0	0	0	0	8	0
1024–2048	16384	18	16	0	0	0	2	0

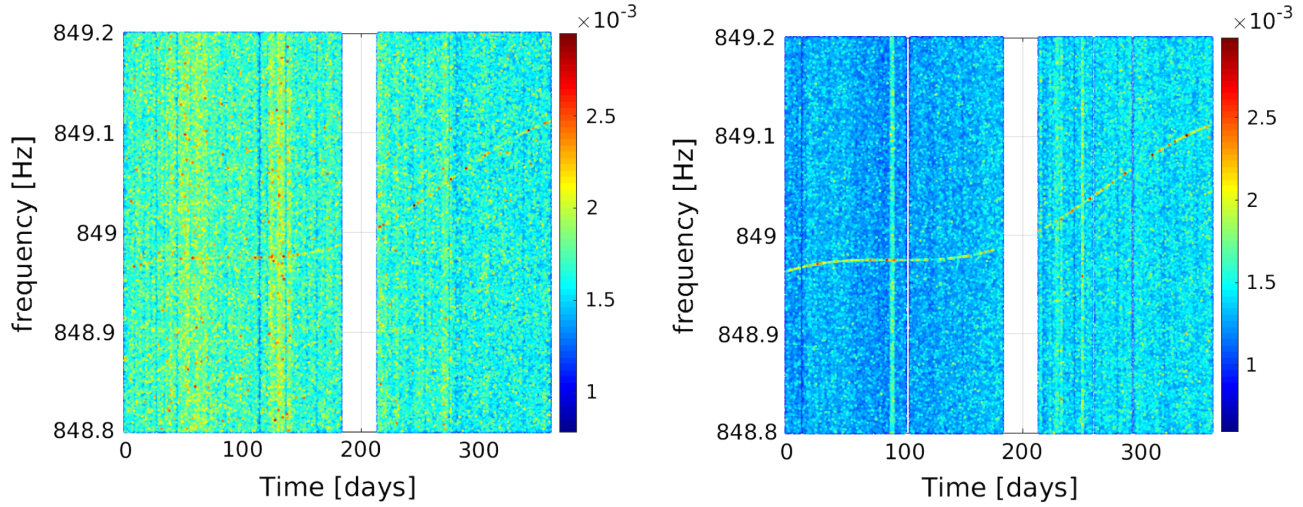

FIG. 4. Peakmap of H1 (left) and L1 (right) data showing one of the eight outliers removed by veto V5 in the second follow-up step, see Table VI. All the eight outliers were generated by the hardware injection ip1. A Doppler correction, with parameters not exactly equal with those of the signal, nevertheless aligns some of the signal peaks, thus producing an excess of counts in the *FrequencyHough* map.

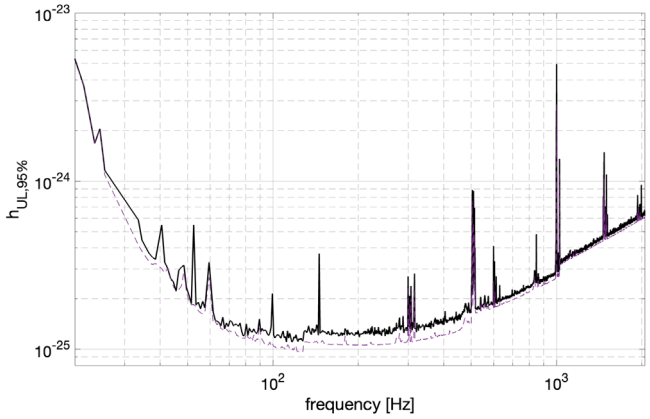

FIG. 5. O3 conservative upper limit estimation (bold continuous curve) and sensitivity lower bound (light dashed curve) for the *FrequencyHough* search.

spread over a rather large portion of the parameter space around the exact signal.

1. Upper limits

Having concluded that no candidate has a likely astrophysical origin, we have computed upper limits following the method described in Sec. IV A 3. Results are shown in Fig. 5. Although the search has been carried with a minimum frequency of 10 Hz, due to the unreliable calibration below 20 Hz, upper limits are given starting from this minimum frequency. The bold continuous curve represents our conservative upper limit estimation, computed on 1 Hz subbands and based on the maximum CR, while the lighter dashed curve is a (nonconservative) lower bound, obtained using the minimum CR in each subband. We expect the search sensitivity, defined as the minimum detectable strain amplitude, to be comprised among the two

TABLE IX. Hardware injection recovery by the *FrequencyHough* pipeline. The second column indicates the total distance metric among the injection and the corresponding strongest analysis candidate. Columns 3–6 give the error values for the individual parameters (frequency, spin-down, ecliptical longitude, and latitude). Column 7 indicate the CR of the strongest candidate corresponding to each injection, and the last column gives the expected number of candidates due to noise, having the same (or bigger) CR value, after taking into account the trial factor. All the reported values are the mean of individual values found separately in Livingston and Hanford detectors, with the exception of the CR and N_n for ip3, indicated by an asterisk, for which the reported values refer to Livingston alone. This hardware injection is very weak and it was confidently detected, after the first follow-up stage, only in Livingston, which has a better sensitivity at the injection frequency.

Injection	d_{FH}	Δf (Hz)	$\Delta \dot{f}$ (nHz/s)	$\Delta\lambda$ (deg)	$\Delta\beta$ (deg)	CR	N_n
ip1	0.77	1.15×10^{-4}	15.11×10^{-3}	0.015	−0.027	51.76	0
ip3	1.05	4.88×10^{-5}	3.52×10^{-3}	0.088	−0.377	6.34*	0.04
ip5	1.92	2.65×10^{-5}	9.64×10^{-3}	0.615	−0.130	41.58	0
ip6	0.16	9.27×10^{-6}	1.31×10^{-3}	0.009	0.045	56.05	0
ip14	1.52	5.77×10^{-4}	52.27×10^{-3}	0.054	0.521	20.58	0

TABLE X. Summary of candidates processed by each of the veto and follow-up stages of the *SkyHough* search.

Search stage	Candidates	% removed
Clustering	456000	
Line veto	414459	9%
$2\mathcal{F}$ threshold	3767	99%
Stage 0 vs Stage 1	697	18%
Stage 1 vs Stage 2	172	75%
Stage 3 vs Stage 3	90	48%
Stage 3 vs Stage 4	48	47%
Stage 4 vs Stage 5	36	25%

curves. The minimum upper limit is about 1.1×10^{-25}, at 116.5 Hz.

The search distance reach, expressed as a relation between the absolute value of the first frequency derivative and the frequency of detectable sources for various source distances, under the assumption the GW emission is the only spin-down mechanism (NSs in this case are often dubbed as *gravitars* [85]), is shown in Fig. 16.

2. Hardware injections

Table IX shows the error of the recovered signal with respect to the hardware injections. The reported values have been obtained at the end of the first follow-up stage, which

TABLE XI. Surviving candidates of the *SkyHough* multistage MCMC follow-up using PYFSTAT. $2\tilde{\mathcal{F}}$ corresponds to the loudest fully coherent $\mathcal{F}$-*statistic* value of the MCMC run. Band index corresponds to a frequency of $(65 + 0.025 \times \text{Band})$ Hz. Reference time is GPS 1238166018.

Band	Candidate	f (Hz)	$\dot{f}$ (nHz/s)	α (rad)	δ (rad)	$2\tilde{\mathcal{F}}$	Comment
834	4	85.872761414	2.41584×10^{-3}	3.143782737	1.165116066	30.54	Broad spectral feature in H1
834	9	85.873653124	-9.35774×10^{-2}	3.409549407	1.385107830	36.25	Broad spectral feature in H1
1227	35	95.697667346	-4.89489×10^{-2}	1.593327050	−1.292111453	31.53	Narrow spectral feature in H1
1229	5	95.725474979	-9.63949×10^{-1}	0.260240661	−1.008336167	30.87	Narrow spectral feature in H1
1754	1	108.857159405	-8.04825×10^{-7}	3.113189707	−0.583577133	1055.70	Hardware injection ip3
1754	2	108.857159406	-8.29209×10^{-7}	3.113189734	−0.583577139	1055.69	Hardware injection ip3
1754	5	108.857159404	-7.43862×10^{-7}	3.113189647	−0.583577277	1055.71	Hardware injection ip3
1754	10	108.857159405	-7.92726×10^{-7}	3.113189663	−0.583577189	1055.71	Hardware injection ip3
1754	13	108.857159406	-8.38377×10^{-7}	3.113189745	−0.583577097	1055.69	Hardware injection ip3
1754	14	108.857159405	-8.14434×10^{-7}	3.113189656	−0.583577155	1055.69	Hardware injection ip3
1754	34	108.857159404	-7.09929×10^{-7}	3.113189613	−0.583577327	1055.69	Hardware injection ip3
7251	10	246.297680589	-2.24806×10^{-2}	1.425124776	−1.242786654	35.79	Narrow spectral feature in H1
8022	0	265.575086278	-4.14962×10^{-3}	1.248816426	−0.981180252	1543.70	Hardware injection ip0
8022	1	265.575086279	-4.14969×10^{-3}	1.248816468	−0.981180265	1543.68	Hardware injection ip0
8022	2	265.575086278	-4.14961×10^{-3}	1.248816419	−0.981180239	1543.69	Hardware injection ip0
8022	3	265.575086278	-4.14964×10^{-3}	1.248816434	−0.981180252	1543.69	Hardware injection ip0
8022	4	265.575086278	-4.14964×10^{-3}	1.248816444	−0.981180252	1543.70	Hardware injection ip0
8022	5	265.575086277	-4.14958×10^{-3}	1.248816405	−0.981180243	1543.70	Hardware injection ip0
8022	7	265.575086279	-4.14968×10^{-3}	1.248816456	−0.981180263	1543.69	Hardware injection ip0
8022	28	265.575086278	-4.14965×10^{-3}	1.248816441	−0.981180257	1543.69	Hardware injection ip0
8023	0	265.575086278	-4.14964×10^{-3}	1.248816439	−0.981180255	1543.70	Hardware injection ip0
8023	1	265.575086278	-4.14961×10^{-3}	1.248816417	−0.981180250	1543.70	Hardware injection ip0
8023	3	265.575086278	-4.14966×10^{-3}	1.248816464	−0.981180249	1543.68	Hardware injection ip0
8023	4	265.575086279	-4.14969×10^{-3}	1.248816466	−0.981180264	1543.68	Hardware injection ip0
8023	7	265.575086279	-4.14967×10^{-3}	1.248816448	−0.981180256	1543.69	Hardware injection ip0
8023	8	265.575086279	-4.14966×10^{-3}	1.248816453	−0.981180260	1543.71	Hardware injection ip0
8023	9	265.575086278	-4.14963×10^{-3}	1.248816431	−0.981180254	1543.70	Hardware injection ip0
8023	10	265.575086275	-4.14945×10^{-3}	1.248816284	−0.981180203	1543.26	Hardware injection ip0
8023	11	265.575086278	-4.14962×10^{-3}	1.248816419	−0.981180255	1543.69	Hardware injection ip0
8023	12	265.575086278	-4.14963×10^{-3}	1.248816435	−0.981180249	1543.70	Hardware injection ip0
8023	13	265.575086277	-4.14956×10^{-3}	1.248816392	−0.981180234	1543.66	Hardware injection ip0
8023	14	265.575086278	-4.14966×10^{-3}	1.248816450	−0.981180252	1543.70	Hardware injection ip0
8023	16	265.575086278	-4.14962×10^{-3}	1.248816403	−0.981180252	1543.65	Hardware injection ip0
8023	18	265.575086278	-4.14962×10^{-3}	1.248816430	−0.981180248	1543.66	Hardware injection ip0
8023	19	265.575086278	-4.14963×10^{-3}	1.248816436	−0.981180254	1543.72	Hardware injection ip0
8023	34	265.575086278	-4.14965×10^{-3}	1.248816452	−0.981180250	1543.72	Hardware injection ip0

TABLE XII. Hardware injection recovery by the *SkyHough* pipeline. For each hardware injection within search range we report the dimension-wise errors with respect to loudest surviving candidate of the follow-up.

Injection	$2\tilde{\mathcal{F}}$	Δf (Hz)	$\Delta \dot{f}$ (nHz/s)	$\Delta\alpha$ (rad)	$\Delta\delta$ (rad)	$\Delta\alpha$ (deg)	$\Delta\delta$ (deg)
ip0	1543.72	-4.80×10^{-9}	3.52×10^{-7}	-2.82×10^{-7}	-2.49×10^{-8}	-1.62×10^{-5}	-1.43×10^{-6}
ip3	1055.71	1.16×10^{-8}	-7.29×10^{-7}	9.35×10^{-7}	1.53×10^{-6}	5.35×10^{-5}	8.74×10^{-5}

was enough to confidently detect the reported signals. The second column gives the total distance metric, defined in Sec. IV A, among the injection and the corresponding strongest analysis candidate. Columns 3–6 give the error values for the individual parameters. Column 7 indicates the CR of the strongest candidate corresponding to each injection, and the last column gives the expected number of candidates due to noise, having the same (or bigger) CR value, after taking into account the trial factor. As shown in the table, we have been able to detect five injections in the analyzed parameter space and the estimated parameters do show a good agreement with the injected ones. All reported values are the mean of the values obtained separately for the Livingston and Hanford detectors, with the exception of the CR and N_n for ip3, for which the reported values refer to Livingston alone. This hardware injection is in fact very weak and it was confidently detected, after the first follow-up stage, only in Livingston detector, which has a better sensitivity at the injection frequency.

B. *SkyHough*

1. Candidate follow-up

Table X summarizes the number of outliers discarded by each of the veto and follow-up stages employed in this search. A total of 36 candidates survive the complete suite of veto and follow-up stages of the *SkyHough* pipeline. Candidates can be grouped into two sets according to their corresponding $\mathcal{F}$-*statistic* value: 31 candidates present a value of $2\tilde{\mathcal{F}} \sim \mathcal{O}(10^3)$, while the remaining five candidates only achieve $2\tilde{\mathcal{F}} \sim \mathcal{O}(30)$. Their corresponding parameters are collected in Table XI.

The 31 strong candidates present consistent values with the only two hardware injections within the *SkyHough* search range: 24 candidates are ascribed to the hardware injection ip0, while 7 candidates are ascribed to the hardware injection ip3. Parameter deviation of the loudest candidate associated to each injection are reported in Table XII.

The five weaker candidates are manually inspected using the segment-wise $\mathcal{F}$-*statistic* on 660 coherent segments, in a similar manner to that in [39,67].

The first pair of candidates is found around 85.850 Hz, where the H1 detector presents a broad spectral feature. As shown in Fig. 6, their single-detector $\mathcal{F}$-*statistic* is more prominent in the H1 detector rather than the L1 detector, and scores over the multidetector $\mathcal{F}$-*statistic*. These characteristics point towards an instrumental, rather than astrophysical, origin.

A second pair of candidates is found around 95.7 Hz. This frequency band is populated by narrow spectral artifacts of unknown origin in the H1 detector. Correspondingly, as shown in Fig. 7, the single-detector $\mathcal{F}$-*statistic* is prominent in the H1 detector rather than the L1 detector. Due to the narrowness of the feature, in this case the accumulation is better localized around a fraction of the run. As in the previous case, the single-detector $\mathcal{F}$-*statistic* scores over the multidetector $\mathcal{F}$-*statistic*. These characteristics point towards an instrumental origin.

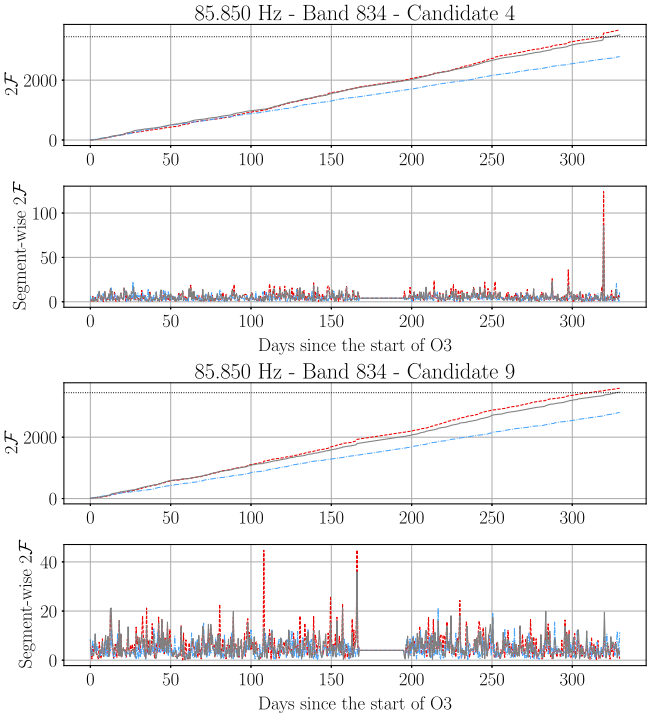

FIG. 6. *SkyHough* candidates consistent with a broad spectral artifact in the H1 detector. Upper panel shows the cumulative semicoherent $\mathcal{F}$-*statistic* using 660 coherent segments ($T_{\mathrm{coh}} = 0.5$ days). Lower panel shows the segment-wise $\mathcal{F}$-*statistic*. Dashed red line represents the single-detector $\mathcal{F}$-*statistic* using H1-only data; the dot-dashed blue line represents the single-detector $\mathcal{F}$-*statistic* using L1-only data. Solid gray line represents the multidetector $\mathcal{F}$-*statistic*. Dotted horizontal line represents the threshold of $2\mathcal{F} = 3450$ set at the initial follow-up stage.

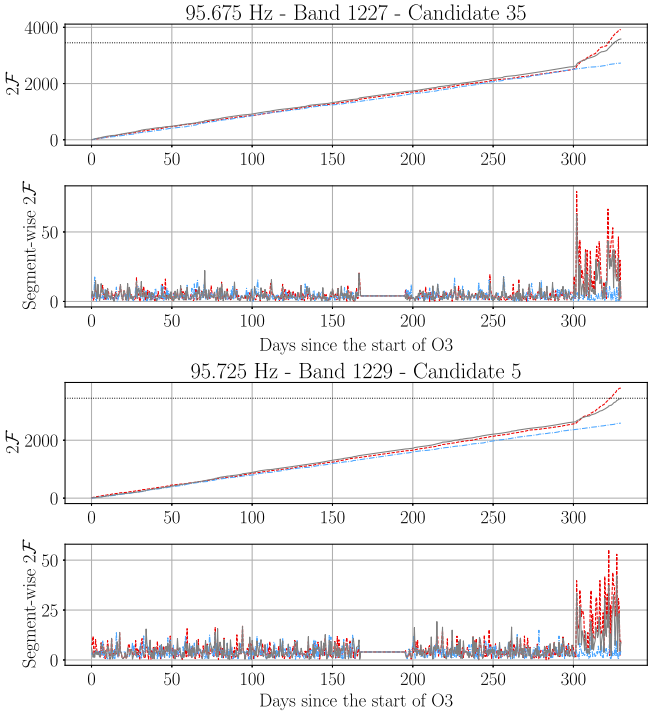

FIG. 7. *SkyHough* candidate consistent with two narrow spectral artifacts of unknown origin in the H1 detector. The legend is equivalent to that of Fig. 6.

The last weak candidate in the vicinity of 246.275 Hz, where the H1 detector presents another narrow spectral artifact of unknown origin, is shown in Fig. 8. The single-detector $\mathcal{F}$-*statistic* is more prominent in the H1 detector than in the L1 detector, and accumulates rapidly at the beginning of the run. As in the previous cases, this behavior is consistent with that of an instrumental artifact.

This concludes the analysis of surviving candidates of the *SkyHough* pipeline. Every single one of them could be related to an instrumental feature.

2. Sensitivity estimation

We estimate the search sensitivity following the same procedure as previous searches [31,32,34,40,41]. Search sensitivity is quantified using the *sensitivity depth* [86,87]

$$\mathcal{D} = \frac{\sqrt{S_{\mathrm{n}}}}{h_0}, \tag{17}$$

where S_{n} represents the power spectral density (PSD) of the data, computed as the inverse squared average of the individual SFT's running-median PSD [41,61]

$$S_{\mathrm{n}}(f) = \sqrt{\frac{N_\alpha}{\sum_\alpha [S_\alpha(f)]^{-2}}}. \tag{18}$$

where S_α represents the running-median noise floor estimation using 101 bins from the SFT labeled by starting

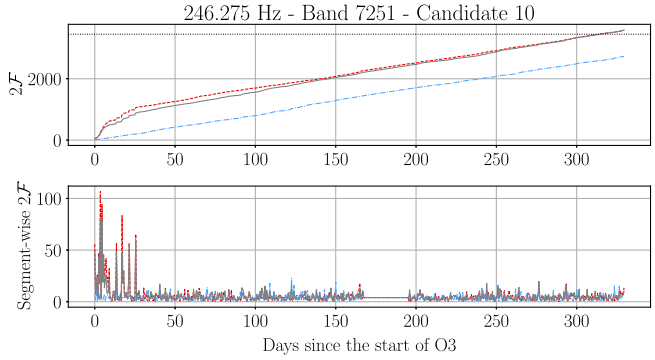

FIG. 8. *SkyHough* candidate consistent with a narrow spectral artifact of unknown origin in the H1 detector. The legend is equivalent to that of Fig. 6.

time t_α (including SFTs from both the H1 and L1 detectors) and N_α represents the total number of SFTs. The resulting amplitude spectral density (ASD) $\sqrt{S_{\mathrm{n}}}$ is shown in Fig. 9.

The sensitivity depth $\mathcal{D}^{95\%}$ corresponding to a 95% average detection rate is characterized by adding a campaign of software-simulated signals into the data. Simulated signals are added into 150 representative frequency bands at several sensitivity depth values bracketing the $\mathcal{D}^{95\%}$ value in each band, as represented in Fig. 10. For each sensitivity depth, 200 simulated signals drawn from uniform distribution in phase and amplitude parameters are added into the data. The *SkyHough* is run on each of these signals in order to evaluate how many of them are detected, and the resulting top lists are clustered using the same configuration as in the main stage of the search.

For each simulated signal, we retrieve the best 40 resulting clusters. The following two criteria must be fulfilled in order to label a simulated signal as "detected." First, the loudest significance of at least one of the selected clusters must be higher than the minimum significance recovered by the

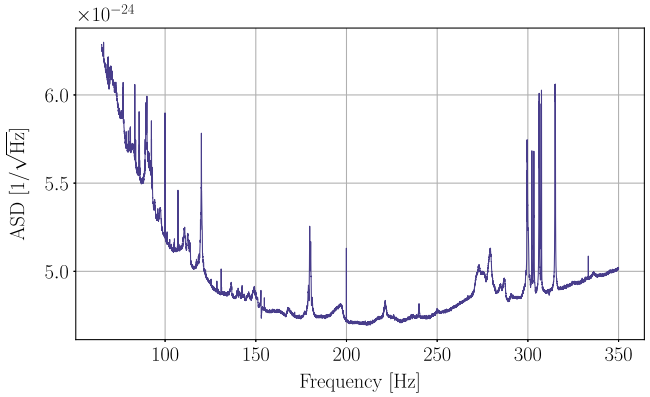

FIG. 9. ASD employed by the *SkyHough* pipeline to estimate the sensitivity of the search. ASD is computed as the square root of the single-sided inverse-square averaged PSD using data from both the H1 and L1 advanced LIGO detectors, as explained in the text surrounding Eq. (18).

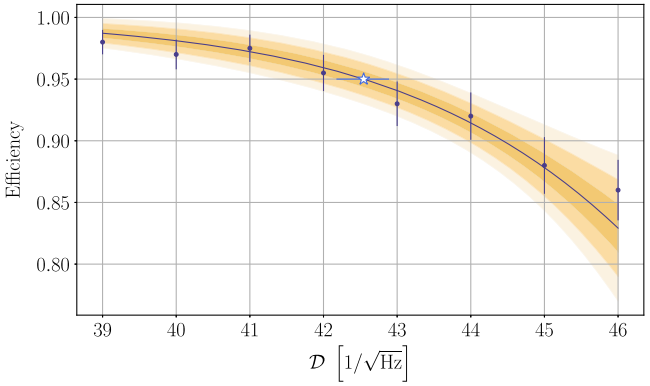

FIG. 10. Example computation of $\mathcal{D}^{95\%}$ (white star) at a frequency band by fitting a sigmoid function (blue solid line) to a set of efficiencies (blue dots) computed using 200 injections at each sensitivity depth for the *SkyHough* search. Shaded regions represent 1, 2, and 3 sigma envelopes of the sigmoid fit. Error bars are computed as discussed in the main text.

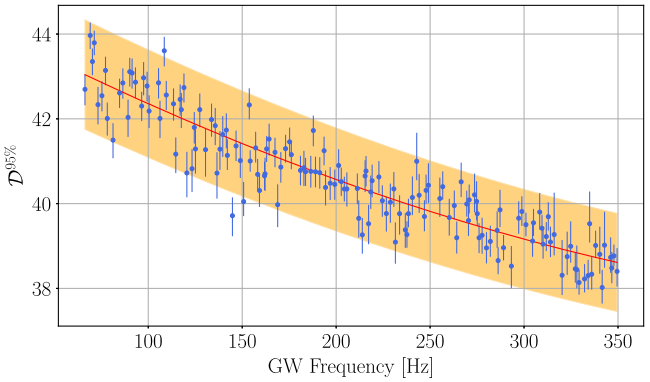

FIG. 11. Wide-band interpolation $\mathcal{D}^{95\%}(f)$ of the results obtained by the *SkyHough* pipeline. Each dot represents a $\mathcal{D}^{95\%}$ at a particular frequency band computed using the procedure exemplified in Fig. 10. The red solid line represents a nonparametric interpolation using a Gaussian process regression, as discussed in the main text. The shaded region represents a 3% relative error with respect to the interpolation and corresponds to the 98% credible interval.

corresponding all-sky clustering; this ensures the signal is significant enough to be selected for a follow-up stage. Second, the parameters of the loudest candidate in said clusters must be closer than two parameter-space bins [see Eq. (7) and Table III] from the simulated-signal's parameter, as otherwise the follow-up would have missed the signal.

The efficiency associated to each sensitivity depth E is computed as the fraction of simulated signals labeled as detected. A binomial uncertainty δE is associated to each efficiency

$$\delta E = \sqrt{\frac{E \cdot (1-E)}{N_{\mathrm{I}}}}, \tag{19}$$

where $N_{\mathrm{I}} = 200$ represents the number of signals. Then, we use SCIPY's CURVE_FIT function [78] to fit a sigmoid curve to the data given by

$$S(\mathcal{D}; a, b) = 1 - \frac{1}{1 + \exp\left(-a\mathcal{D} + b\right)}, \tag{20}$$

where a, b represent the parameters to adjust. After fitting, this expression can be numerically inverted to obtain $\mathcal{D}^{95\%}$. The uncertainty associated to the fit is compute through the covariance matrix C as[7]

$$\delta\mathcal{D}^{95\%} = \sqrt{\left(\frac{\partial S}{\partial a}\right)^2 C_{aa} + 2\left(\frac{\partial S}{\partial a}\right)\left(\frac{\partial S}{\partial b}\right) C_{ab} + \left(\frac{\partial S}{\partial b}\right)^2 C_{bb}}. \tag{21}$$

This procedure is exemplified in Fig. 10.

[7]This method is akin to that employed by the *SkyHough* search in [34]. We note that Eq. (19) in [41] is incorrect and should be equivalent to Eq. (21) in this document. This is just a typographical error, as the analysis was performed using the correct formulas.

We compute the average wide-band $\mathcal{D}^{95\%}(f)$ value using Gaussian process regression, as shown in Fig. 11. We fit a Gaussian process using to the ensemble of $\mathcal{D}^{95\%}$ obtained from the injection campaign using SCIKIT-LEARN's GAUSSIANPROCESSREGRESSOR with an RBF kernel [88]. The uncertainty associated to the fit is computed as the 98% credible region of the deviations with respect to the Gaussian process regression, which corresponds to a 3% relative uncertainty. Equation (17) allows us to translate $\mathcal{D}^{95\%}(f)$ into a corresonding CW amplitude $h_0^{95\%}(f)$, shown in Fig. 12.

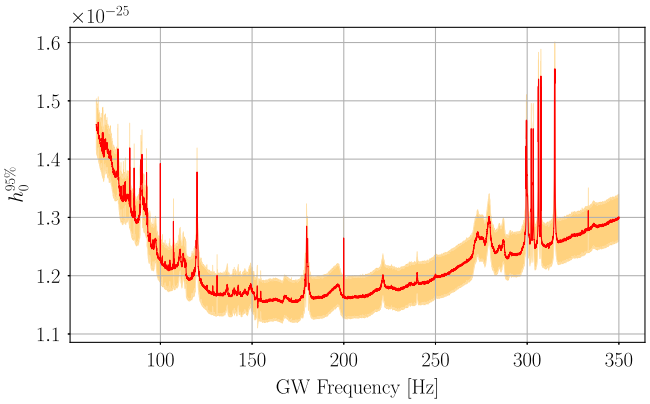

FIG. 12. CW amplitude $h_0^{95\%}$ corresponding to the 95% detection efficiency depth along the frequency band analyzed by the *SkyHough* pipeline. Solid line represents the implied $h_0^{95\%}$ from the wide-band $\mathcal{D}^{95\%}$ interpolation shown in Fig. 11. Shaded region corresponds to the 3% relative error with respect to the interpolation.

TABLE XIII. Hardware injection recovery with the *Time-Domain $\mathcal{F}$-statistic* pipeline. The first column is the injection index ip$N$, where N is the injection number. The last four columns are the differences between the true values of the parameters of the injected signal ipN and the parameters of the most significant candidate in the subband where injection is added. The second column is the false alarm probability associated with the topmost candidate.

Injection	FAP	Δf (Hz)	$\Delta \dot{f}$ (nHz/s)	$\Delta\delta$ (deg)	$\Delta\alpha$ (deg)
ip10	$< 10^{-8}$	7.73×10^{-4}	3.91×10^{-3}	0.74	1.51
ip11	$< 10^{-8}$	6.20×10^{-3}	7.22×10^{-2}	14.78	248.13
ip5	$< 10^{-8}$	1.62×10^{-4}	6.64×10^{-2}	30.24	24.83
ip3	0.997	5.21×10^{-2}	5.21×10^{-2}	3.85	1.56
ip0	0.055	1.84×10^{-1}	1.15×10^{-1}	18.94	20.98
ip2	0.275	4.41×10^{-5}	9.28×10^{-3}	1.12	0.074

C. *Time-Domain $\mathcal{F}$-statistic*

In the frequency bandwidth of [20, 750] Hz that we analyze we have 3245 subbands that are 0.25 Hz wide and that are overlapped by 0.025 Hz. 104 subbands were not analyzed because of the excessive noise originating mainly from the first harmonic of the violin mode, first and second harmonics of the beam splitter violin mode, and 60 Hz mains line and its harmonics. This leads to the loss of around 23.50 Hz of the band. Moreover, we have vetoed lines identified by the detector characterization group. This leads to an additional 34.18 Hz band loss. Thus altogether 57.68 Hz of the band was vetoed, which constitutes 7.9% of the 730 Hz band analyzed. Consequently we searched 3141 subbands. For each subband we analyzed coherently 41 six-day time segments with the *$\mathcal{F}$-statistic*. As a result with our *$\mathcal{F}$-statistic* threshold of 15.5 we obtained 5.47×10^{10} candidates.

In the second stage of the analysis for each subband we search for coincidences among the candidates from the 41 time-domain segments. For each subband and each hemisphere we find the candidate with the smallest coincidence false alarm probability, i.e., the most significant candidate. As a result we have 6282 top candidates from our search. Among the top candidates we consider a candidate to be statistically significant if the coincidence false alarm probability is less than 1%. This leads to the selection of 311 candidates that we call *outliers*. The outliers were subject to further investigation to determine whether they can be considered as true GW events. Three of the outliers were determined to be "artificial" GW signals injected in hardware to the LIGO detectors data.

1. Hardware injections

In the parameter space analyzed by *Time-Domain $\mathcal{F}$-statistic* only six hardware injections were present. These are injections ip0, ip2, ip3, ip5, ip10, and ip11. In Table XIII we have compared the parameters of the top candidates obtained in our search in the frequency subbands, where the injections were made, with the parameters of the injections. In the table we show the false alarm probability of coincidence of the top candidates and the difference between the parameters of the candidate and the parameters of the injections. We see that the two injections ip5 and ip10 are detected with a very high confidence. Their false alarm probability is close to 0 and the errors in the parameter estimation are small. The top candidate in the band where injection ip11 is located has a very small false alarm probability; however, the right ascension of the candidate differs very much from the true value the right ascension of the injection. A close analysis shows that this candidate is associated with a strong line present in the Hanford detector. The line frequency is different from the hardware injection frequency by only around 10 mHz. The amplitude of the injection ip11 is very low. Its SNR in the six-day segments that we analyze coherently with *$\mathcal{F}$-statistic* is around 4. This is considerably lower than our threshold SNR of around 5.2 and it is not surprising that the injection is not recovered. For the remaining three bands we see that the top candidates have parameters very close to the parameters of the hardware injections ip0, ip2, and ip3; however their false alarm probabilities are greater than 1% and we cannot consider these injections as detected. The SNRs of the two detected injections ip5 and ip10 is considerably above our threshold of 5.2, whereas SNRs of the three remaining injections ip0, ip2, and ip3 are close to our threshold and they could not be detected.

2. Outliers

We have identified 311 outliers in our search. For these outliers the probability of being due to accidental coincidence between the candidates from the 41 time segments is less than 1%.

In our search we have vetoed the lines of known origin identified in LIGO detectors. However, the LIGO data contained additional lines and interferences. In order to identify the origin of the outliers in our search we have performed three independent investigations. First we compared our outliers with the lines of unknown origin identified by the LIGO data characterization group. Second we have performed an independent search for strictly periodic signals in all the six-day time-domain segments that we analyzed in our search. We have searched

TABLE XIV. Outlier associated with the hardware injection ip6.

Injection	FAP	Δf (Hz)	$\Delta \dot{f}$ (nHz/s)	$\Delta\delta$ (deg)	$\Delta\alpha$ (deg)
ip6	4.02×10^{-8}	1.54×10^{-2}	2.26	36.59	314.54

for periodic signals separately in the data from the Hanford and the Livingston LIGO detector. Thirdly we have performed a visual inspection of the outliers by searching the data with $\mathcal{F}$*-statistic* around the outliers separately in the two LIGO detectors. In addition we have checked whether outliers are around the frequencies associated with the suspension violin mode 1st harmonic around 500 Hz and the beam splitter violin mode first and second harmonics around 300 and 600 Hz, respectively. As a result of the above study 204 outliers were found to be associated with lines and interferences present in the detector. They were classified as follows: 146 originated from the Hanford detector and 21 were associated with the Livingston detector. One line that appeared in both detectors was the 20 Hz tooth of the 1 Hz comb known to be present in both detectors. Thirty-six outliers were associated with the two violin mode resonances. Two outliers are pulsar injections ip5 and ip10 that were confidently detected and they are described in Sec. V C 1.

One of the outliers was associated with the pulsar injection ip6. The frequency of the outlier was only 15 mHz from the frequency of the injection. The injected signal ip6 has a spin-down of -6.73×10^{-9} Hz/s, which is outside our search range. However, the SNR of the injection was around 17 for each of the six-day segments that we analyzed. This resulted in a sufficiently strong correlation to give a significant signal; however, with the spin down and the sky position of the outlier very much displaced from the true values (see Table XIV).

The 102 outliers that could not be associated with interferences in the detector or hardware injections appeared with frequencies on the left edges of the 0.25 Hz subbands of the narrow band segments that we analyzed. To determine whether these are artifacts or they warrant a further detailed follow-up, we regenerated the narrow band data where the artifacts occurred, however with the offset frequencies decreased by 0.125 Hz (half of the width of the subband). Consequently the outliers that appeared at the left edges of the subbands, should now be present approximately in the middle of the subband. We have then performed a search with our pipeline around the parameters of the outliers. None of the outliers were found to be significant. The smallest false probability was found to be around 59%.

As a result we were left with two outliers for a more detailed study, with parameters given in Table XV. We followed up the outliers in the data segments that are twice as long as the original segments. For each subband where the outliers are present we divided the data into 12-day segments, and we performed the search around the position of the outliers. A twofold increase of the coherence times would result in the increase of the signal-to-noise ratio of a true GW signal by a factor of $\sqrt{2}$. We performed a coherent search ± 16 grid points in spin down and ± 4 points in the sky position around the point of the parameter space where the outliers should be present. We then performed a coincidence search. For the two cases we did not find a significant coincidence. The probability that the best coincidence was accidental was close to 1.

TABLE XV. Outliers of unknown origin from the *Time-Domain* $\mathcal{F}$*-statistic* analysis.

f (Hz)	$\dot{f}$ (nHz/s)	δ (deg)	α (deg)	FAP
83.52	-6.58×10^{-1}	−18.08	179.16	0.0094
726.07	-3.30×10^{-2}	58.07	190.79	0.0034

3. Upper limits

The analysis of the outliers described in Secs. V C 1 and V C 2 has not revealed a viable candidate for a GW event. We therefore proceeded to establish upper limits on the amplitude of GW signals in our search. We establish upper limits in each subband analyzed and for each hemisphere by using the procedure described in Sec. IV C 2 (as a result periodic interferences in the data for 201 subbands out of 3141 that we analyzed we were not able to establish upper limits). The 95% confidence upper limits $h_0^{95\%}$ for analysis of LIGO O3 data presented in the paper are plotted in Fig. 13 in comparison with upper limits obtained with our pipeline in O1 and O2 data. We see a considerable improvement which is more than the improvement in the sensitivity of LIGO data. This additional improvement in our pipeline sensitivity is around $1/3$ and it is mainly due to changes in the coincidence algorithm. The biggest improvement for frequencies above 450 Hz is due to the longer coherence time of six days used in the search, compared to the coherence time of two days used in our O2 search above 450 Hz.

D. *SOAP*

SOAP was run on the O3 dataset from 40–2000 Hz where we are sensitive to a broad range of signals from the entire sky. To contain an entire signal within a single subband, its spin-down must be within $\pm \sim 10^{-9}$ Hz/s up to 1000 Hz and $\pm \sim 10^{-8}$ Hz/s above 1000 Hz, therefore when values are outside this range we lose sensitivity. We

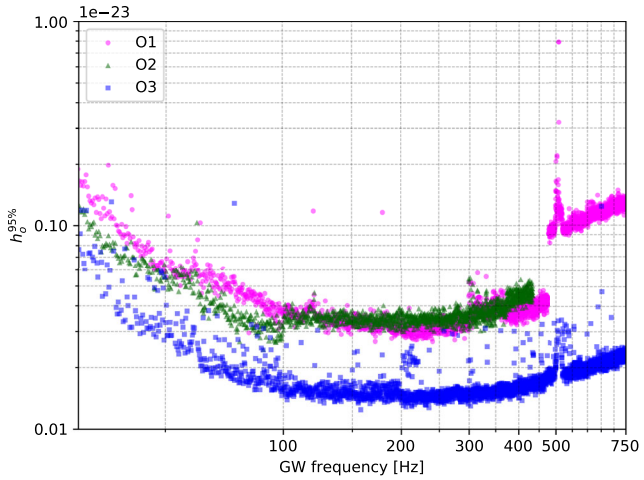

FIG. 13. Comparison of 95% confidence upper limits on GW amplitude h_0 obtained with the *Time-Domain $\mathcal{F}$-statistic* pipeline in the analysis of Advanced LIGO data. The magenta circles, green triangles, and blue squares represent the $h_0^{95\%}$ upper limits in 0.25 Hz sub-bands of the O1, O2, and O3 data, respectively.

start from a set of 1800s long FFT of cleaned time series data from the two LIGO detectors H1 and L1. As described in Sec. IV D 1, the FFT are normalized to the running median of width 100 bins before being split into 0.1 (0.2, 0.3, 0.4) Hz wide subbands overlapping by half of their width. For each of the subbands, time segments and frequency bins are summed together, where along the time axis, 48 FFT (1 day) are summed along the frequency axis, and every 1 (2, 3, 4) frequency bins are summed respective to the analysis band. *SOAP* is then run on each of these subbands, returning the Viterbi statistic, Viterbi map, and Viterbi tracks, which can be input to the CNN to return a second statistic. The number of subbands searched totals to 19868 across all four analysis bands, where for each band (40–500, 500–1000, 1000–1500, 1500–2000) Hz the respective total is (9200, 5040, 3263, 2362). Subbands which contained known instrumental lines identified by the calibration group are then removed from the analysis leaving a total number of subbands as 17929, with each separate band containing (8297, 4494, 2952, 2186) subbands. Candidates are then selected by taking the subbands which contribute to the top 1% of both the remaining Viterbi and CNN statistics. These candidates can then be investigated further to identify whether a real GW signal is present. Subbands which contain an instrumental line identified by the calibration group but also cross the 1% threshold are also investigated to check whether it is the instrumental line which causes the high statistic value. There were 293 subbands which were in this category, and in 291 subbands the Viterbi tracks closely follow the instrumental line, and the remaining two contained both an instrumental line and a hardware injection (ip5). These were then reintroduced into the analysis as the Viterbi tracks did not follow that of the instrumental line. From the total of the 17929 subbands, 248 were selected for a followup investigation where 107 of these subbands cross the thresholds of both the Viterbi and CNN statistics.

1. Outliers

The 248 candidates are then investigated further by analysing the outputs of the Viterbi search, i.e., the Viterbi maps, Viterbi tracks and Viterbi statistics, alongside the CNN statistic and the spectrograms from each detector. Plots of each of these allow the identification of features which are not astrophysical but originate from the instrument or environment. The spectrograms from both detectors summed over time and frequency, as described in Sec. IV D 1, along with the optimal Viterbi track, allow us to identify what features within the data contribute towards the final statistic. For example, many of the spectrograms contain spectral features which are far above the noise level and appear in only a single detector, but still crosses the detection threshold for one of the statistics. These subbands can be visually inspected, and if found to contain a nonastrophysical artifact which contributes to the statistic is removed from the analysis. Of the subbands that were investigated further, 242 were removed due to the presence of an instrumental artifact. These range from broad spectral lines which last the entire observing run to short duration [$\mathcal{O}$(days)] high power events which contribute large amounts of power to the statistic. The remaining subbands contain fake CW signals which were injected into the hardware of the detector.

2. Hardware injections

In O3 there are a total of 18 hardware injections, where nine fall within our search parameter space and two of these (ip1 and ip5) appear in subbands which cross our detection threshold without being excluded. These signals appear in multiple subbands due to the 50% overlap, therefore the subband containing a larger fraction of the signal is used for followup. Two additional injections outside of our "sensitive" range for $\dot{f}$ also crossed our detection thresholds (ip4 and ip6) as *SOAP* identified the part of the signal which crossed the search band. Of the seven injections we did not detect, two are in binary systems which we are less likely to detect as this search was optimized for isolated NSs. The remaining missed injections have SNRs which are below our expected sensitivity for isolated NSs, therefore would not be expected to cross our threshold. The two remaining hardware injections crossed the detection threshold for both the Viterbi statistic or the CNN statistic. These candidates were then followed up using the parameter estimation method described in Sec. IV D 5, where we correctly recover the injected parameters of the injections.

3. Sensitivity

The sensitivity of *SOAP* can be tested by running the search on a set of CW signals injected into real O3 data.

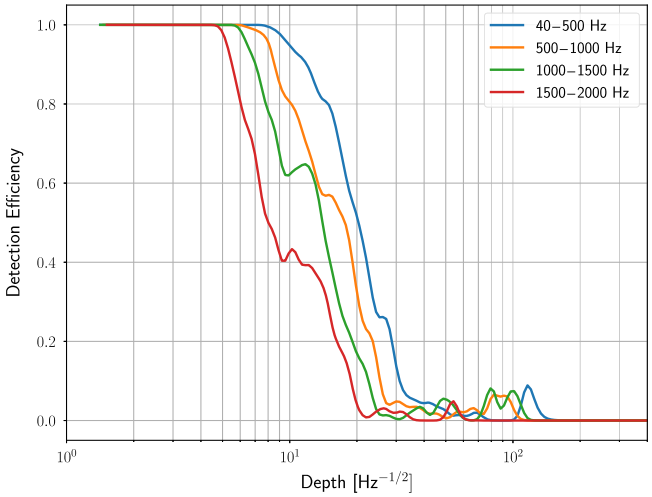

FIG. 14. Detection efficiencies of the *SOAP* + CNN search on isolated NS signals injected into real O3 data. These are shown as a function of the sensitivity depth for the four different frequency ranges described in Sec. IV D 1. The efficiencies are calculated with a false alarm rate of 1%.

A total of 3.3×10^4 signals are injected across each of the four frequency bands described in Sec. IV D 1, where the signals have Doppler parameters which are drawn uniformly on the sky, uniformly within the respective frequency range and uniformly in the range $[-10^{-9}, 0]$ Hz s^{-1} for the frequency derivative. The other amplitude parameters varied in the same ranges as described in Sec. IV D 3. A false alarm value of 1% can be set for each of the odd and even datasets within the four analysis bands by taking the corresponding statistic value at which 1% of the noise only bands exceed. Both the Viterbi and CNN statistics are calculated separately for each of the odd and even bands. Each of the bands containing injected signals can then be classified as detected or not depending on if a statistic crossed its respective false alarm value. These classified statistics can then be combined together to produce an efficiency curve shown in Fig. 14, which show the fraction of detected signals at a given sensitivity depth, defined in Eq. (17). At a false alarm value of 1% and a detection efficiency of 95% we are sensitive to signals with a depth of 9.9, 8.0, 6.5, and 5.3 Hz$^{-1/2}$ for the frequency bands 40–500, 500–1000, 1000–1500, and 1500–2000 Hz, respectively. To further investigate our sensitivity, we split each of the four analysis bands into smaller bands ranging from 20 Hz wide at lower frequency to 100 Hz wide at higher frequencies. For each of these bands a detection efficiency curve is generated in the same way as for the sensitivity depth above, however, they are now generated for values of h_0. The false alarm values for each band are set based on which of the four larger analysis bands that it falls within. Our false alarm values are then contaminated by the strongest artifacts within each 500 Hz wide analysis band, meaning that this is a conservative estimate of our sensitivity. The error on these curves is found using the

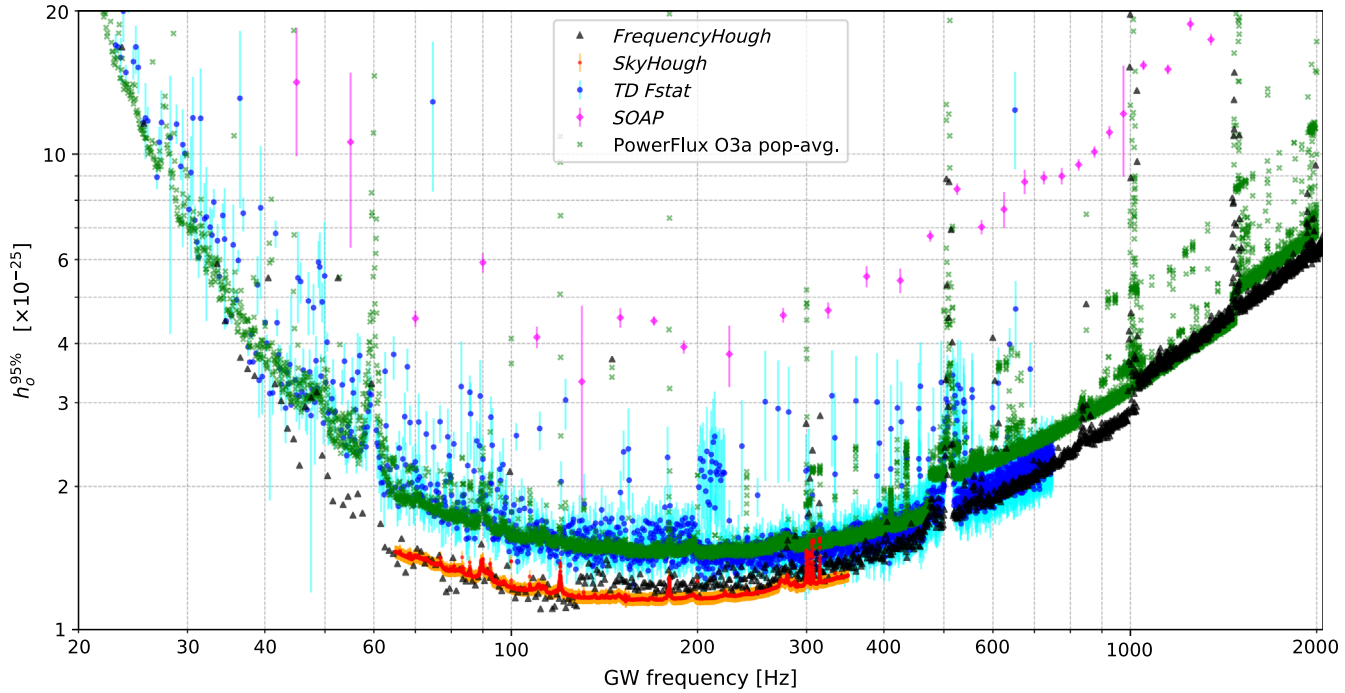

FIG. 15. Comparison of broadband search sensitivities obtained by the *FrequencyHough* pipeline (black triangles), the *SkyHough* pipeline (red squares), the *Time-Domain $\mathcal{F}$-statistic* pipeline (blue circles), and the *SOAP* pipeline (magenta diamonds). Vertical bars mark errors of h_0 obtained in the procedures described in Secs. IV and V. Population-averaged upper limits obtained in [39] using the O3a data are marked with dark-green crosses.

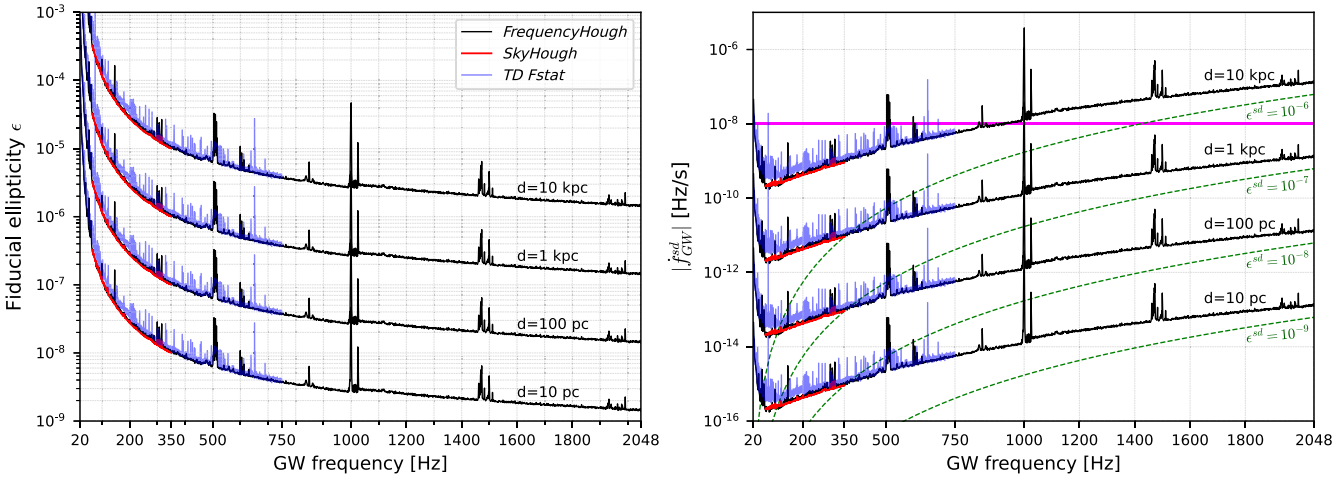

FIG. 16. Left panel: detectable ellipticity, given by Eq. (22), as a function of the GW frequency for neutron stars with the "canonical" moment of inertia $I_{zz} = 10^{38}$ kg m^2 at a distance of 10 kpc, 1 kpc, 100 pc, and 10 pc (from top to bottom). Results for the *FrequencyHough* pipeline are marked in black, *SkyHough* in red and for *Time-Domain* $\mathcal{F}$*-statistic* in blue. The right panel shows the relation between the absolute value of the first GW frequency derivative $\dot{f} = 2\dot{f}_{\rm rot}$ and the GW frequency $f = 2f_{\rm rot}$ (with $f_{\rm rot}$ the rotational frequency) of detectable sources as a function of the distance, assuming their spin-down is due solely to the emission of GWs. Constant spin-down ellipticities ϵ^{sd}, corresponding to this condition, are denoted by dashed green curves. The magenta horizontal line marks the maximum spin down searched.

binomial error on each of the points as defined in Eq. (19), giving two bounds on our efficiency curves. Values of h_0 for each frequency band can then be selected where the detection efficiency reaches 95%, defining our sensitivity shown in Fig. 15.

VI. CONCLUSIONS

In Fig. 15 we summarize 95% confidence-level upper limits on strain amplitude h_0 for the four pipelines used in this search. The upper limits obtained improve on those obtained using the PowerFlux method in early O3 LIGO data [39]. Our results constitute the most sensitive all-sky search to date for continuous GWs in the range 20–2000 Hz while probing spin-down magnitudes as high as 1×10^{-8} Hz/s. Only the O2 Falcon search [37,38,89] provides a better sensitivity in the frequency range 20–2000 Hz; however it does so with a dramatically reduced frequency derivative range. In the frequency range of [20, 500] Hz Falcon searches a $\dot{f}$ range from -3×10^{-13} Hz/s to 3×10^{-13} Hz/s and $\dot{f}$ range upto $[-7.5 \times 10^{-12}, 3 \times 10^{-12}]$ Hz/s for frequencies above 500 Hz. Thus the Falcon search parameter space is smaller than ours by factor of $\sim 1.8 \times 10^4$ below 500 Hz and factor of 10^3 above 500 Hz. A recent search for persistent narrowband gravitational waves using radiometer analysis of combined O1, O2, and O3 LIGO and Virgo data in the frequency range of 20–1726 Hz [90] has not revealed any significant signals and has reported upper limits on an *equivalent* strain amplitude in the range of $(0.030–9.6) \times 10^{-24}$. As briefly discussed in [90], the radiometer search is expected to be significantly less sensitive than our CW searches for two reasons. First, the former uses frequency bins much larger than the latter [1/32 Hz vs O(mHz)], thus collecting more noise in each bin. Second, it does not take into account the Doppler effect due to the Earth motion, which causes a spread of the signal power over several bins (especially at higher frequencies), thus producing a further sensitivity loss.

We can use the amplitude h_0 given by Eq. (2) to calculate star's ellipticity ϵ,

$$\epsilon = \frac{c^4}{4\pi^2 G}\frac{h_0 d}{I_{zz} f^2} \approx 9.46 \times 10^{-6}\left(\frac{h_0}{10^{-25}}\right) \times \left(\frac{10^{38}\ \text{kg m}^2}{I_{zz}}\right)\left(\frac{100\ \text{Hz}}{f}\right)^2\left(\frac{d}{1\ \text{kpc}}\right). \quad (22)$$

Using the above equation the upper limits on the GW strain amplitude h_0 can be converted to upper limits on the ellipticity ϵ. The results are plotted in Fig. 16 (left panel) for four representative values of the distance d and they provide astrophysically interesting results. The NSs with ellipticities above a given trace and distance value corresponding to the trace in the left panel of Fig. 16 would be detectable by our searches. For instance, at frequency 200 Hz we would be able to detect a CW signal from a NS within a distance of 100 pc if its ellipticity were at least 3×10^{-7}. Similarly, in the middle frequency range, around 550 Hz, we would be able to detect the CW signal up to a distance of 1 kpc, with $\epsilon > 5 \times 10^{-7}$. Finally at higher frequencies, around 1550 Hz, the same signal would be detectable up to a distance of 10 kpc if $\epsilon > 2 \times 10^{-6}$. These levels of ellipticity are below the maximum value of the

ellipticity that may be supported by the crust of a NS described by a standard equation of state reported in [91–93]. However they are above the most recent estimates in general relativity by [94,95]. The latter do not, however, exclude larger values of ellipticity when additional physical processes, such as plastic flow in the crust, are taken into account. Our upper limits are starting to probe the range predicted for pulsars by the models of [96], which predict ellipticities up to $\epsilon \approx 10^{-7}$–10^{-6} for younger stars in which the deformation is not supported by crustal rigidity, but by a nonaxisymmetric magnetic field at the end of its Hall driven evolution in the crust. Note however that for known pulsars at a distance of a few kpc, such as the Crab, the signal would be at frequencies $f \lesssim 100$ Hz, so still beyond the reach of our searches.

Another way of representing limits on ellipticity is shown in the right panel of Fig. 16. Assuming that the emission of gravitational radiation is the sole energy loss mechanism for a rotating NS, we obtain the so-called spin-down limit h_0^{sd} on the amplitude h_0, see Eqs. (7)–(9) of [97]:

$$h_0^{\mathrm{sd}} = \frac{1}{d}\left(\frac{5}{2}\frac{GI_{zz}}{c^3}\frac{|\dot{f}|}{f}\right)^{1/2} \approx 2.55\times10^{-25}\left(\frac{1\ \mathrm{kpc}}{d}\right) \times \left(\frac{I_{zz}}{10^{38}\ \mathrm{kg\,m^2}}\right)^{1/2}\left(\frac{100\ \mathrm{Hz}}{f}\right)^{1/2}\left(\frac{|\dot{f}|}{10^{-11}\ \mathrm{Hz\,s^{-1}}}\right)^{1/2}. \tag{23}$$

Inverting the above equation and replacing the spin-down limit amplitude h_0^{sd} with our upper limit amplitudes $h_0^{95\%}$ we have the following relation between the frequency derivative and frequency:

$$|\dot{f}| = \frac{2c^3}{5G}\frac{(h_0^{95\%}d)^2 f}{I_{zz}} \approx 1.54\times10^{-10}\left(\frac{h_0^{95\%}}{10^{-24}}\right)^2 \times \left(\frac{10^{38}\ \mathrm{kg\,m^2}}{I_{zz}}\right)\left(\frac{f}{100\ \mathrm{Hz}}\right)\left(\frac{d}{1\ \mathrm{kpc}}\right)^2. \tag{24}$$

In the right panel of Fig. 16 we have plotted $|\dot{f}|$ as a function of frequency f for several representative values of the distance d and for a canonical value of the moment of inertia. The NSs with $|\dot{f}|$ above a given trace and distance value corresponding to the trace in the right panel of Fig. 16 would be detectable by our searches.

By equating Eq. (2) for the amplitude h_0 and Eq. (23) for the spin-down limit, we obtain the following equation for $\dot{f}$:

$$|\dot{f}| = \frac{32\pi^4 G}{5c^5}\epsilon^2 I_{zz} f^5 \approx 1.72\times10^{-14}\left(\frac{\epsilon}{10^{-6}}\right)^2 \times \left(\frac{I_{zz}}{10^{38}\ \mathrm{kg\,m^2}}\right)\left(\frac{f}{100\ \mathrm{Hz}}\right)^5. \tag{25}$$

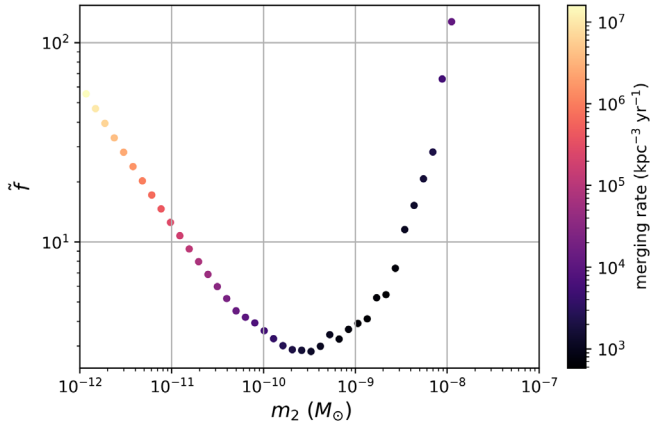

FIG. 17. Constraints on $\tilde{f}$, a quantity that, if less than one, indicates the sensitivity to a given f_{pbh}, and inspiraling rate (color) as a function of the secondary mass, with a primary mass $m_1 = 2.5\ M_\odot$, assuming a monochromatic mass function for m_1, no rate suppression, and $f_{\mathrm{pbh}} = 1$. These constraints are valid at distances of $\mathcal{O}(\mathrm{pc})$.

The dashed lines in the right panel of Fig. 16 are constant ellipticity curves from Eq. (25) above. These lines are independent of the distance d.

In addition to constraints on ellipticities of isolated NSs, we can make statements about the rate and abundance of inspiraling planetary-mass and asteroid-mass PBHs [29]. The upper limits presented in Fig. 15 are *generic*: they can be applied to any quasimonochromatic, persistent GW that follows a linear frequency evolution over time and whose frequency derivative lies within the search range. Based on these all-sky searches, GW signals from inspiralling PBH binaries with chirp masses less than $\mathcal{O}(10^{-5})M_\odot$ and GW frequencies less than ∼250 Hz would be identical to those arising from nonaxisymmetric rotating NSs. Following the procedure presented in [30], and using the *FrequencyHough* upper limits in Fig. 5, which cover the widest range of spin-down/spin-up, we obtain constraints on highly asymmetric mass ratio binary systems, assuming that one object in the binary has a mass $m_1 = 2.5\ M_\odot$, motivated by the QCD phase transition [11,26,98]. In Fig. 17, we plot constraints on the merging rates and an effective parameter, $\tilde{f}$, that, if less than one, indicates the sensitivity to the fraction of dark matter that PBHs could compose, f_{pbh}, as a function of the companion mass m_2:

$$\tilde{f}^{53/37} \equiv f_{\mathrm{sup}} f(m_1) f(m_2) f_{\mathrm{pbh}}^{53/37}, \tag{26}$$

where f_{sup} is a rate suppression factor, defined to be one, and $f(m_1)$ and $f(m_2)$ are the mass distribution functions for m_1 and m_2, respectively. We assume $f(m_1) = 1$, that is, a monochromatic mass function peaked at 2.5 $M_\odot$, and that $f_{\mathrm{pbh}} = 1$. Our results indicate that $\tilde{f}$ lies slightly above one for a wide range of asteroid-mass BHs within the distance range of $\mathcal{O}(\mathrm{pc})$. However, as the GW detectors become

more sensitive, and especially when future ground-based instruments come online, we will start to probe a physical regime of the PBH masses. Thus, these results not only imply a bright future for analyses for PBHs, but also motivate the expansion of CW techniques specifically adapted to search for planetary-mass inspiraling PBHs [29]. While the rates only depend on the distance reach of the search, i.e., they are model independent, the constraints on $\tilde{f}$ depend on particular models of PBH clustering or binary formation. Other models are certainly just as valid as those that we constrain here [99,100]; therefore, Fig. 17 should be seen as an example of the kinds of statements that could be made based on upper limits from CW searches, and not an absolute statement about the abundance and rates of PBHs.

ACKNOWLEDGMENTS

This material is based upon work supported by NSF's LIGO Laboratory, which is a major facility fully funded by the National Science Foundation. The authors also gratefully acknowledge the support of the Science and Technology Facilities Council (STFC) of the United Kingdom, the Max-Planck-Society (MPS), and the State of Niedersachsen/Germany for support of the construction of Advanced LIGO and construction and operation of the GEO 600 detector. Additional support for Advanced LIGO was provided by the Australian Research Council. The authors gratefully acknowledge the Italian Istituto Nazionale di Fisica Nucleare (INFN), the French Centre National de la Recherche Scientifique (CNRS) and the Netherlands Organization for Scientific Research (NWO), for the construction and operation of the Virgo detector and the creation and support of the EGO consortium. The authors also gratefully acknowledge research support from these agencies as well as by the Council of Scientific and Industrial Research of India, the Department of Science and Technology, India, the Science and Engineering Research Board (SERB), India, the Ministry of Human Resource Development, India, the Spanish Agencia Estatal de Investigación (AEI), the Spanish Ministerio de Ciencia e Innovación and Ministerio de Universidades, the Conselleria de Fons Europeus, Universitat i Cultura and the Direcció General de Política Universitaria i Recerca del Govern de les Illes Balears, the Conselleria d'Innovació, Universitats, Ciència i Societat Digital de la Generalitat Valenciana, and the CERCA Programme Generalitat de Catalunya, Spain, the National Science Centre of Poland and the European Union—European Regional Development Fund; Foundation for Polish Science (FNP), the Swiss National Science Foundation (SNSF), the Russian Foundation for Basic Research, the Russian Science Foundation, the European Commission, the European Social Funds (ESF), the European Regional Development Funds (ERDF), the Royal Society, the Scottish Funding Council, the Scottish Universities Physics Alliance, the Hungarian Scientific Research Fund (OTKA), the French Lyon Institute of Origins (LIO), the Belgian Fonds de la Recherche Scientifique (FRS-FNRS), Actions de Recherche Concertées (ARC) and Fonds Wetenschappelijk Onderzoek—Vlaanderen (FWO), Belgium, the Paris Île-de-France Region, the National Research, Development and Innovation Office Hungary (NKFIH), the National Research Foundation of Korea, the Natural Science and Engineering Research Council Canada, Canadian Foundation for Innovation (CFI), the Brazilian Ministry of Science, Technology, and Innovations, the International Center for Theoretical Physics South American Institute for Fundamental Research (ICTP-SAIFR), the Research Grants Council of Hong Kong, the National Natural Science Foundation of China (NSFC), the Leverhulme Trust, the Research Corporation, the Ministry of Science and Technology (MOST), Taiwan, the United States Department of Energy, and the Kavli Foundation. The authors gratefully acknowledge the support of the NSF, STFC, INFN, CNRS, and PL-Grid for provision of computational resources. This work was supported by MEXT, JSPS Leading-edge Research Infrastructure Program, JSPS Grant-in-Aid for Specially Promoted Research 26000005, JSPS Grant-in-Aid for Scientific Research on Innovative Areas 2905: JP17H06358, JP17H06361 and JP17H06364, JSPS Core-to-Core Program A. Advanced Research Networks, JSPS Grant-in-Aid for Scientific Research (S) 17H06133 and 20H05639, JSPS Grant-in-Aid for Transformative Research Areas (A) 20A203: JP20H05854, the joint research program of the Institute for Cosmic Ray Research, University of Tokyo, National Research Foundation (NRF), Computing Infrastructure Project of KISTI-GSDC, Korea Astronomy and Space Science Institute (KASI), and Ministry of Science and ICT (MSIT) in Korea, Academia Sinica (AS), AS Grid Center (ASGC) and the Ministry of Science and Technology (MoST) in Taiwan under grants including AS-CDA-105-M06, Advanced Technology Center (ATC) of NAOJ, and Mechanical Engineering Center of KEK.

APPENDIX: SCALING FACTORS FOR *FREQUENCYHOUGH* UPPER LIMITS

The "population average" upper limit formula given in Eq. (6) has been derived in [45]. It assumes an underlying population of sources randomly distributed in the sky, with a uniform distribution of the polarization angle ψ and of the cosine of the star's rotation axis inclination angle, ι, with respect to the line of sight. We show here how to obtain the scaling factor to be applied for a specific set of source parameters. The relevant term, which contains the dependence on the source parameters, is [see Eq. (B15) in [45]]

$$\mathcal{S}^2 = (A_+ F_+ + A_\times F_\times)^2. \tag{A1}$$

$F_+, F_\times$ are the time-dependent detector beam pattern functions, which can be expressed as

$$F_+(t) = a(t)\cos 2\psi + b(t)\sin 2\psi,$$
$$F_\times(t) = b(t)\cos 2\psi - a(t)\sin 2\psi, \tag{A2}$$

where $a(t)$, $b(t)$ explicit expressions are given, e.g., in [47]. The terms $A_+, A_\times$ are given by

$$A_+ = \frac{1+\cos^2\iota}{2},$$
$$A_\times = \cos\iota. \tag{A3}$$

Taking the average over all the source parameters, it can be found

$$\mathcal{S}^2_{\alpha,\delta,\psi,\iota} = \langle \mathcal{F}^2 \rangle_{\alpha,\delta,\psi,\iota} \simeq \frac{4}{25}, \tag{A4}$$

nearly independent of the specific detector being considered. If we consider a specific set of source parameters $(\alpha, \delta, \psi, \iota)$, then the only average we need to compute is over the time and we can write

$$\mathcal{S}^2_t = \langle F^2_+ \rangle_t \left(\frac{1+\cos^2\iota}{2}\right)^2 + \langle F^2_\times \rangle_t \cos^2\iota. \tag{A5}$$

The scaling factor by which the population average upper limit must be multiplied, in order to refer it to a specific set of source parameters, is

$$\mathcal{C} = \sqrt{\frac{\mathcal{S}^2_{\alpha,\delta,\psi,\iota}}{\mathcal{S}^2_t}}. \tag{A6}$$

[1] J. Aasi *et al.*, Advanced LIGO, Classical Quantum Gravity **32**, 074001 (2015).
[2] F. Acernese *et al.*, Advanced Virgo: A second-generation interferometric gravitational wave detector, Classical Quantum Gravity **32**, 024001 (2015).
[3] B. P. Abbott *et al.*, GWTC-1: A Gravitational-Wave Transient Catalog of Compact Binary Mergers Observed by LIGO and Virgo during the First and Second Observing Runs, Phys. Rev. X **9**, 031040 (2019).
[4] R. Abbott *et al.*, GWTC-2: Compact Binary Coalescences Observed by LIGO and Virgo during the First Half of the Third Observing Run, Phys. Rev. X **11**, 021053 (2021).
[5] R. Abbott *et al.*, Observation of gravitational waves from two neutron star-black hole coalescences, Astrophys. J. Lett. **915**, L5 (2021).
[6] Paul D. Lasky, Gravitational waves from neutron stars: A review, Pub. Astron. Soc. Aust. **32**, e034 (2015).
[7] Kostas Glampedakis and Leonardo Gualtieri, Gravitational waves from single neutron stars: An advanced detector era survey, Astrophysics and Space Science Library **457**, 673 (2018).
[8] Magdalena Sieniawska and Michał Bejger, Continuous gravitational waves from neutron stars: Current status and prospects, Universe **5**, 217 (2019).
[9] Maximiliano Isi, Matthew Pitkin, and Alan J. Weinstein, Probing dynamical gravity with the polarization of continuous gravitational waves, Phys. Rev. D **96**, 042001 (2017).
[10] Anne M. Green and Bradley J. Kavanagh, Primordial black holes as a dark matter candidate, J. Phys. G **48**, 043001 (2021).
[11] Sebastien Clesse and Juan Garcia-Bellido, GW190425, GW190521 and GW190814: Three candidate mergers of primordial black holes from the QCD epoch, Phys. Dark Universe **38**, 101111 (2022).
[12] Hiroko Niikura, Masahiro Takada, Shuichiro Yokoyama, Takahiro Sumi, and Shogo Masaki, Constraints on Earth-mass primordial black holes from OGLE 5-year microlensing events, Phys. Rev. D **99**, 083503 (2019).
[13] M. R. S. Hawkins, The signature of primordial black holes in the dark matter halos of galaxies, Astron. Astrophys. **633**, A107 (2020).
[14] Saloni Bhatiani, Xinyu Dai, and Eduardo Guerras, Confirmation of planet-mass objects in extragalactic systems, Astrophys. J. **885**, 77 (2019).
[15] Sebastien Clesse and Juan García-Bellido, Seven hints for primordial black hole dark matter, Phys. Dark Universe **22**, 137 (2018).
[16] C. Sivaram, Kenath Arun, and O. V. Kiren, Primordial planets predominantly of dark matter, Earth Moon Planets **122**, 115 (2019).
[17] Jakub Scholtz and James Unwin, What If Planet 9 Is a Primordial Black Hole?, Phys. Rev. Lett. **125**, 051103 (2020).
[18] Marek A. Abramowicz, Michał Bejger, and Maciek Wielgus, Collisions of neutron stars with primordial black holes as fast radio bursts engines, Astrophys. J. **868**, 17 (2018).
[19] B. P. Abbott *et al.*, Search for Subsolar Mass Ultracompact Binaries in Advanced LIGO's Second Observing Run, Phys. Rev. Lett. **123**, 161102 (2019).
[20] Khun Sang Phukon, Gregory Baltus, Sarah Caudill, Sebastien Clesse, Antoine Depasse, Maxime Fays, Heather Fong, Shasvath J. Kapadia, Ryan Magee, and Andres Jorge Tanasijczuk, The hunt for sub-solar primordial black holes in low mass ratio binaries is open, arXiv:2105.11449.
[21] Martti Raidal, Ville Vaskonen, and Hardi Veermäe, Gravitational waves from primordial black hole mergers, J. Cosmol. Astropart. Phys. 09 (2017) 037.
[22] Sai Wang, Yi-Fan Wang, Qing-Guo Huang, and Tjonnie G. F. Li, Constraints on the Primordial Black Hole Abundance from the First Advanced LIGO Observation Run

Using the Stochastic Gravitational-Wave Background, Phys. Rev. Lett. **120**, 191102 (2018).
[23] Juan García-Bellido and Sebastien Clesse, Constraints from microlensing experiments on clustered primordial black holes, Phys. Dark Universe **19**, 144 (2018).
[24] Josh Calcino, Juan Garcia-Bellido, and Tamara M. Davis, Updating the MACHO fraction of the Milky Way dark halowith improved mass models, Mon. Not. R. Astron. Soc. **479**, 2889 (2018).
[25] Konstantin M. Belotsky, Vyacheslav I. Dokuchaev, Yury N. Eroshenko, Ekaterina A. Esipova, Maxim Yu. Khlopov, Leonid A. Khromykh, Alexander A. Kirillov, Valeriy V. Nikulin, Sergey G. Rubin, and Igor V. Svadkovsky, Clusters of primordial black holes, Eur. Phys. J. C **79**, 246 (2019).
[26] Bernard Carr, Sebastien Clesse, Juan García-Bellido, and Florian Kühnel, Cosmic conundra explained by thermal history and primordial black holes, Phys. Dark Universe **31**, 100755 (2021).
[27] Manuel Trashorras, Juan García-Bellido, and Savvas Nesseris, The clustering dynamics of primordial black boles in *N*-body simulations, Universe **7**, 18 (2021).
[28] V. De Luca, V. Desjacques, G. Franciolini, and A. Riotto, The clustering evolution of primordial black holes, J. Cosmol. Astropart. Phys. 11 (2020) 028.
[29] Andrew L. Miller, Sébastien Clesse, Federico De Lillo, Giacomo Bruno, Antoine Depasse, and Andres Tanasijczuk, Probing planetary-mass primordial black holes with continuous gravitational waves, Phys. Dark Universe **32**, 100836 (2021).
[30] Andrew L. Miller, Nancy Aggarwal, Sébastien Clesse, and Federico De Lillo, Constraints on planetary and asteroid-mass primordial black holes from continuous gravitational-wave searches, Phys. Rev. D **105**, 062008 (2022).
[31] B. P. Abbott *et al.*, All-sky search for periodic gravitational waves in the O1 LIGO data, Phys. Rev. D **96**, 062002 (2017).
[32] B. P. Abbott *et al.*, Full band all-sky search for periodic gravitational waves in the O1 LIGO data, Phys. Rev. D **97**, 102003 (2018).
[33] B. P. Abbott *et al.*, First low-frequency Einstein@Home all-sky search for continuous gravitational waves in Advanced LIGO data, Phys. Rev. D **96**, 122004 (2017).
[34] B. P. Abbott *et al.*, All-sky search for continuous gravitational waves from isolated neutron stars using Advanced LIGO O2 data, Phys. Rev. D **100**, 024004 (2019).
[35] C. Palomba, S. D'Antonio, P. Astone, S. Frasca, G. Intini, I. La Rosa, P. Leaci, S. Mastrogiovanni, A. L. Miller, F. Muciaccia, O. J. Piccinni, L. Rei, and F. Simula, Direct Constraints on the Ultralight Boson Mass from Searches of Continuous Gravitational Waves, Phys. Rev. Lett. **123**, 171101 (2019).
[36] B. Steltner, M. A. Papa, H. B. Eggenstein, B. Allen, V. Dergachev, R. Prix, B. Machenschalk, S. Walsh, S. J. Zhu, O. Behnke, and S. Kwang, Einstein@Home all-sky search for continuous gravitational waves in LIGO O2 public data, Astrophys. J. **909**, 79 (2021).
[37] Vladimir Dergachev and Maria Alessandra Papa, Results from the First All-Sky Search for Continuous Gravitational Waves from Small-Ellipticity Sources, Phys. Rev. Lett. **125**, 171101 (2020).
[38] Vladimir Dergachev and Maria Alessandra Papa, Results from high-frequency all-sky search for continuous gravitational waves from small-ellipticity sources, Phys. Rev. D **103**, 063019 (2021).
[39] R. Abbott *et al.*, All-sky search for continuous gravitational waves from isolated neutron stars in the early O3 LIGO data, Phys. Rev. D **104**, 082004 (2021).
[40] P. B. Covas and Alicia M. Sintes, First All-Sky Search for Continuous Gravitational-Wave Signals from Unknown Neutron Stars in Binary Systems Using Advanced LIGO Data, Phys. Rev. Lett. **124**, 191102 (2020).
[41] R. Abbott *et al.*, All-sky search in early O3 LIGO data for continuous gravitational-wave signals from unknown neutron stars in binary systems, Phys. Rev. D **103**, 064017 (2021).
[42] Karl Wette, Liam Dunn, Patrick Clearwater, and Andrew Melatos, Deep exploration for continuous gravitational waves at 171–172 Hz in LIGO second observing run data, Phys. Rev. D **103**, 083020 (2021).
[43] R. Abbott *et al.*, All-sky search for gravitational wave emission from scalar boson clouds around spinning black holes in LIGO O3 data, Phys. Rev. D **105**, 102001 (2022).
[44] Rodrigo Tenorio, David Keitel, and Alicia M. Sintes, Search methods for continuous gravitational-wave signals from unknown sources in the advanced-detector era, Universe **7**, 474 (2021).
[45] Pia Astone, Alberto Colla, Sabrina D'Antonio, Sergio Frasca, and Cristiano Palomba, Method for all-sky searches of continuous gravitational wave signals using the frequency-Hough transform, Phys. Rev. D **90**, 042002 (2014).
[46] Badri Krishnan, Alicia M. Sintes, Maria Alessandra Papa, Bernard F. Schutz, Sergio Frasca, and Cristiano Palomba, Hough transform search for continuous gravitational waves, Phys. Rev. D **70**, 082001 (2004).
[47] Piotr Jaranowski, Andrzej Królak, and Bernard F. Schutz, Data analysis of gravitational-wave signals from spinning neutron stars: The signal and its detection, Phys. Rev. D **58**, 063001 (1998).
[48] J. Aasi *et al.*, Implementation of an F-statistic all-sky search for continuous gravitational waves in Virgo VSR1 data, Classical Quantum Gravity **31**, 165014 (2014).
[49] Joe Bayley, Chris Messenger, and Graham Woan, Generalized application of the Viterbi algorithm to searches for continuous gravitational-wave signals, Phys. Rev. D **100**, 023006 (2019).
[50] Ling Sun *et al.*, Characterization of systematic error in Advanced LIGO calibration, Classical Quantum Gravity **37**, 225008 (2020).
[51] Ling Sun *et al.*, Characterization of systematic error in Advanced LIGO calibration in the second half of O3, arXiv:2107.00129.
[52] F. Acernese *et al.*, Calibration of Advanced Virgo and reconstruction of detector strain h(t) during the observing run O3, Classical Quantum Gravity **39**, 045006 (2022).
[53] R. N. Manchester, G. B. Hobbs, A. Teoh, and M. Hobbs, The Australia Telescope National Facility Pulsar Catalogue, Astron. J. **129**, 1993 (2005).
[54] E. Goetz *et al.*, O3 lines and combs in found in self-gated c01 data, Technical Report No. T2100200-v2, LIGO, 2021, https://dcc.ligo.org/LIGO-T2100200/public.

[55] J. Aasi *et al.* (LIGO Scientific and Virgo Collaborations), First low-frequency all-sky search for continuous gravitational wave signals, Phys. Rev. D **93**, 042007 (2016).
[56] P. Astone, S. Frasca, and C. Palomba, The short FFT database and the peak map for the hierarchical search of periodic sources, Classical Quantum Gravity **22**, S1197 (2005).
[57] C. Palomba, P. Astone, and S. Frasca, Adaptive Hough transform for the search of periodic sources, Classical Quantum Gravity **22**, S1255 (2005).
[58] I. La Rosa, P. Astone, S. D'Antonio, S. Frasca, P. Leaci, A. L. Miller, C. Palomba, O. J. Piccinni, L. Pierini, and T. Regimbau, Continuous gravitational-wave data analysis with general purpose computing on graphic processing units, Universe **7**, 218 (2021).
[59] M. Di Cesare, All-sky gravitational wave searches for isolated neutron stars: Methods and applications to LIGO-Virgo data, Master's thesis, University of Rome Sapienza, 2021, https://web.infn.it/VirgoRoma/images/MartinaDiCesare_MDC_master_thesis.pdf.
[60] Alicia M. Sintes and Badri Krishnan, Improved hough search for gravitational wave pulsars, J. Phys. Conf. Ser. **32**, 206 (2006).
[61] B. Abbott *et al.*, All-sky search for periodic gravitational waves in LIGO S4 data, Phys. Rev. D **77**, 022001 (2008).
[62] B. P. Abbott *et al.*, Comprehensive all-sky search for periodic gravitational waves in the sixth science run LIGO data, Phys. Rev. D **94**, 042002 (2016).
[63] P. B. Covas and Alicia M. Sintes, New method to search for continuous gravitational waves from unknown neutron stars in binary systems, Phys. Rev. D **99**, 124019 (2019).
[64] Miquel Oliver, David Keitel, and Alicia M. Sintes, Adaptive transient Hough method for long-duration gravitational wave transients, Phys. Rev. D **99**, 104067 (2019).
[65] Rodrigo Tenorio, David Keitel, and Alicia M. Sintes, Time-frequency track distance for comparing continuous gravitational wave signals, Phys. Rev. D **103**, 064053 (2021).
[66] David Keitel, Rodrigo Tenorio, Gregory Ashton, and Reinhard Prix, PyFstat: A Python package for continuous gravitational-wave data analysis, J. Open Source Software **6**, 3000 (2021).
[67] Rodrigo Tenorio, David Keitel, and Alicia M. Sintes, Application of a hierarchical MCMC follow-up to Advanced LIGO continuous gravitational-wave candidates, Phys. Rev. D **104**, 084012 (2021).
[68] Sylvia J. Zhu, Masha Baryakhtar, Maria Alessandra Papa, Daichi Tsuna, Norita Kawanaka, and Heinz-Bernd Eggenstein, Characterizing the continuous gravitational-wave signal from boson clouds around Galactic isolated black holes, Phys. Rev. D **102**, 063020 (2020).
[69] G. Ashton and R. Prix, Hierarchical multistage MCMC follow-up of continuous gravitational wave candidates, Phys. Rev. D **97**, 103020 (2018).
[70] R. Abbott *et al.*, Search for continuous gravitational waves from 20 accreting millisecond x-ray pulsars in O3 LIGO data, Phys. Rev. D **105**, 022002 (2022).
[71] Prix, Reinhard, Coherent $\mathcal{F}$-statistic on semi-coherent candidate, https://dcc.ligo.org/LIGO-T1700236/public (2019).
[72] Andrzej Pisarski and Piotr Jaranowski, Banks of templates for all-sky narrow-band searches of gravitational waves from spinning neutron stars, Classical Quantum Gravity **32**, 145014 (2015).
[73] Benjamin J. Owen, Lee Lindblom, Curt Cutler, Bernard F. Schutz, Alberto Vecchio, and Nils Andersson, Gravitational waves from hot young rapidly rotating neutron stars, Phys. Rev. D **58**, 084020 (1998).
[74] Mark G. Alford and Kai Schwenzer, Gravitational wave emission and spin-down of young pulsars, Astrophys. J. **781**, 26 (2014).
[75] A. Patruno, B. Haskell, and N. Andersson, The spin distribution of fast-spinning neutron stars in low-mass x-ray binaries: Evidence for two subpopulations, Astrophys. J. **850**, 106 (2017).
[76] P. C. C. Freire, A. Ridolfi, M. Kramer, C. Jordan, R. N. Manchester, P. Torne, J. Sarkissian, C. O. Heinke, N. D'Amico, F. Camilo, D. R. Lorimer, and A. G. Lyne, Long-term observations of the pulsars in 47 Tucanae—II. Proper motions, accelerations and jerks, Mon. Not. R. Astron. Soc. **471**, 857 (2017).
[77] Guido Van Rossum and Fred L. Drake, *Python 3 Reference Manual* (CreateSpace, Scotts Valley, CA, 2009).
[78] Pauli Virtanen *et al.*, SciPy 1.0: Fundamental algorithms for scientific computing in Python, Nat. Methods **17**, 261 (2020).
[79] Eric O. Lebigot, Uncertainties: A python package for calculations with uncertainties (v3.1.5), http://pythonhosted.org/uncertainties (2020).
[80] Andrew J. Viterbi, Error bounds for convolutional codes and an asymptotically optimum decoding algorithm, IEEE Trans. Inf. Theory **13**, 260 (1967).
[81] Joe Bayley, Chris Messenger, and Graham Woan, Robust machine learning algorithm to search for continuous gravitational waves, Phys. Rev. D **102**, 083024 (2020).
[82] Joe Bayley, Non-parametric and machine learning techniques for continuous gravitational wave searches, Ph.D. thesis, University of Glasgow, 2020.
[83] Hunter Gabbard, Chris Messenger, Ik Siong Heng, Francesco Tonolini, and Roderick Murray-Smith, Bayesian parameter estimation using conditional variational autoencoders for gravitational-wave astronomy, Nat. Phys. **18**, 112 (2022).
[84] Joe Bayley, Chris Messenger, and Graham Woan (to be published).
[85] C. Palomba, Simulation of a population of isolated neutron stars evolving through the emission of gravitational waves, Mon. Not. R. Astron. Soc. **359**, 1150 (2005).
[86] Berit Behnke, Maria Alessandra Papa, and Reinhard Prix, Postprocessing methods used in the search for continuous gravitational-wave signals from the Galactic Center, Phys. Rev. D **91**, 064007 (2015).
[87] Christoph Dreissigacker, Reinhard Prix, and Karl Wette, Fast and accurate sensitivity estimation for continuous-gravitational-wave searches, Phys. Rev. D **98**, 084058 (2018).
[88] F. Pedregosa, G. Varoquaux, A. Gramfort, V. Michel, B. Thirion, O. Grisel, M. Blondel, P. Prettenhofer, R. Weiss, V. Dubourg, J. Vanderplas, A. Passos, D. Cournapeau, M. Brucher, M. Perrot, and E. Duchesnay, Scikit-learn: Machine learning in Python, J. Mach. Learn. Res. **12**, 2825 (2011), https://www.jmlr.org/papers/volume12/pedregosa11a/pedregosa11a.pdf.

[89] Vladimir Dergachev and Maria Alessandra Papa, The search for continuous gravitational waves from small-ellipticity sources at low frequencies, Phys. Rev. D **104**, 043003 (2021).
[90] R. Abbott *et al.*, All-sky, all-frequency directional search for persistent gravitational-waves from Advanced LIGO's and Advanced Virgo's first three observing runs, Phys. Rev. D **105**, 122001 (2022).
[91] Greg Ushomirsky, Curt Cutler, and Lars Bildsten, Deformations of accreting neutron star crusts and gravitational wave emission, Mon. Not. R. Astron. Soc. **319**, 902 (2000).
[92] B. Haskell, D. I. Jones, and N. Andersson, Mountains on neutron stars: Accreted versus non-accreted crusts, Mon. Not. R. Astron. Soc. **373**, 1423 (2006).
[93] Nathan K. Johnson-McDaniel and Benjamin J. Owen, Maximum elastic deformations of relativistic stars, Phys. Rev. D **88**, 044004 (2013).
[94] Fabian Gittins and Nils Andersson, Modelling neutron star mountains in relativity, Mon. Not. R. Astron. Soc. **507**, 116 (2021).
[95] F. Gittins, N. Andersson, and D. I. Jones, Modelling neutron star mountains, Mon. Not. R. Astron. Soc. **500**, 5570 (2020).
[96] A. G. Suvorov, A. Mastrano, and U. Geppert, Gravitational radiation from neutron stars deformed by crustal Hall drift, Mon. Not. R. Astron. Soc. **459**, 3407 (2016).
[97] B. P. Abbott *et al.*, Searches for gravitational waves from known pulsars at two harmonics in 2015-2017 LIGO data, Astrophys. J. **879**, 10 (2019).
[98] Christian T. Byrnes, Mark Hindmarsh, Sam Young, and Michael R. S. Hawkins, Primordial black holes with an accurate QCD equation of state, J. Cosmol. Astropart. Phys. 08 (2018) 041.
[99] Martti Raidal, Christian Spethmann, Ville Vaskonen, and Hardi Veermäe, Formation and evolution of primordial black hole binaries in the early universe, J. Cosmol. Astropart. Phys. 02 (2019) 018.
[100] Gert Hütsi, Martti Raidal, Ville Vaskonen, and Hardi Veermäe, Two populations of LIGO-Virgo black holes, J. Cosmol. Astropart. Phys. 03 (2021) 068.

R. Abbott,[1] H. Abe,[2] F. Acernese,[3,4] K. Ackley,[5] N. Adhikari,[6] R. X. Adhikari,[1] V. K. Adkins,[7] V. B. Adya,[8] C. Affeldt,[9,10] D. Agarwal,[11] M. Agathos,[12,13] K. Agatsuma,[14] N. Aggarwal,[15] O. D. Aguiar,[16] L. Aiello,[17] A. Ain,[18] P. Ajith,[19] T. Akutsu,[20,21] S. Albanesi,[22,23] R. A. Alfaidi,[24] A. Allocca,[25,4] P. A. Altin,[8] A. Amato,[26] C. Anand,[5] S. Anand,[1] A. Ananyeva,[1] S. B. Anderson,[1] W. G. Anderson,[6] M. Ando,[27,28] T. Andrade,[29] N. Andres,[30] M. Andrés-Carcasona,[31] T. Andrić,[32] S. V. Angelova,[33] S. Ansoldi,[34,35] J. M. Antelis,[36] S. Antier,[37,38] T. Apostolatos,[39] E. Z. Appavuravther,[40,41] S. Appert,[1] S. K. Apple,[42] K. Arai,[1] A. Araya,[43] M. C. Araya,[1] J. S. Areeda,[44] M. Arène,[45] N. Aritomi,[20] N. Arnaud,[46,47] M. Arogeti,[48] S. M. Aronson,[7] H. Asada,[49] Y. Asali,[50] G. Ashton,[51] Y. Aso,[52,53] M. Assiduo,[54,55] S. Assis de Souza Melo,[47] S. M. Aston,[56] P. Astone,[57] F. Aubin,[55] K. AultONeal,[36] C. Austin,[7] S. Babak,[45] F. Badaracco,[58] M. K. M. Bader,[59] C. Badger,[60] S. Bae,[61] Y. Bae,[62] A. M. Baer,[63] S. Bagnasco,[23] Y. Bai,[1] J. Baird,[45] R. Bajpai,[64] T. Baka,[65] M. Ball,[66] G. Ballardin,[47] S. W. Ballmer,[67] A. Balsamo,[63] G. Baltus,[68] S. Banagiri,[15] B. Banerjee,[32] D. Bankar,[11] J. C. Barayoga,[1] C. Barbieri,[69,70,71] B. C. Barish,[1] D. Barker,[72] P. Barneo,[29] F. Barone,[73,4] B. Barr,[24] L. Barsotti,[74] M. Barsuglia,[45] D. Barta,[75] J. Bartlett,[72] M. A. Barton,[24] I. Bartos,[76] S. Basak,[19] R. Bassiri,[77] A. Basti,[78,18] M. Bawaj,[40,79] J. C. Bayley,[24] M. Bazzan,[80,81] B. R. Becher,[82] B. Bécsy,[83] V. M. Bedakihale,[84] F. Beirnaert,[85] M. Bejger,[86] I. Belahcene,[46] V. Benedetto,[87] D. Beniwal,[88] M. G. Benjamin,[89] T. F. Bennett,[90] J. D. Bentley,[14] M. BenYaala,[33] S. Bera,[11] M. Berbel,[91] F. Bergamin,[9,10] B. K. Berger,[77] S. Bernuzzi,[13] D. Bersanetti,[92] A. Bertolini,[59] J. Betzwieser,[56] D. Beveridge,[93] R. Bhandare,[94] A. V. Bhandari,[11] U. Bhardwaj,[38,59] R. Bhatt,[1] D. Bhattacharjee,[95] S. Bhaumik,[76] A. Bianchi,[59,96] I. A. Bilenko,[97] G. Billingsley,[1] S. Bini,[98,99] R. Birney,[100] O. Birnholtz,[101] S. Biscans,[1,74] M. Bischi,[54,55] S. Biscoveanu,[74] A. Bisht,[9,10] B. Biswas,[11] M. Bitossi,[47,18] M.-A. Bizouard,[37] J. K. Blackburn,[1] C. D. Blair,[93] D. G. Blair,[93] R. M. Blair,[72] F. Bobba,[102,103] N. Bode,[9,10] M. Boër,[37] G. Bogaert,[37] M. Boldrini,[104,57] G. N. Bolingbroke,[88] L. D. Bonavena,[80] F. Bondu,[105] E. Bonilla,[77] R. Bonnand,[30] P. Booker,[9,10] B. A. Boom,[59] R. Bork,[1] V. Boschi,[18] N. Bose,[106] S. Bose,[11] V. Bossilkov,[93] V. Boudart,[68] Y. Bouffanais,[80,81] A. Bozzi,[47] C. Bradaschia,[18] P. R. Brady,[6] A. Bramley,[56] A. Branch,[56] M. Branchesi,[32,107] J. E. Brau,[66] M. Breschi,[13] T. Briant,[108] J. H. Briggs,[24] A. Brillet,[37] M. Brinkmann,[9,10] P. Brockill,[6] A. F. Brooks,[1] J. Brooks,[47] D. D. Brown,[88] S. Brunett,[1] G. Bruno,[58] R. Bruntz,[63] J. Bryant,[14] F. Bucci,[55] T. Bulik,[109] H. J. Bulten,[59] A. Buonanno,[110,111] K. Burtnyk,[72] R. Buscicchio,[14] D. Buskulic,[30] C. Buy,[112] R. L. Byer,[77] G. S. Cabourn Davies,[51] G. Cabras,[34,35] R. Cabrita,[58] L. Cadonati,[48] M. Caesar,[113] G. Cagnoli,[26] C. Cahillane,[72] J. Calderón Bustillo,[114] J. D. Callaghan,[24] T. A. Callister,[115,116] E. Calloni,[25,4] J. Cameron,[93] J. B. Camp,[117] M. Canepa,[118,92] S. Canevarolo,[65] M. Cannavacciuolo,[102] K. C. Cannon,[28] H. Cao,[88] Z. Cao,[119] E. Capocasa,[45,20] E. Capote,[67] G. Carapella,[102,103] F. Carbognani,[47] M. Carlassara,[9,10] J. B. Carlin,[120] M. F. Carney,[15] M. Carpinelli,[121,122,47] G. Carrillo,[66] G. Carullo,[78,18] T. L. Carver,[17] J. Casanueva Diaz,[47] C. Casentini,[123,124] G. Castaldi,[125] S. Caudill,[59,65] M. Cavaglià,[95] F. Cavalier,[46] R. Cavalieri,[47] G. Cella,[18] P. Cerdá-Durán,[126] E. Cesarini,[124] W. Chaibi,[37]

S. Chalathadka Subrahmanya,[127] E. Champion,[128] C.-H. Chan,[129] C. Chan,[28] C. L. Chan,[130] K. Chan,[130] M. Chan,[131] K. Chandra,[106] I. P. Chang,[129] P. Chanial,[47] S. Chao,[129] C. Chapman-Bird,[24] P. Charlton,[132] E. A. Chase,[15] E. Chassande-Mottin,[45] C. Chatterjee,[93] Debarati Chatterjee,[11] Deep Chatterjee,[6] M. Chaturvedi,[94] S. Chaty,[45] C. Chen,[133,134] D. Chen,[52] H. Y. Chen,[74] J. Chen,[129] K. Chen,[135] X. Chen,[93] Y.-B. Chen,[136] Y.-R. Chen,[137] Z. Chen,[17] H. Cheng,[76] C. K. Cheong,[130] H. Y. Cheung,[130] H. Y. Chia,[76] F. Chiadini,[138,103] C-Y. Chiang,[139] G. Chiarini,[81] R. Chierici,[140] A. Chincarini,[92] M. L. Chiofalo,[78,18] A. Chiummo,[47] R. K. Choudhary,[93] S. Choudhary,[11] N. Christensen,[37] Q. Chu,[93] Y-K. Chu,[139] S. S. Y. Chua,[8] K. W. Chung,[60] G. Ciani,[80,81] P. Ciecielag,[86] M. Cieślar,[86] M. Cifaldi,[123,124] A. A. Ciobanu,[88] R. Ciolfi,[141,81] F. Cipriano,[37] F. Clara,[72] J. A. Clark,[1,48] P. Clearwater,[142] S. Clesse,[143] F. Cleva,[37] E. Coccia,[32,107] E. Codazzo,[32] P.-F. Cohadon,[108] D. E. Cohen,[46] M. Colleoni,[144] C. G. Collette,[145] A. Colombo,[69,70] M. Colpi,[69,70] C. M. Compton,[72] M. Constancio Jr.,[16] L. Conti,[81] S. J. Cooper,[14] P. Corban,[56] T. R. Corbitt,[7] I. Cordero-Carrión,[146] S. Corezzi,[79,40] K. R. Corley,[50] N. J. Cornish,[83] D. Corre,[46] A. Corsi,[147] S. Cortese,[47] C. A. Costa,[16] R. Cotesta,[111] R. Cottingham,[56] M. W. Coughlin,[148] J.-P. Coulon,[37] S. T. Countryman,[50] B. Cousins,[149] P. Couvares,[1] D. M. Coward,[93] M. J. Cowart,[56] D. C. Coyne,[1] R. Coyne,[150] J. D. E. Creighton,[6] T. D. Creighton,[89] A. W. Criswell,[148] M. Croquette,[108] S. G. Crowder,[151] J. R. Cudell,[68] T. J. Cullen,[7] A. Cumming,[24] R. Cummings,[24] L. Cunningham,[24] E. Cuoco,[47,152,18] M. Curyło,[109] P. Dabadie,[26] T. Dal Canton,[46] S. Dall'Osso,[32] G. Dálya,[85,153] A. Dana,[77] B. D'Angelo,[118,92] S. Danilishin,[154,59] S. D'Antonio,[124] K. Danzmann,[9,10] C. Darsow-Fromm,[127] A. Dasgupta,[84] L. E. H. Datrier,[24] Sayak Datta,[11] Sayantani Datta,[155] V. Dattilo,[47] I. Dave,[94] M. Davier,[46] D. Davis,[1] M. C. Davis,[113] E. J. Daw,[156] R. Dean,[113] D. DeBra,[77] M. Deenadayalan,[11] J. Degallaix,[157] M. De Laurentis,[25,4] S. Deléglise,[108] V. Del Favero,[128] F. De Lillo,[58] N. De Lillo,[24] D. Dell'Aquila,[121] W. Del Pozzo,[78,18] L. M. DeMarchi,[15] F. De Matteis,[123,124] V. D'Emilio,[17] N. Demos,[74] T. Dent,[114] A. Depasse,[58] R. De Pietri,[158,159] R. De Rosa,[25,4] C. De Rossi,[47] R. DeSalvo,[125,160] R. De Simone,[138] S. Dhurandhar,[11] M. C. Díaz,[89] M. Di Cesare,[104] N. A. Didio,[67] T. Dietrich,[111] L. Di Fiore,[4] C. Di Fronzo,[14] C. Di Giorgio,[102,103] F. Di Giovanni,[126] M. Di Giovanni,[32] T. Di Girolamo,[25,4] A. Di Lieto,[78,18] A. Di Michele,[79] B. Ding,[145] S. Di Pace,[104,57] I. Di Palma,[104,57] F. Di Renzo,[78,18] A. K. Divakarla,[76] A. Dmitriev,[14] Z. Doctor,[15] L. Donahue,[161] L. D'Onofrio,[25,4] F. Donovan,[74] K. L. Dooley,[17] S. Doravari,[11] O. Dorosh,[162] M. Drago,[104,57] J. C. Driggers,[72] Y. Drori,[1] J.-G. Ducoin,[46] P. Dupej,[24] U. Dupletsa,[32] O. Durante,[102,103] D. D'Urso,[121,122] P.-A. Duverne,[46] S. E. Dwyer,[72] C. Eassa,[72] P. J. Easter,[5] M. Ebersold,[163] T. Eckhardt,[127] G. Eddolls,[24] B. Edelman,[66] T. B. Edo,[1] O. Edy,[51] A. Effler,[56] S. Eguchi,[131] J. Eichholz,[8] S. S. Eikenberry,[76] M. Eisenmann,[30,20] R. A. Eisenstein,[74] A. Ejlli,[17] E. Engelby,[44] Y. Enomoto,[27] L. Errico,[25,4] R. C. Essick,[164] H. Estellés,[144] D. Estevez,[165] Z. Etienne,[166] T. Etzel,[1] M. Evans,[74] T. M. Evans,[56] T. Evstafyeva,[12] B. E. Ewing,[149] F. Fabrizi,[54,55] F. Faedi,[55] V. Fafone,[123,124,32] H. Fair,[67] S. Fairhurst,[17] P. C. Fan,[161] A. M. Farah,[167] S. Farinon,[92] B. Farr,[66] W. M. Farr,[115,116] E. J. Fauchon-Jones,[17] G. Favaro,[80] M. Favata,[168] M. Fays,[68] M. Fazio,[169] J. Feicht,[1] M. M. Fejer,[77] E. Fenyvesi,[75,170] D. L. Ferguson,[171] A. Fernandez-Galiana,[74] I. Ferrante,[78,18] T. A. Ferreira,[16] F. Fidecaro,[78,18] P. Figura,[109] A. Fiori,[18,78] I. Fiori,[47] M. Fishbach,[15] R. P. Fisher,[63] R. Fittipaldi,[172,103] V. Fiumara,[173,103] R. Flaminio,[30,20] E. Floden,[148] H. K. Fong,[28] J. A. Font,[126,174] B. Fornal,[160] P. W. F. Forsyth,[8] A. Franke,[127] S. Frasca,[104,57] F. Frasconi,[18] J. P. Freed,[36] Z. Frei,[153] A. Freise,[59,96] O. Freitas,[175] R. Frey,[66] P. Fritschel,[74] V. V. Frolov,[56] G. G. Fronzé,[23] Y. Fujii,[176] Y. Fujikawa,[177] Y. Fujimoto,[178] P. Fulda,[76] M. Fyffe,[56] H. A. Gabbard,[24] B. U. Gadre,[111] J. R. Gair,[111] J. Gais,[130] S. Galaudage,[5] R. Gamba,[13] D. Ganapathy,[74] A. Ganguly,[11] D. Gao,[179] S. G. Gaonkar,[11] B. Garaventa,[92,118] C. García Núñez,[100] C. García-Quirós,[144] F. Garufi,[25,4] B. Gateley,[72] V. Gayathri,[76] G.-G. Ge,[179] G. Gemme,[92] A. Gennai,[18] J. George,[94] O. Gerberding,[127] L. Gergely,[180] P. Gewecke,[127] S. Ghonge,[48] Abhirup Ghosh,[111] Archisman Ghosh,[85] Shaon Ghosh,[168] Shrobana Ghosh,[17] Tathagata Ghosh,[11] B. Giacomazzo,[69,70,71] L. Giacoppo,[104,57] J. A. Giaime,[7,56] K. D. Giardina,[56] D. R. Gibson,[100] C. Gier,[33] M. Giesler,[181] P. Giri,[18,78] F. Gissi,[87] S. Gkaitatzis,[18,78] J. Glanzer,[7] A. E. Gleckl,[44] P. Godwin,[149] E. Goetz,[182] R. Goetz,[76] N. Gohlke,[9,10] J. Golomb,[1] B. Goncharov,[32] G. González,[7] M. Gosselin,[47] R. Gouaty,[30] D. W. Gould,[8] S. Goyal,[19] B. Grace,[8] A. Grado,[183,4] V. Graham,[24] M. Granata,[157] V. Granata,[102] A. Grant,[24] S. Gras,[74] P. Grassia,[1] C. Gray,[72] R. Gray,[24] G. Greco,[40] A. C. Green,[76] R. Green,[17] A. M. Gretarsson,[36] E. M. Gretarsson,[36] D. Griffith,[1] W. L. Griffiths,[17] H. L. Griggs,[48] G. Grignani,[79,40] A. Grimaldi,[98,99] E. Grimes,[36] S. J. Grimm,[32,107] H. Grote,[17] S. Grunewald,[111] P. Gruning,[46] A. S. Gruson,[44] D. Guerra,[126] G. M. Guidi,[54,55] A. R. Guimaraes,[7] G. Guixé,[29] H. K. Gulati,[84] A. M. Gunny,[74] H.-K. Guo,[160] Y. Guo,[59] Anchal Gupta,[1] Anuradha Gupta,[184] I. M. Gupta,[149] P. Gupta,[59,65] S. K. Gupta,[106] R. Gustafson,[185] F. Guzman,[186] S. Ha,[187] I. P. W. Hadiputrawan,[135] L. Haegel,[45] S. Haino,[139] O. Halim,[35] E. D. Hall,[74] E. Z. Hamilton,[163] G. Hammond,[24] W.-B. Han,[188] M. Haney,[163] J. Hanks,[72] C. Hanna,[149] M. D. Hannam,[17] O. Hannuksela,[65,59] H. Hansen,[72] T. J. Hansen,[36] J. Hanson,[56] T. Harder,[37] K. Haris,[59,65]

J. Harms,[32,107] G. M. Harry,[42] I. W. Harry,[51] D. Hartwig,[127] K. Hasegawa,[189] B. Haskell,[86] C.-J. Haster,[74] J. S. Hathaway,[128] K. Hattori,[190] K. Haughian,[24] H. Hayakawa,[191] K. Hayama,[131] F. J. Hayes,[24] J. Healy,[128] A. Heidmann,[108] A. Heidt,[9,10] M. C. Heintze,[56] J. Heinze,[9,10] J. Heinzel,[74] H. Heitmann,[37] F. Hellman,[192] P. Hello,[46] A. F. Helmling-Cornell,[66] G. Hemming,[47] M. Hendry,[24] I. S. Heng,[24] E. Hennes,[59] J. Hennig,[193] M. H. Hennig,[193] C. Henshaw,[48] A. G. Hernandez,[90] F. Hernandez Vivanco,[5] M. Heurs,[9,10] A. L. Hewitt,[194] S. Higginbotham,[17] S. Hild,[154,59] P. Hill,[33] Y. Himemoto,[195] A. S. Hines,[186] N. Hirata,[20] C. Hirose,[177] T-C. Ho,[135] S. Hochheim,[9,10] D. Hofman,[157] J. N. Hohmann,[127] D. G. Holcomb,[113] N. A. Holland,[8] I. J. Hollows,[156] Z. J. Holmes,[88] K. Holt,[56] D. E. Holz,[167] Q. Hong,[129] J. Hough,[24] S. Hourihane,[1] E. J. Howell,[93] C. G. Hoy,[17] D. Hoyland,[14] A. Hreibi,[9,10] B-H. Hsieh,[189] H-F. Hsieh,[196] C. Hsiung,[133] Y. Hsu,[129] H-Y. Huang,[139] P. Huang,[179] Y-C. Huang,[137] Y.-J. Huang,[139] Yiting Huang,[151] Yiwen Huang,[74] M. T. Hübner,[5] A. D. Huddart,[197] B. Hughey,[36] D. C. Y. Hui,[198] V. Hui,[30] S. Husa,[144] S. H. Huttner,[24] R. Huxford,[149] T. Huynh-Dinh,[56] S. Ide,[199] B. Idzkowski,[109] A. Iess,[123,124] K. Inayoshi,[200] Y. Inoue,[135] P. Iosif,[201] M. Isi,[74] K. Isleif,[127] K. Ito,[202] Y. Itoh,[178,203] B. R. Iyer,[19] V. JaberianHamedan,[93] T. Jacqmin,[108] P.-E. Jacquet,[108] S. J. Jadhav,[204] S. P. Jadhav,[11] T. Jain,[12] A. L. James,[17] A. Z. Jan,[171] K. Jani,[205] J. Janquart,[65,59] K. Janssens,[206,37] N. N. Janthalur,[204] P. Jaranowski,[207] D. Jariwala,[76] R. Jaume,[144] A. C. Jenkins,[60] K. Jenner,[88] C. Jeon,[208] W. Jia,[74] J. Jiang,[76] H.-B. Jin,[209,210] G. R. Johns,[63] R. Johnston,[24] A. W. Jones,[93] D. I. Jones,[211] P. Jones,[14] R. Jones,[24] P. Joshi,[149] L. Ju,[93] A. Jue,[160] P. Jung,[62] K. Jung,[187] J. Junker,[9,10] V. Juste,[165] K. Kaihotsu,[202] T. Kajita,[212] M. Kakizaki,[190] C. V. Kalaghatgi,[17,65,59,213] V. Kalogera,[15] B. Kamai,[1] M. Kamiizumi,[191] N. Kanda,[178,203] S. Kandhasamy,[11] G. Kang,[214] J. B. Kanner,[1] Y. Kao,[129] S. J. Kapadia,[19] D. P. Kapasi,[8] C. Karathanasis,[31] S. Karki,[95] R. Kashyap,[149] M. Kasprzack,[1] W. Kastaun,[9,10] T. Kato,[189] S. Katsanevas,[47] E. Katsavounidis,[74] W. Katzman,[56] T. Kaur,[93] K. Kawabe,[72] K. Kawaguchi,[189] F. Kéfélian,[37] D. Keitel,[144] J. S. Key,[215] S. Khadka,[77] F. Y. Khalili,[97] S. Khan,[17] T. Khanam,[147] E. A. Khazanov,[216] N. Khetan,[32,107] M. Khursheed,[94] N. Kijbunchoo,[8] A. Kim,[15] C. Kim,[208] J. C. Kim,[217] J. Kim,[218] K. Kim,[208] W. S. Kim,[62] Y.-M. Kim,[187] C. Kimball,[15] N. Kimura,[191] M. Kinley-Hanlon,[24] R. Kirchhoff,[9,10] J. S. Kissel,[72] S. Klimenko,[76] T. Klinger,[12] A. M. Knee,[182] T. D. Knowles,[166] N. Knust,[9,10] E. Knyazev,[74] Y. Kobayashi,[178] P. Koch,[9,10] G. Koekoek,[59,154] K. Kohri,[219] K. Kokeyama,[220] S. Koley,[32] P. Kolitsidou,[17] M. Kolstein,[31] K. Komori,[74] V. Kondrashov,[1] A. K. H. Kong,[196] A. Kontos,[82] N. Koper,[9,10] M. Korobko,[127] M. Kovalam,[93] N. Koyama,[177] D. B. Kozak,[1] C. Kozakai,[52] V. Kringel,[9,10] N. V. Krishnendu,[9,10] A. Królak,[221,162] G. Kuehn,[9,10] F. Kuei,[129] P. Kuijer,[59] S. Kulkarni,[184] A. Kumar,[204] Prayush Kumar,[19] Rahul Kumar,[72] Rakesh Kumar,[84] J. Kume,[28] K. Kuns,[74] Y. Kuromiya,[202] S. Kuroyanagi,[222,223] K. Kwak,[187] G. Lacaille,[24] P. Lagabbe,[30] D. Laghi,[112] E. Lalande,[224] M. Lalleman,[206] T. L. Lam,[130] A. Lamberts,[37,225] M. Landry,[72] B. B. Lane,[74] R. N. Lang,[74] J. Lange,[171] B. Lantz,[77] I. La Rosa,[30] A. Lartaux-Vollard,[46] P. D. Lasky,[5] M. Laxen,[56] A. Lazzarini,[1] C. Lazzaro,[80,81] P. Leaci,[104,57] S. Leavey,[9,10] S. LeBohec,[160] Y. K. Lecoeuche,[182] E. Lee,[189] H. M. Lee,[226] H. W. Lee,[217] K. Lee,[227] R. Lee,[137] I. N. Legred,[1] J. Lehmann,[9,10] A. Lemaître,[228] M. Lenti,[55,229] M. Leonardi,[20] E. Leonova,[38] N. Leroy,[46] N. Letendre,[30] C. Levesque,[224] Y. Levin,[5] J. N. Leviton,[185] K. Leyde,[45] A. K. Y. Li,[1] B. Li,[129] J. Li,[15] K. L. Li,[230] P. Li,[231] T. G. F. Li,[130] X. Li,[136] C-Y. Lin,[232] E. T. Lin,[196] F-K. Lin,[139] F-L. Lin,[233] H. L. Lin,[135] L. C.-C. Lin,[230] F. Linde,[213,59] S. D. Linker,[125,90] J. N. Linley,[24] T. B. Littenberg,[234] G. C. Liu,[133] J. Liu,[93] K. Liu,[129] X. Liu,[6] F. Llamas,[89] R. K. L. Lo,[1] T. Lo,[129] L. T. London,[38,74] A. Longo,[235] D. Lopez,[163] M. Lopez Portilla,[65] M. Lorenzini,[123,124] V. Loriette,[236] M. Lormand,[56] G. Losurdo,[18] T. P. Lott,[48] J. D. Lough,[9,10] C. O. Lousto,[128] G. Lovelace,[44] J. F. Lucaccioni,[237] H. Lück,[9,10] D. Lumaca,[123,124] A. P. Lundgren,[51] L.-W. Luo,[139] J. E. Lynam,[63] M. Ma'arif,[135] R. Macas,[51] J. B. Machtinger,[15] M. MacInnis,[74] D. M. Macleod,[17] I. A. O. MacMillan,[1] A. Macquet,[37] I. Magaña Hernandez,[6] C. Magazzù,[18] R. M. Magee,[1] R. Maggiore,[14] M. Magnozzi,[92,118] S. Mahesh,[166] E. Majorana,[104,57] I. Maksimovic,[236] S. Maliakal,[1] A. Malik,[94] N. Man,[37] V. Mandic,[148] V. Mangano,[104,57] G. L. Mansell,[72,74] M. Manske,[6] M. Mantovani,[47] M. Mapelli,[80,81] F. Marchesoni,[41,40,238] D. Marín Pina,[29] F. Marion,[30] Z. Mark,[136] S. Márka,[50] Z. Márka,[50] C. Markakis,[12] A. S. Markosyan,[77] A. Markowitz,[1] E. Maros,[1] A. Marquina,[146] S. Marsat,[45] F. Martelli,[54,55] I. W. Martin,[24] R. M. Martin,[168] M. Martinez,[31] V. A. Martinez,[76] V. Martinez,[26] K. Martinovic,[60] D. V. Martynov,[14] E. J. Marx,[74] H. Masalehdan,[127] K. Mason,[74] E. Massera,[156] A. Masserot,[30] M. Masso-Reid,[24] S. Mastrogiovanni,[45] A. Matas,[111] M. Mateu-Lucena,[144] F. Matichard,[1,74] M. Matiushechkina,[9,10] N. Mavalvala,[74] J. J. McCann,[93] R. McCarthy,[72] D. E. McClelland,[8] P. K. McClincy,[149] S. McCormick,[56] L. McCuller,[74] G. I. McGhee,[24] S. C. McGuire,[56] C. McIsaac,[51] J. McIver,[182] T. McRae,[8] S. T. McWilliams,[166] D. Meacher,[6] M. Mehmet,[9,10] A. K. Mehta,[111] Q. Meijer,[65] A. Melatos,[120] D. A. Melchor,[44] G. Mendell,[72] A. Menendez-Vazquez,[31] C. S. Menoni,[169] R. A. Mercer,[6] L. Mereni,[157] K. Merfeld,[66] E. L. Merilh,[56] J. D. Merritt,[66] M. Merzougui,[37] S. Meshkov,[1,†] C. Messenger,[24] C. Messick,[74] P. M. Meyers,[120] F. Meylahn,[9,10] A. Mhaske,[11] A. Miani,[98,99] H. Miao,[14] I. Michaloliakos,[76] C. Michel,[157] Y. Michimura,[27] H. Middleton,[120]

D. P. Mihaylov,[111] L. Milano,[25,‡] A. L. Miller,[58] A. Miller,[90] B. Miller,[38,59] M. Millhouse,[120] J. C. Mills,[17] E. Milotti,[239,35] Y. Minenkov,[124] N. Mio,[240] Ll. M. Mir,[31] M. Miravet-Tenés,[126] A. Mishkin,[76] C. Mishra,[241] T. Mishra,[76] T. Mistry,[156] S. Mitra,[11] V. P. Mitrofanov,[97] G. Mitselmakher,[76] R. Mittleman,[74] O. Miyakawa,[191] K. Miyo,[191] S. Miyoki,[191] Geoffrey Mo,[74] L. M. Modafferi,[144] E. Moguel,[237] K. Mogushi,[95] S. R. P. Mohapatra,[74] S. R. Mohite,[6] I. Molina,[44] M. Molina-Ruiz,[192] M. Mondin,[90] M. Montani,[54,55] C. J. Moore,[14] J. Moragues,[144] D. Moraru,[72] F. Morawski,[86] A. More,[11] C. Moreno,[36] G. Moreno,[72] Y. Mori,[202] S. Morisaki,[6] N. Morisue,[178] Y. Moriwaki,[190] B. Mours,[165] C. M. Mow-Lowry,[59,96] S. Mozzon,[51] F. Muciaccia,[104,57] Arunava Mukherjee,[242] D. Mukherjee,[149] Soma Mukherjee,[89] Subroto Mukherjee,[84] Suvodip Mukherjee,[164,38] N. Mukund,[9,10] A. Mullavey,[56] J. Munch,[88] E. A. Muñiz,[67] P. G. Murray,[24] R. Musenich,[92,118] S. Muusse,[88] S. L. Nadji,[9,10] K. Nagano,[243] A. Nagar,[23,244] K. Nakamura,[20] H. Nakano,[245] M. Nakano,[189] Y. Nakayama,[202] V. Napolano,[47] I. Nardecchia,[123,124] T. Narikawa,[189] H. Narola,[65] L. Naticchioni,[57] B. Nayak,[90] R. K. Nayak,[246] B. F. Neil,[93] J. Neilson,[87,103] A. Nelson,[186] T. J. N. Nelson,[56] M. Nery,[9,10] P. Neubauer,[237] A. Neunzert,[215] K. Y. Ng,[74] S. W. S. Ng,[88] C. Nguyen,[45] P. Nguyen,[66] T. Nguyen,[74] L. Nguyen Quynh,[247] J. Ni,[148] W.-T. Ni,[209,179,137] S. A. Nichols,[7] T. Nishimoto,[189] A. Nishizawa,[28] S. Nissanke,[38,59] E. Nitoglia,[140] F. Nocera,[47] M. Norman,[17] C. North,[17] S. Nozaki,[190] G. Nurbek,[89] L. K. Nuttall,[51] Y. Obayashi,[189] J. Oberling,[72] B. D. O'Brien,[76] J. O'Dell,[197] E. Oelker,[24] W. Ogaki,[189] G. Oganesyan,[32,107] J. J. Oh,[62] K. Oh,[198] S. H. Oh,[62] M. Ohashi,[191] T. Ohashi,[178] M. Ohkawa,[177] F. Ohme,[9,10] H. Ohta,[28] M. A. Okada,[16] Y. Okutani,[199] C. Olivetto,[47] K. Oohara,[189,248] R. Oram,[56] B. O'Reilly,[56] R. G. Ormiston,[148] N. D. Ormsby,[63] R. O'Shaughnessy,[128] E. O'Shea,[181] S. Oshino,[191] S. Ossokine,[111] C. Osthelder,[1] S. Otabe,[2] D. J. Ottaway,[88] H. Overmier,[56] A. E. Pace,[149] G. Pagano,[78,18] R. Pagano,[7] M. A. Page,[93] G. Pagliaroli,[32,107] A. Pai,[106] S. A. Pai,[94] S. Pal,[246] J. R. Palamos,[66] O. Palashov,[216] C. Palomba,[57] H. Pan,[129] K.-C. Pan,[137,196] P. K. Panda,[204] P. T. H. Pang,[59,65] C. Pankow,[15] F. Pannarale,[104,57] B. C. Pant,[94] F. H. Panther,[93] F. Paoletti,[18] A. Paoli,[47] A. Paolone,[57,249] G. Pappas,[201] A. Parisi,[133] H. Park,[6] J. Park,[250] W. Parker,[56] D. Pascucci,[59,85] A. Pasqualetti,[47] R. Passaquieti,[78,18] D. Passuello,[18] M. Patel,[63] M. Pathak,[88] B. Patricelli,[47,18] A. S. Patron,[7] S. Paul,[66] E. Payne,[5] M. Pedraza,[1] R. Pedurand,[103] M. Pegoraro,[81] A. Pele,[56] F. E. Peña Arellano,[191] S. Penano,[77] S. Penn,[251] A. Perego,[98,99] A. Pereira,[26] T. Pereira,[252] C. J. Perez,[72] C. Périgois,[30] C. C. Perkins,[76] A. Perreca,[98,99] S. Perriès,[140] D. Pesios,[201] J. Petermann,[127] D. Petterson,[1] H. P. Pfeiffer,[111] H. Pham,[56] K. A. Pham,[148] K. S. Phukon,[59,213] H. Phurailatpam,[130] O. J. Piccinni,[57] M. Pichot,[37] M. Piendibene,[78,18] F. Piergiovanni,[54,55] L. Pierini,[104,57] V. Pierro,[87,103] G. Pillant,[47] M. Pillas,[46] F. Pilo,[18] L. Pinard,[157] C. Pineda-Bosque,[90] I. M. Pinto,[87,103,253] M. Pinto,[47] B. J. Piotrzkowski,[6] K. Piotrzkowski,[58] M. Pirello,[72] A. Pisarski,[207] M. D. Pitkin,[194] A. Placidi,[40,79] E. Placidi,[104,57] M. L. Planas,[144] W. Plastino,[254,235] C. Pluchar,[255] R. Poggiani,[78,18] E. Polini,[30] D. Y. T. Pong,[130] S. Ponrathnam,[11] E. K. Porter,[45] R. Poulton,[47] A. Poverman,[82] J. Powell,[142] M. Pracchia,[30] T. Pradier,[165] A. K. Prajapati,[84] K. Prasai,[77] R. Prasanna,[204] G. Pratten,[14] M. Principe,[87,253,103] G. A. Prodi,[256,99] L. Prokhorov,[14] P. Prosposito,[123,124] L. Prudenzi,[111] A. Puecher,[59,65] M. Punturo,[40] F. Puosi,[18,78] P. Puppo,[57] M. Pürrer,[111] H. Qi,[17] N. Quartey,[63] V. Quetschke,[89] P. J. Quinonez,[36] R. Quitzow-James,[95] F. J. Raab,[72] G. Raaijmakers,[38,59] H. Radkins,[72] N. Radulesco,[37] P. Raffai,[153] S. X. Rail,[224] S. Raja,[94] C. Rajan,[94] K. E. Ramirez,[56] T. D. Ramirez,[44] A. Ramos-Buades,[111] J. Rana,[149] P. Rapagnani,[104,57] A. Ray,[6] V. Raymond,[17] N. Raza,[182] M. Razzano,[78,18] J. Read,[44] L. A. Rees,[42] T. Regimbau,[30] L. Rei,[92] S. Reid,[33] S. W. Reid,[63] D. H. Reitze,[1,76] P. Relton,[17] A. Renzini,[1] P. Rettegno,[22,23] B. Revenu,[45] A. Reza,[59] M. Rezac,[44] F. Ricci,[104,57] D. Richards,[197] J. W. Richardson,[257] L. Richardson,[186] G. Riemenschneider,[22,23] K. Riles,[185] S. Rinaldi,[78,18] K. Rink,[182] N. A. Robertson,[1] R. Robie,[1] F. Robinet,[46] A. Rocchi,[124] S. Rodriguez,[44] L. Rolland,[30] J. G. Rollins,[1] M. Romanelli,[105] R. Romano,[3,4] C. L. Romel,[72] A. Romero,[31] I. M. Romero-Shaw,[5] J. H. Romie,[56] S. Ronchini,[32,107] L. Rosa,[4,25] C. A. Rose,[6] D. Rosińska,[109] M. P. Ross,[258] S. Rowan,[24] S. J. Rowlinson,[14] S. Roy,[65] Santosh Roy,[11] Soumen Roy,[259] D. Rozza,[121,122] P. Ruggi,[47] K. Ruiz-Rocha,[205] K. Ryan,[72] S. Sachdev,[149] T. Sadecki,[72] J. Sadiq,[114] S. Saha,[196] Y. Saito,[191] K. Sakai,[260] M. Sakellariadou,[60] S. Sakon,[149] O. S. Salafia,[71,70,69] F. Salces-Carcoba,[1] L. Salconi,[47] M. Saleem,[148] F. Salemi,[98,99] A. Samajdar,[70] E. J. Sanchez,[1] J. H. Sanchez,[44] L. E. Sanchez,[1] N. Sanchis-Gual,[261] J. R. Sanders,[262] A. Sanuy,[29] T. R. Saravanan,[11] N. Sarin,[5] B. Sassolas,[157] H. Satari,[93] O. Sauter,[76] R. L. Savage,[72] V. Savant,[11] T. Sawada,[178] H. L. Sawant,[11] S. Sayah,[157] D. Schaetzl,[1] M. Scheel,[136] J. Scheuer,[15] M. G. Schiworski,[88] P. Schmidt,[14] S. Schmidt,[65] R. Schnabel,[127] M. Schneewind,[9,10] R. M. S. Schofield,[66] A. Schönbeck,[127] B. W. Schulte,[9,10] B. F. Schutz,[17,9,10] E. Schwartz,[17] J. Scott,[24] S. M. Scott,[8] M. Seglar-Arroyo,[30] Y. Sekiguchi,[263] D. Sellers,[56] A. S. Sengupta,[259] D. Sentenac,[47] E. G. Seo,[130] V. Sequino,[25,4] A. Sergeev,[216] Y. Setyawati,[9,10,65] T. Shaffer,[72] M. S. Shahriar,[15] M. A. Shaikh,[19] B. Shams,[160] L. Shao,[200] A. Sharma,[32,107] P. Sharma,[94] P. Shawhan,[110] N. S. Shcheblanov,[228] A. Sheela,[241] Y. Shikano,[264,265] M. Shikauchi,[28] H. Shimizu,[266] K. Shimode,[191] H. Shinkai,[267] T. Shishido,[53] A. Shoda,[20] D. H. Shoemaker,[74]

D. M. Shoemaker,[171] S. ShyamSundar,[94] M. Sieniawska,[58] D. Sigg,[72] L. Silenzi,[40,41] L. P. Singer,[117] D. Singh,[149] M. K. Singh,[19] N. Singh,[109] A. Singha,[154,59] A. M. Sintes,[144] V. Sipala,[121,122] V. Skliris,[17] B. J. J. Slagmolen,[8] T. J. Slaven-Blair,[93] J. Smetana,[14] J. R. Smith,[44] L. Smith,[24] R. J. E. Smith,[5] J. Soldateschi,[229,268,55] S. N. Somala,[269] K. Somiya,[2] I. Song,[196] K. Soni,[11] S. Soni,[74] V. Sordini,[140] F. Sorrentino,[92] N. Sorrentino,[78,18] R. Soulard,[37] T. Souradeep,[270,11] E. Sowell,[147] V. Spagnuolo,[154,59] A. P. Spencer,[24] M. Spera,[80,81] P. Spinicelli,[47] A. K. Srivastava,[84] V. Srivastava,[67] K. Staats,[15] C. Stachie,[37] F. Stachurski,[24] D. A. Steer,[45] J. Steinlechner,[154,59] S. Steinlechner,[154,59] N. Stergioulas,[201] D. J. Stops,[14] M. Stover,[237] K. A. Strain,[24] L. C. Strang,[120] G. Stratta,[271,57] M. D. Strong,[7] A. Strunk,[72] R. Sturani,[252] A. L. Stuver,[113] M. Suchenek,[86] S. Sudhagar,[11] V. Sudhir,[74] R. Sugimoto,[272,243] H. G. Suh,[6] A. G. Sullivan,[50] T. Z. Summerscales,[273] L. Sun,[8] S. Sunil,[84] A. Sur,[86] J. Suresh,[28] P. J. Sutton,[17] Takamasa Suzuki,[177] Takanori Suzuki,[2] Toshikazu Suzuki,[189] B. L. Swinkels,[59] M. J. Szczepańczyk,[76] P. Szewczyk,[109] M. Tacca,[59] H. Tagoshi,[189] S. C. Tait,[24] H. Takahashi,[274] R. Takahashi,[20] S. Takano,[27] H. Takeda,[27] M. Takeda,[178] C. J. Talbot,[33] C. Talbot,[1] K. Tanaka,[275] Taiki Tanaka,[189] Takahiro Tanaka,[276] A. J. Tanasijczuk,[58] S. Tanioka,[191] D. B. Tanner,[76] D. Tao,[1] L. Tao,[76] R. D. Tapia,[149] E. N. Tapia San Martín,[59] C. Taranto,[123] A. Taruya,[277] J. D. Tasson,[161] R. Tenorio,[144] J. E. S. Terhune,[113] L. Terkowski,[127] M. P. Thirugnanasambandam,[11] M. Thomas,[56] P. Thomas,[72] E. E. Thompson,[48] J. E. Thompson,[17] S. R. Thondapu,[94] K. A. Thorne,[56] E. Thrane,[5] Shubhanshu Tiwari,[163] Srishti Tiwari,[11] V. Tiwari,[17] A. M. Toivonen,[148] A. E. Tolley,[51] T. Tomaru,[20] T. Tomura,[191] M. Tonelli,[78,18] Z. Tornasi,[24] A. Torres-Forné,[126] C. I. Torrie,[1] I. Tosta e Melo,[122] D. Töyrä,[8] A. Trapananti,[41,40] F. Travasso,[40,41] G. Traylor,[56] M. Trevor,[110] M. C. Tringali,[47] A. Tripathee,[185] L. Troiano,[278,103] A. Trovato,[45] L. Trozzo,[4,191] R. J. Trudeau,[1] D. Tsai,[129] K. W. Tsang,[59,279,65] T. Tsang,[280] J-S. Tsao,[233] M. Tse,[74] R. Tso,[136] S. Tsuchida,[178] L. Tsukada,[149] D. Tsuna,[28] T. Tsutsui,[28] K. Turbang,[281,206] M. Turconi,[37] D. Tuyenbayev,[178] A. S. Ubhi,[14] N. Uchikata,[189] T. Uchiyama,[191] R. P. Udall,[1] A. Ueda,[282] T. Uehara,[283,284] K. Ueno,[28] G. Ueshima,[285] C. S. Unnikrishnan,[286] A. L. Urban,[7] T. Ushiba,[191] A. Utina,[154,59] G. Vajente,[1] A. Vajpeyi,[5] G. Valdes,[186] M. Valentini,[184,98,99] V. Valsan,[6] N. van Bakel,[59] M. van Beuzekom,[59] M. van Dael,[59,287] J. F. J. van den Brand,[154,96,59] C. Van Den Broeck,[65,59] D. C. Vander-Hyde,[67] H. van Haevermaet,[206] J. V. van Heijningen,[58] M. H. P. M. van Putten,[288] N. van Remortel,[206] M. Vardaro,[213,59] A. F. Vargas,[120] V. Varma,[111] M. Vasúth,[75] A. Vecchio,[14] G. Vedovato,[81] J. Veitch,[24] P. J. Veitch,[88] J. Venneberg,[9,10] G. Venugopalan,[1] D. Verkindt,[30] P. Verma,[162] Y. Verma,[94] S. M. Vermeulen,[17] D. Veske,[50] F. Vetrano,[54] A. Viceré,[54,55] S. Vidyant,[67] A. D. Viets,[289] A. Vijaykumar,[19] V. Villa-Ortega,[114] J.-Y. Vinet,[37] A. Virtuoso,[239,35] S. Vitale,[74] H. Vocca,[79,40] E. R. G. von Reis,[72] J. S. A. von Wrangel,[9,10] C. Vorvick,[72] S. P. Vyatchanin,[97] L. E. Wade,[237] M. Wade,[237] K. J. Wagner,[128] R. C. Walet,[59] M. Walker,[63] G. S. Wallace,[33] L. Wallace,[1] J. Wang,[179] J. Z. Wang,[185] W. H. Wang,[89] R. L. Ward,[8] J. Warner,[72] M. Was,[30] T. Washimi,[20] N. Y. Washington,[1] J. Watchi,[145] B. Weaver,[72] C. R. Weaving,[51] S. A. Webster,[24] M. Weinert,[9,10] A. J. Weinstein,[1] R. Weiss,[74] C. M. Weller,[258] R. A. Weller,[205] F. Wellmann,[9,10] L. Wen,[93] P. Weßels,[9,10] K. Wette,[8] J. T. Whelan,[128] D. D. White,[44] B. F. Whiting,[76] C. Whittle,[74] D. Wilken,[9,10] D. Williams,[24] M. J. Williams,[24] A. R. Williamson,[51] J. L. Willis,[1] B. Willke,[9,10] D. J. Wilson,[255] C. C. Wipf,[1] T. Wlodarczyk,[111] G. Woan,[24] J. Woehler,[9,10] J. K. Wofford,[128] D. Wong,[182] I. C. F. Wong,[130] M. Wright,[24] C. Wu,[137] D. S. Wu,[9,10] H. Wu,[137] D. M. Wysocki,[6] L. Xiao,[1] T. Yamada,[266] H. Yamamoto,[1] K. Yamamoto,[190] T. Yamamoto,[191] K. Yamashita,[202] R. Yamazaki,[199] F. W. Yang,[160] K. Z. Yang,[148] L. Yang,[169] Y.-C. Yang,[129] Y. Yang,[290] Yang Yang,[76] M. J. Yap,[8] D. W. Yeeles,[17] S.-W. Yeh,[137] A. B. Yelikar,[128] M. Ying,[129] J. Yokoyama,[28,27] T. Yokozawa,[191] J. Yoo,[181] T. Yoshioka,[202] Hang Yu,[136] Haocun Yu,[74] H. Yuzurihara,[189] A. Zadrożny,[162] M. Zanolin,[36] S. Zeidler,[291] T. Zelenova,[47] J.-P. Zendri,[81] M. Zevin,[167] M. Zhan,[179] H. Zhang,[233] J. Zhang,[93] L. Zhang,[1] R. Zhang,[76] T. Zhang,[14] Y. Zhang,[186] C. Zhao,[93] G. Zhao,[145] Y. Zhao,[189,20] Yue Zhao,[160] R. Zhou,[192] Z. Zhou,[15] X. J. Zhu,[5] Z.-H. Zhu,[119,231] M. E. Zucker,[1,74] and J. Zweizig[1]

(LIGO Scientific Collaboration, Virgo Collaboration, and KAGRA Collaboration)

[1]*LIGO Laboratory, California Institute of Technology, Pasadena, California 91125, USA*
[2]*Graduate School of Science, Tokyo Institute of Technology, Meguro-ku, Tokyo 152-8551, Japan*
[3]*Dipartimento di Farmacia, Università di Salerno, I-84084 Fisciano, Salerno, Italy*
[4]*INFN, Sezione di Napoli, Complesso Universitario di Monte S. Angelo, I-80126 Napoli, Italy*
[5]*OzGrav, School of Physics and Astronomy, Monash University, Clayton 3800, Victoria, Australia*
[6]*University of Wisconsin-Milwaukee, Milwaukee, Wisconsin 53201, USA*
[7]*Louisiana State University, Baton Rouge, Louisiana 70803, USA*
[8]*OzGrav, Australian National University, Canberra, Australian Capital Territory 0200, Australia*
[9]*Max Planck Institute for Gravitational Physics (Albert Einstein Institute), D-30167 Hannover, Germany*

[10]*Leibniz Universität Hannover, D-30167 Hannover, Germany*
[11]*Inter-University Centre for Astronomy and Astrophysics, Pune 411007, India*
[12]*University of Cambridge, Cambridge CB2 1TN, United Kingdom*
[13]*Theoretisch-Physikalisches Institut, Friedrich-Schiller-Universität Jena, D-07743 Jena, Germany*
[14]*University of Birmingham, Birmingham B15 2TT, United Kingdom*
[15]*Northwestern University, Evanston, Illinois 60208, USA*
[16]*Instituto Nacional de Pesquisas Espaciais, 12227-010 São José dos Campos, São Paulo, Brazil*
[17]*Cardiff University, Cardiff CF24 3AA, United Kingdom*
[18]*INFN, Sezione di Pisa, I-56127 Pisa, Italy*
[19]*International Centre for Theoretical Sciences, Tata Institute of Fundamental Research, Bengaluru 560089, India*
[20]*Gravitational Wave Science Project, National Astronomical Observatory of Japan (NAOJ), Mitaka City, Tokyo 181-8588, Japan*
[21]*Advanced Technology Center, National Astronomical Observatory of Japan (NAOJ), Mitaka City, Tokyo 181-8588, Japan*
[22]*Dipartimento di Fisica, Università degli Studi di Torino, I-10125 Torino, Italy*
[23]*INFN Sezione di Torino, I-10125 Torino, Italy*
[24]*SUPA, University of Glasgow, Glasgow G12 8QQ, United Kingdom*
[25]*Università di Napoli "Federico II," Complesso Universitario di Monte S. Angelo, I-80126 Napoli, Italy*
[26]*Université de Lyon, Université Claude Bernard Lyon 1, CNRS, Institut Lumière Matière, F-69622 Villeurbanne, France*
[27]*Department of Physics, The University of Tokyo, Bunkyo-ku, Tokyo 113-0033, Japan*
[28]*Research Center for the Early Universe (RESCEU), The University of Tokyo, Bunkyo-ku, Tokyo 113-0033, Japan*
[29]*Institut de Ciències del Cosmos (ICCUB), Universitat de Barcelona, C/ Martí i Franquès 1, Barcelona 08028, Spain*
[30]*Université Savoie Mont Blanc, CNRS, Laboratoire d'Annecy de Physique des Particules—IN2P3, F-74000 Annecy, France*
[31]*Institut de Física d'Altes Energies (IFAE), Barcelona Institute of Science and Technology, and ICREA, E-08193 Barcelona, Spain*
[32]*Gran Sasso Science Institute (GSSI), I-67100 L'Aquila, Italy*
[33]*SUPA, University of Strathclyde, Glasgow G1 1XQ, United Kingdom*
[34]*Dipartimento di Scienze Matematiche, Informatiche e Fisiche, Università di Udine, I-33100 Udine, Italy*
[35]*INFN, Sezione di Trieste, I-34127 Trieste, Italy*
[36]*Embry-Riddle Aeronautical University, Prescott, Arizona 86301, USA*
[37]*Artemis, Université Côte d'Azur, Observatoire de la Côte d'Azur, CNRS, F-06304 Nice, France*
[38]*GRAPPA, Anton Pannekoek Institute for Astronomy and Institute for High-Energy Physics, University of Amsterdam, Science Park 904, 1098 XH Amsterdam, Netherlands*
[39]*National and Kapodistrian University of Athens, School of Science Building, 2nd floor, Panepistimiopolis, 15771 Ilissia, Greece*
[40]*INFN, Sezione di Perugia, I-06123 Perugia, Italy*
[41]*Università di Camerino, Dipartimento di Fisica, I-62032 Camerino, Italy*
[42]*American University, Washington 20016, USA*
[43]*Earthquake Research Institute, The University of Tokyo, Bunkyo-ku, Tokyo 113-0032, Japan*
[44]*California State University Fullerton, Fullerton, California 92831, USA*
[45]*Université de Paris, CNRS, Astroparticule et Cosmologie, F-75006 Paris, France*
[46]*Université Paris-Saclay, CNRS/IN2P3, IJCLab, 91405 Orsay, France*
[47]*European Gravitational Observatory (EGO), I-56021 Cascina, Pisa, Italy*
[48]*Georgia Institute of Technology, Atlanta, Georgia 30332, USA*
[49]*Department of Mathematics and Physics, Graduate School of Science and Technology, Hirosaki University, Hirosaki, Aomori 036-8561, Japan*
[50]*Columbia University, New York, New York 10027, USA*
[51]*University of Portsmouth, Portsmouth PO1 3FX, United Kingdom*
[52]*Kamioka Branch, National Astronomical Observatory of Japan (NAOJ), Kamioka-cho, Hida City, Gifu 506-1205, Japan*
[53]*The Graduate University for Advanced Studies (SOKENDAI), Mitaka City, Tokyo 181-8588, Japan*
[54]*Università degli Studi di Urbino "Carlo Bo," I-61029 Urbino, Italy*
[55]*INFN, Sezione di Firenze, I-50019 Sesto Fiorentino, Firenze, Italy*
[56]*LIGO Livingston Observatory, Livingston, Louisiana 70754, USA*
[57]*INFN, Sezione di Roma, I-00185 Roma, Italy*

[58]*Université catholique de Louvain, B-1348 Louvain-la-Neuve, Belgium*
[59]*Nikhef, Science Park 105, 1098 XG Amsterdam, Netherlands*
[60]*King's College London, University of London, London WC2R 2LS, United Kingdom*
[61]*Korea Institute of Science and Technology Information, Daejeon 34141, Republic of Korea*
[62]*National Institute for Mathematical Sciences, Daejeon 34047, Republic of Korea*
[63]*Christopher Newport University, Newport News, Virginia 23606, USA*
[64]*School of High Energy Accelerator Science,*
The Graduate University for Advanced Studies (SOKENDAI), Tsukuba City, Ibaraki 305-0801, Japan
[65]*Institute for Gravitational and Subatomic Physics (GRASP), Utrecht University,*
Princetonplein 1, 3584 CC Utrecht, Netherlands
[66]*University of Oregon, Eugene, Oregon 97403, USA*
[67]*Syracuse University, Syracuse, New York 13244, USA*
[68]*Université de Liège, B-4000 Liège, Belgium*
[69]*Università degli Studi di Milano-Bicocca, I-20126 Milano, Italy*
[70]*INFN, Sezione di Milano-Bicocca, I-20126 Milano, Italy*
[71]*INAF, Osservatorio Astronomico di Brera sede di Merate, I-23807 Merate, Lecco, Italy*
[72]*LIGO Hanford Observatory, Richland, Washington 99352, USA*
[73]*Dipartimento di Medicina, Chirurgia e Odontoiatria "Scuola Medica Salernitana,"*
Università di Salerno, I-84081 Baronissi, Salerno, Italy
[74]*LIGO Laboratory, Massachusetts Institute of Technology, Cambridge, Massachusetts 02139, USA*
[75]*Wigner RCP, RMKI, H-1121 Budapest, Konkoly Thege Miklós út 29-33, Hungary*
[76]*University of Florida, Gainesville, Florida 32611, USA*
[77]*Stanford University, Stanford, California 94305, USA*
[78]*Università di Pisa, I-56127 Pisa, Italy*
[79]*Università di Perugia, I-06123 Perugia, Italy*
[80]*Università di Padova, Dipartimento di Fisica e Astronomia, I-35131 Padova, Italy*
[81]*INFN, Sezione di Padova, I-35131 Padova, Italy*
[82]*Bard College, Annandale-On-Hudson, New York 12504, USA*
[83]*Montana State University, Bozeman, Montana 59717, USA*
[84]*Institute for Plasma Research, Bhat, Gandhinagar 382428, India*
[85]*Universiteit Gent, B-9000 Gent, Belgium*
[86]*Nicolaus Copernicus Astronomical Center, Polish Academy of Sciences, 00-716 Warsaw, Poland*
[87]*Dipartimento di Ingegneria, Università del Sannio, I-82100 Benevento, Italy*
[88]*OzGrav, University of Adelaide, Adelaide, South Australia 5005, Australia*
[89]*The University of Texas Rio Grande Valley, Brownsville, Texas 78520, USA*
[90]*California State University, Los Angeles, Los Angeles, California 90032, USA*
[91]*Departamento de Matemáticas, Universitat Autònoma de Barcelona, Edificio C Facultad de Ciencias,*
08193 Bellaterra (Barcelona), Spain
[92]*INFN, Sezione di Genova, I-16146 Genova, Italy*
[93]*OzGrav, University of Western Australia, Crawley, Western Australia 6009, Australia*
[94]*RRCAT, Indore, Madhya Pradesh 452013, India*
[95]*Missouri University of Science and Technology, Rolla, Missouri 65409, USA*
[96]*Vrije Universiteit Amsterdam, 1081 HV Amsterdam, Netherlands*
[97]*Lomonosov Moscow State University, Moscow 119991, Russia*
[98]*Università di Trento, Dipartimento di Fisica, I-38123 Povo, Trento, Italy*
[99]*INFN, Trento Institute for Fundamental Physics and Applications, I-38123 Povo, Trento, Italy*
[100]*SUPA, University of the West of Scotland, Paisley PA1 2BE, United Kingdom*
[101]*Bar-Ilan University, Ramat Gan 5290002, Israel*
[102]*Dipartimento di Fisica "E.R. Caianiello," Università di Salerno, I-84084 Fisciano, Salerno, Italy*
[103]*INFN, Sezione di Napoli, Gruppo Collegato di Salerno, Complesso Universitario di Monte S. Angelo,*
I-80126 Napoli, Italy
[104]*Università di Roma "La Sapienza," I-00185 Roma, Italy*
[105]*Université Rennes, CNRS, Institut FOTON—UMR6082, F-3500 Rennes, France*
[106]*Indian Institute of Technology Bombay, Powai, Mumbai 400 076, India*
[107]*INFN, Laboratori Nazionali del Gran Sasso, I-67100 Assergi, Italy*
[108]*Laboratoire Kastler Brossel, Sorbonne Université, CNRS, ENS-Université PSL, Collège de France,*
F-75005 Paris, France
[109]*Astronomical Observatory Warsaw University, 00-478 Warsaw, Poland*
[110]*University of Maryland, College Park, Maryland 20742, USA*
[111]*Max Planck Institute for Gravitational Physics (Albert Einstein Institute), D-14476 Potsdam, Germany*

[112]*L2IT, Laboratoire des 2 Infinis—Toulouse, Université de Toulouse, CNRS/IN2P3, UPS, F-31062 Toulouse Cedex 9, France*
[113]*Villanova University, Villanova, Pennsylvania 19085, USA*
[114]*IGFAE, Universidade de Santiago de Compostela, Santiago de Compostela 15782, Spain*
[115]*Stony Brook University, Stony Brook, New York 11794, USA*
[116]*Center for Computational Astrophysics, Flatiron Institute, New York, New York 10010, USA*
[117]*NASA Goddard Space Flight Center, Greenbelt, Maryland 20771, USA*
[118]*Dipartimento di Fisica, Università degli Studi di Genova, I-16146 Genova, Italy*
[119]*Department of Astronomy, Beijing Normal University, Beijing 100875, China*
[120]*OzGrav, University of Melbourne, Parkville, Victoria 3010, Australia*
[121]*Università degli Studi di Sassari, I-07100 Sassari, Italy*
[122]*INFN, Laboratori Nazionali del Sud, I-95125 Catania, Italy*
[123]*Università di Roma Tor Vergata, I-00133 Roma, Italy*
[124]*INFN, Sezione di Roma Tor Vergata, I-00133 Roma, Italy*
[125]*University of Sannio at Benevento, I-82100 Benevento, Italy and INFN, Sezione di Napoli, I-80100 Napoli, Italy*
[126]*Departamento de Astronomía y Astrofísica, Universitat de València, E-46100 Burjassot, València, Spain*
[127]*Universität Hamburg, D-22761 Hamburg, Germany*
[128]*Rochester Institute of Technology, Rochester, New York 14623, USA*
[129]*National Tsing Hua University, Hsinchu City, 30013 Taiwan, Republic of China*
[130]*The Chinese University of Hong Kong, Shatin, NT, Hong Kong*
[131]*Department of Applied Physics, Fukuoka University, Jonan, Fukuoka City, Fukuoka 814-0180, Japan*
[132]*OzGrav, Charles Sturt University, Wagga Wagga, New South Wales 2678, Australia*
[133]*Department of Physics, Tamkang University, Danshui District, New Taipei City 25137, Taiwan*
[134]*Department of Physics and Institute of Astronomy, National Tsing Hua University, Hsinchu 30013, Taiwan*
[135]*Department of Physics, Center for High Energy and High Field Physics, National Central University, Zhongli District, Taoyuan City 32001, Taiwan*
[136]*CaRT, California Institute of Technology, Pasadena, California 91125, USA*
[137]*Department of Physics, National Tsing Hua University, Hsinchu 30013, Taiwan*
[138]*Dipartimento di Ingegneria Industriale (DIIN), Università di Salerno, I-84084 Fisciano, Salerno, Italy*
[139]*Institute of Physics, Academia Sinica, Nankang, Taipei 11529, Taiwan*
[140]*Université Lyon, Université Claude Bernard Lyon 1, CNRS, IP2I Lyon / IN2P3, UMR 5822, F-69622 Villeurbanne, France*
[141]*INAF, Osservatorio Astronomico di Padova, I-35122 Padova, Italy*
[142]*OzGrav, Swinburne University of Technology, Hawthorn VIC 3122, Australia*
[143]*Université libre de Bruxelles, Avenue Franklin Roosevelt, 50–1050 Bruxelles, Belgium*
[144]*IAC3–IEEC, Universitat de les Illes Balears, E-07122 Palma de Mallorca, Spain*
[145]*Université Libre de Bruxelles, Brussels 1050, Belgium*
[146]*Departamento de Matemáticas, Universitat de València, E-46100 Burjassot, València, Spain*
[147]*Texas Tech University, Lubbock, Texas 79409, USA*
[148]*University of Minnesota, Minneapolis, Minnesota 55455, USA*
[149]*The Pennsylvania State University, University Park, Pennsylvania 16802, USA*
[150]*University of Rhode Island, Kingston, Rhode Island 02881, USA*
[151]*Bellevue College, Bellevue, Washington 98007, USA*
[152]*Scuola Normale Superiore, Piazza dei Cavalieri, 7–56126 Pisa, Italy*
[153]*Eötvös University, Budapest 1117, Hungary*
[154]*Maastricht University, P.O. Box 616, 6200 MD Maastricht, Netherlands*
[155]*Chennai Mathematical Institute, Chennai 603103, India*
[156]*The University of Sheffield, Sheffield S10 2TN, United Kingdom*
[157]*Université Lyon, Université Claude Bernard Lyon 1, CNRS, Laboratoire des Matériaux Avancés (LMA), IP2I Lyon / IN2P3, UMR 5822, F-69622 Villeurbanne, France*
[158]*Dipartimento di Scienze Matematiche, Fisiche e Informatiche, Università di Parma, I-43124 Parma, Italy*
[159]*INFN, Sezione di Milano Bicocca, Gruppo Collegato di Parma, I-43124 Parma, Italy*
[160]*The University of Utah, Salt Lake City, Utah 84112, USA*
[161]*Carleton College, Northfield, Minnesota 55057, USA*
[162]*National Center for Nuclear Research, 05-400 Świerk-Otwock, Poland*
[163]*University of Zurich, Winterthurerstrasse 190, 8057 Zurich, Switzerland*

[164]Perimeter Institute, Waterloo, Ontario N2L 2Y5, Canada
[165]Université de Strasbourg, CNRS, IPHC UMR 7178, F-67000 Strasbourg, France
[166]West Virginia University, Morgantown, West Virginia 26506, USA
[167]University of Chicago, Chicago, Illinois 60637, USA
[168]Montclair State University, Montclair, New Jersey 07043, USA
[169]Colorado State University, Fort Collins, Colorado 80523, USA
[170]Institute for Nuclear Research, Bem t'er 18/c, H-4026 Debrecen, Hungary
[171]University of Texas, Austin, Texas 78712, USA
[172]CNR-SPIN, c/o Università di Salerno, I-84084 Fisciano, Salerno, Italy
[173]Scuola di Ingegneria, Università della Basilicata, I-85100 Potenza, Italy
[174]Observatori Astronòmic, Universitat de València, E-46980 Paterna, València, Spain
[175]Centro de Física das Universidades do Minho e do Porto, Universidade do Minho, Campus de Gualtar, PT-4710–057 Braga, Portugal
[176]Department of Astronomy, The University of Tokyo, Mitaka City, Tokyo 181-8588, Japan
[177]Faculty of Engineering, Niigata University, Nishi-ku, Niigata City, Niigata 950-2181, Japan
[178]Department of Physics, Graduate School of Science, Osaka City University, Sumiyoshi-ku, Osaka City, Osaka 558-8585, Japan
[179]State Key Laboratory of Magnetic Resonance and Atomic and Molecular Physics, Innovation Academy for Precision Measurement Science and Technology (APM), Chinese Academy of Sciences, Xiao Hong Shan, Wuhan 430071, China
[180]University of Szeged, Dóm tér 9, Szeged 6720, Hungary
[181]Cornell University, Ithaca, New York 14850, USA
[182]University of British Columbia, Vancouver, British Columbia V6T 1Z4, Canada
[183]INAF, Osservatorio Astronomico di Capodimonte, I-80131 Napoli, Italy
[184]The University of Mississippi, University, Mississippi 38677, USA
[185]University of Michigan, Ann Arbor, Michigan 48109, USA
[186]Texas A&M University, College Station, Texas 77843, USA
[187]Ulsan National Institute of Science and Technology, Ulsan 44919, Republic of Korea
[188]Shanghai Astronomical Observatory, Chinese Academy of Sciences, Shanghai 200030, China
[189]Institute for Cosmic Ray Research (ICRR), KAGRA Observatory, The University of Tokyo, Kashiwa City, Chiba 277-8582, Japan
[190]Faculty of Science, University of Toyama, Toyama City, Toyama 930-8555, Japan
[191]Institute for Cosmic Ray Research (ICRR), KAGRA Observatory, The University of Tokyo, Kamioka-cho, Hida City, Gifu 506-1205, Japan
[192]University of California, Berkeley, California 94720, USA
[193]Maastricht University, 6200 MD Maastricht, Netherlands
[194]Lancaster University, Lancaster LA1 4YW, United Kingdom
[195]College of Industrial Technology, Nihon University, Narashino City, Chiba 275-8575, Japan
[196]Institute of Astronomy, National Tsing Hua University, Hsinchu 30013, Taiwan
[197]Rutherford Appleton Laboratory, Didcot OX11 0DE, United Kingdom
[198]Department of Astronomy and Space Science, Chungnam National University, Yuseong-gu, Daejeon 34134, Republic of Korea
[199]Department of Physical Sciences, Aoyama Gakuin University, Sagamihara City, Kanagawa 252-5258, Japan
[200]Kavli Institute for Astronomy and Astrophysics, Peking University, Haidian District, Beijing 100871, China
[201]Aristotle University of Thessaloniki, University Campus, 54124 Thessaloniki, Greece
[202]Graduate School of Science and Engineering, University of Toyama, Toyama City, Toyama 930-8555, Japan
[203]Nambu Yoichiro Institute of Theoretical and Experimental Physics (NITEP), Osaka City University, Sumiyoshi-ku, Osaka City, Osaka 558-8585, Japan
[204]Directorate of Construction, Services and Estate Management, Mumbai 400094, India
[205]Vanderbilt University, Nashville, Tennessee 37235, USA
[206]Universiteit Antwerpen, Prinsstraat 13, 2000 Antwerpen, Belgium
[207]University of Białystok, 15-424 Białystok, Poland
[208]Ewha Womans University, Seoul 03760, Republic of Korea
[209]National Astronomical Observatories, Chinese Academic of Sciences, 20A Datun Road, Chaoyang District, Beijing, China
[210]School of Astronomy and Space Science, University of Chinese Academy of Sciences, 20A Datun Road, Chaoyang District, Beijing, China

[211]*University of Southampton, Southampton SO17 1BJ, United Kingdom*
[212]*Institute for Cosmic Ray Research (ICRR), The University of Tokyo, Kashiwa City, Chiba 277-8582, Japan*
[213]*Institute for High-Energy Physics, University of Amsterdam, Science Park 904, 1098 XH Amsterdam, Netherlands*
[214]*Chung-Ang University, Seoul 06974, Republic of Korea*
[215]*University of Washington Bothell, Bothell, Washington 98011, USA*
[216]*Institute of Applied Physics, Nizhny Novgorod 603950, Russia*
[217]*Inje University Gimhae, South Gyeongsang 50834, Republic of Korea*
[218]*Department of Physics, Myongji University, Yongin 17058, Republic of Korea*
[219]*Institute of Particle and Nuclear Studies (IPNS), High Energy Accelerator Research Organization (KEK), Tsukuba City, Ibaraki 305-0801, Japan*
[220]*School of Physics and Astronomy, Cardiff University, Cardiff CF24 3AA, United Kingdom*
[221]*Institute of Mathematics, Polish Academy of Sciences, 00656 Warsaw, Poland*
[222]*Instituto de Fisica Teorica, 28049 Madrid, Spain*
[223]*Department of Physics, Nagoya University, Chikusa-ku, Nagoya, Aichi 464-8602, Japan*
[224]*Université de Montréal/Polytechnique, Montreal, Quebec H3T 1J4, Canada*
[225]*Laboratoire Lagrange, Université Côte d'Azur, Observatoire Côte d'Azur, CNRS, F-06304 Nice, France*
[226]*Seoul National University, Seoul 08826, Republic of Korea*
[227]*Sungkyunkwan University, Seoul 03063, Republic of Korea*
[228]*NAVIER, École des Ponts, Univ Gustave Eiffel, CNRS, 77454 Marne-la-Vallée, France*
[229]*Università di Firenze, Sesto Fiorentino I-50019, Italy*
[230]*Department of Physics, National Cheng Kung University, Tainan City 701, Taiwan*
[231]*School of Physics and Technology, Wuhan University, Wuhan, Hubei 430072, China*
[232]*National Center for High-performance computing, National Applied Research Laboratories, Hsinchu Science Park, Hsinchu City 30076, Taiwan*
[233]*Department of Physics, National Taiwan Normal University, sec. 4, Taipei 116, Taiwan*
[234]*NASA Marshall Space Flight Center, Huntsville, Alabama 35811, USA*
[235]*INFN, Sezione di Roma Tre, I-00146 Roma, Italy*
[236]*ESPCI, CNRS, F-75005 Paris, France*
[237]*Kenyon College, Gambier, Ohio 43022, USA*
[238]*School of Physics Science and Engineering, Tongji University, Shanghai 200092, China*
[239]*Dipartimento di Fisica, Università di Trieste, I-34127 Trieste, Italy*
[240]*Institute for Photon Science and Technology, The University of Tokyo, Bunkyo-ku, Tokyo 113-8656, Japan*
[241]*Indian Institute of Technology Madras, Chennai 600036, India*
[242]*Saha Institute of Nuclear Physics, Bidhannagar, West Bengal 700064, India*
[243]*Institute of Space and Astronautical Science (JAXA), Chuo-ku, Sagamihara City, Kanagawa 252-0222, Japan*
[244]*Institut des Hautes Etudes Scientifiques, F-91440 Bures-sur-Yvette, France*
[245]*Faculty of Law, Ryukoku University, Fushimi-ku, Kyoto City, Kyoto 612-8577, Japan*
[246]*Indian Institute of Science Education and Research, Kolkata, Mohanpur, West Bengal 741252, India*
[247]*Department of Physics, University of Notre Dame, Notre Dame, Indiana 46556, USA*
[248]*Graduate School of Science and Technology, Niigata University, Nishi-ku, Niigata City, Niigata 950-2181, Japan*
[249]*Consiglio Nazionale delle Ricerche—Istituto dei Sistemi Complessi, Piazzale Aldo Moro 5, I-00185 Roma, Italy*
[250]*Korea Astronomy and Space Science Institute (KASI), Yuseong-gu, Daejeon 34055, Republic of Korea*
[251]*Hobart and William Smith Colleges, Geneva, New York 14456, USA*
[252]*International Institute of Physics, Universidade Federal do Rio Grande do Norte, Natal RN 59078-970, Brazil*
[253]*Museo Storico della Fisica e Centro Studi e Ricerche "Enrico Fermi," I-00184 Roma, Italy*
[254]*Dipartimento di Matematica e Fisica, Università degli Studi Roma Tre, I-00146 Roma, Italy*
[255]*University of Arizona, Tucson, Arizona 85721, USA*
[256]*Università di Trento, Dipartimento di Matematica, I-38123 Povo, Trento, Italy*
[257]*University of California, Riverside, Riverside, California 92521, USA*
[258]*University of Washington, Seattle, Washington 98195, USA*
[259]*Indian Institute of Technology, Palaj, Gandhinagar, Gujarat 382355, India*

[260]Department of Electronic Control Engineering, National Institute of Technology, Nagaoka College, Nagaoka City, Niigata 940-8532, Japan
[261]Departamento de Matemática da Universidade de Aveiro and Centre for Research and Development in Mathematics and Applications, Campus de Santiago, 3810-183 Aveiro, Portugal
[262]Marquette University, Milwaukee, Wisconsin 53233, USA
[263]Faculty of Science, Toho University, Funabashi City, Chiba 274-8510, Japan
[264]Graduate School of Science and Technology, Gunma University, Maebashi, Gunma 371-8510, Japan
[265]Institute for Quantum Studies, Chapman University, Orange, California 92866, USA
[266]Accelerator Laboratory, High Energy Accelerator Research Organization (KEK), Tsukuba City, Ibaraki 305-0801, Japan
[267]Faculty of Information Science and Technology, Osaka Institute of Technology, Hirakata City, Osaka 573-0196, Japan
[268]INAF, Osservatorio Astrofisico di Arcetri, Largo E. Fermi 5, I-50125 Firenze, Italy
[269]Indian Institute of Technology Hyderabad, Sangareddy, Khandi, Telangana 502285, India
[270]Indian Institute of Science Education and Research, Pune, Maharashtra 411008, India
[271]Istituto di Astrofisica e Planetologia Spaziali di Roma, Via del Fosso del Cavaliere, 100, 00133 Roma RM, Italy
[272]Department of Space and Astronautical Science, The Graduate University for Advanced Studies (SOKENDAI), Sagamihara City, Kanagawa 252-5210, Japan
[273]Andrews University, Berrien Springs, Michigan 49104, USA
[274]Research Center for Space Science, Advanced Research Laboratories, Tokyo City University, Setagaya, Tokyo 158-0082, Japan
[275]Institute for Cosmic Ray Research (ICRR), Research Center for Cosmic Neutrinos (RCCN), The University of Tokyo, Kashiwa City, Chiba 277-8582, Japan
[276]Department of Physics, Kyoto University, Sakyou-ku, Kyoto City, Kyoto 606-8502, Japan
[277]Yukawa Institute for Theoretical Physics (YITP), Kyoto University, Sakyou-ku, Kyoto City, Kyoto 606-8502, Japan
[278]Dipartimento di Scienze Aziendali—Management and Innovation Systems (DISA-MIS), Università di Salerno, I-84084 Fisciano, Salerno, Italy
[279]Van Swinderen Institute for Particle Physics and Gravity, University of Groningen, Nijenborgh 4, 9747 AG Groningen, Netherlands
[280]Faculty of Science, Department of Physics, The Chinese University of Hong Kong, Shatin, N.T., Hong Kong
[281]Vrije Universiteit Brussel, Pleinlaan 2, 1050 Brussel, Belgium
[282]Applied Research Laboratory, High Energy Accelerator Research Organization (KEK), Tsukuba City, Ibaraki 305-0801, Japan
[283]Department of Communications Engineering, National Defense Academy of Japan, Yokosuka City, Kanagawa 239-8686, Japan
[284]Department of Physics, University of Florida, Gainesville, Florida 32611, USA
[285]Department of Information and Management Systems Engineering, Nagaoka University of Technology, Nagaoka City, Niigata 940-2188, Japan
[286]Tata Institute of Fundamental Research, Mumbai 400005, India
[287]Eindhoven University of Technology, Postbus 513, 5600 MB Eindhoven, Netherlands
[288]Department of Physics and Astronomy, Sejong University, Gwangjin-gu, Seoul 143-747, Republic of Korea
[289]Concordia University Wisconsin, Mequon, Wisconsin 53097, USA
[290]Department of Electrophysics, National Yang Ming Chiao Tung University, 300 Hsinchu, Taiwan
[291]Department of Physics, Rikkyo University, Toshima-ku, Tokyo 171-8501, Japan

[†]Deceased, August 2020.
[‡]Deceased, April 2021.